

ABSTRACT

Title of Document: IMPACT OF DUST ON THE RELIABILITY
OF PRINTED CIRCUIT ASSEMBLIES

Bo Song, Doctor of Philosophy, 2012

Dissertation directed By: Professor Michael G. Pecht
Department of Mechanical Engineering

Dust is a ubiquitous component of the environments in which we live and work. It can deposit on printed circuit assembly to act as a source of ionic contamination. Two common consequences of dust contaminations in the printed circuit boards are loss of impedance (i.e., loss of surface insulation resistance) and electrochemical migration between traces and component leads. Both failure mechanisms involve the contamination forming a current leakage path on a printed circuit board. Based on studies on ionic contaminations, researchers have argued that the impact of dust in these two failure mechanisms is dependent on its pH, its hygroscopic compositions, and the critical relative humidity of the salts in it. However, due to the lack of experimental results and the complexity of dust compositions, the argument is not substantiated. Very few papers concerning the impact of different natural dusts on these two failure mechanisms can be found in the literature. In practice, mixtures of Arizona dust and salts are used as a substitute for dust in experiments. In this research, natural dusts were collected from four locations: natural outdoor and indoor dust samples from Massachusetts, U.S., natural

outdoor dust from Tianjin, China, and the ISO standard test dust (Arizona test dust). Loss of impedance in dust contaminated printed circuit boards was investigated under controlled temperature (20°C to 60°C) and relative humidity (50% to 95%) ranges. The impact of dust on electrochemical migration and corrosion was evaluated under temperature-humidity-bias tests (50°C, 90% RH, and 10 VDC). In addition to the conventional DC measurement where only resistive data can be obtained, electrochemical impedance spectroscopy were adopted to obtain nonlinear equivalent circuit models of the electrochemical process, which helps to understand the underlying physics-of-failure.

The variation of impedance with relative humidity exhibited a transition range. Below the range, the impedance was constant, and above it, the impedance degraded by orders of magnitude. The value of the transition range decreased with an increase of dust deposition density. The equivalent circuit modeling showed that the dominant resistive path gradually shifted from the bulk to the interfacial with the increase of temperature from 20 °C to 60 °C. There were big variations among different dusts, which were quantified using the degradation factor introduced in the research, the critical transition range, and time-to-failure. This result demonstrated that a single salt or a mixture of compounds can not be representative of all dusts. It also indicated that using the ISO standard test dust in place of natural dust samples for reliability evaluation could lead to inaccurate results. Dust should be collected from the field in order to evaluate its impact. It is showed in this thesis that some critical characteristics of dust can be used to classify different dusts for the failure mechanisms of interest. Moisture sorption capability of dust can be used to classify different dusts regarding the loss of impedance failure. The dust with the highest moisture sorption capability had the highest degradation factor. Ion

species/concentration or conductivity of dust aqueous solution can be used to classify dust regarding the electrochemical migration related failures. Dust with the highest ion concentration and conductivity had the lowest time-to-failure. The underlying principals behind those critical characteristics were described and discussed based on the physics-of-failure.

IMPACT OF DUST ON THE RELIABILITY OF PRINTED CIRCUIT ASSEMBLIES

By

Bo Song

Dissertation submitted to the Faculty of the Graduate School of the
University of Maryland, College Park in partial fulfillment
of the requirements for the degree of
Doctor of Philosophy
2012

Advisory Committee:

Professor Michael G. Pecht, Chair
Dr. Michael H. Azarian
Professor Wang, Chunsheng
Professor Aris Christou
Professor Abhijit Dasgupta
Professor Peter Sandborn

© Copyright by

Bo Song

2012

Acknowledgement

My greatest gratitude is to my advisor, Prof. Michael Pecht. I feel so fortunate to have him as my advisor, who always gives me the freedom to explore and encourages me to think deeper. Dr. Pecht also taught me how to think and question, when I felt my research was going nowhere. Dr. Pecht advised me “Patience is a virtue”, when I was frustrated. His advice and encouragement guided me to complete my research and finish this dissertation.

I would also present the sincerest thanks to Dr. Michael Azarian for his invaluable discussion with me on this research topic and for his continuous encouragement for my study. Dr. Azarian has been always there to listen and give good advice. I am deeply grateful to him for the discussions that helped me sort out the technical details of my research work.

I am very grateful to Dr. Chunsheng Wang for the long discussions that brought me into a research area which was new to me. I would like to thank Dr. Aris Christou, Dr. Abhigjit Dasgupta, Dr. Peter Sandborn, and Dr. Chunsheng Wang for kindly consenting to be on my dissertation committee and evaluating my work.

My friends in CALCE research center, Vicor Corporation and Dräger Medical Inc. have helped and supported me through my Ph.D. years. Their friendship helped me overcome numerous difficulties and stay focused on my study. I greatly value their friendship and I

deeply appreciate their faith in me. I would like to give my special thanks to Yuhan Huang, Dr. Jun Dai, Fei Chai, and Xiaofei He in CALCE, Dr. Lidia Lee, Guang Xu, Wenlong Wang and Hardie Macauley in Vicor, Ken Zhen, Don Naugler, Christina DeMur in Dräger.

I am especially indebted to my parents for their everlasting support and patience. I would like to give my very special thanks to my husband, Dr. Zhi Han, for his unconditional love and the greatest support. Without their love and patience none of this would have been possible.

Table of Contents

Acknowledgement	II
Table of Contents	IV
List of Tables	VII
List of Figures.....	IX
List of Figures.....	IX
Chapter 1: Introduction	1
Chapter 2: Background on Dust.....	8
Natural Dust Properties	8
Dust particle sizes and sources.....	8
Compositions and key ions	10
Indoor and outdoor dust contamination levels	19
Dust Samples Used in Accelerated Tests	20
Chapter 3: Dust related Failure Mechanisms, Test Methods and Models	24
Surface Insulation Resistance Degradation.....	25
Electrochemical Migration	28
Electrochemical Corrosion	30
Available Test methods	36
Time-to-Failure Models	42
Arrhenius-based empirical models for ECM.....	42
Physics-of-failure models for ECM	44
Empirical linear bi-logarithmic law for atmospheric corrosion	45
Chapter 4: Impedance Spectroscopy	47
Models of Electrochemical Reactions	48

Kinetic Models	51
Mass transfer controlled models.....	52
Equivalent Circuit Modeling	56
Electrical double layer capacitance	56
Warburg impedance	58
Randles Circuit Model	59
Chapter 5: Methodology.....	62
Different Natural Dusts and Standard Test Dust	62
Design of Test Coupon	63
Estimation of Dust Deposition Density	66
Dust Deposition.....	67
Experimental Approach.....	69
Test Measurement	72
Chapter 6: Experimental Results	75
Characterization of Different Dusts.....	75
Ion Chromatography Analysis.....	75
SEM-EDS Analysis.....	76
pH and Conductivity	77
Moisture Sorption Study	80
Relative Humidity Effect.....	82
Temperature Effect	86
Comparison of Different Dusts.....	87
Varying Relative Humidity Tests.....	87
Varying Temperature Tests	90
Impact of Dust during Temperature-Humidity-Bias Test	91
Chapter 7: Discussions	97
Relative Humidity Effect.....	97
Temperature Effect	101
Other Factors	106
Comparison of Different Dusts.....	107
Chapter 8: Field Data	115

Case Study 1: Solder Metal Migration with Ni/Pb/Au Lead Finish.....	116
Case Study 2: Solder Metal Migration with Ni/Pb Lead Finish.....	121
Case Study 3: Conductive Path Formation Caused by Dust	124
Summary	126
Chapter 9: Conclusions	127
Chapter 10: Recommended Future Work.....	129
Bibliography	133

List of Tables

Table 1: Relative contents of main mineral particles in dust.....	11
Table 2: Composition of test dust used in other research	21
Table 3: Composition of Standard Test Dust.....	22
Table 4: Composition of Arizona Test Dust.....	23
Table 5: Critical relative humidity (CRH) for several inorganic compounds	26
Table 6: Standard Electrode Potentials in an Aqueous Solution at 25°C	30
Table 7: Average Yearly Levels of Indoor/Outdoor Contaminants.....	66
Table 8: Deposition Velocities for Airborne Particles (cm/s)	67
Table 9: Surface Deposition Density of Dust per Year	67
Table 10: Summary of test s and sample size.	71
Table 11: Ion analysis results.....	76
Table 12: pH and conductivity measurements at 22°C.....	78
Table 13: Chemical compositions of Dust 4 (ISO test dust).	78
Table 14: Weight gain at 48 hrs.....	82
Table 15: Summary of the time-to-failures of different types of dust.	93
Table 16: CRH of possible inorganic compounds in dust samples at 25°C.....	99
Table 17: Summary of the results of mathematical fit to the equivalent circuit at different temperatures with 90% RH (Dust 1, 1X).....	105
Table 18: Summary of test results of different dust types	111
Table 19: The probability of occurrences of each element on 12 locations	120
Table 20: Results of compositional analysis of dust on the substrate.....	125

Table 21: Recommended evaluation approaches for each step 132

List of Figures

Figure 1: Typical size ranges for some types of aerosol particles	9
Figure 2: Schematic drawing of normalized frequency plots of the number and volume distribution as a function of the grand average 1969 Pasadena aerosol	10
Figure 3: Examples of dust particles.....	11
Figure 4: Schematic drawing of multi-layer structure of dust.....	12
Figure 5: A Schematic Representation of the ECM Phenomenon	28
Figure 6: Mechanism of atmospheric corrosion [59].....	34
Figure 7: Sketch of the Hygroscopic Salt Mist Deposition System [6].....	37
Figure 8: Schematic Representation of Dust Chamber used for Exposure of Test Connectors [11].....	38
Figure 9: Change of Temperature and Relative Humidity in Damp Heat Experiments [10]	40
Figure 10: Simplified Diagram of Dust Chamber [10].....	41
Figure 11 A typical polarization curve of fuel cell and decomposition of the potential losses [5]	50
Figure 12: Cylindrical coordinate system.....	53
Figure 13: Double layer structure (adapted from [16]).....	57
Figure 14: Randles circuit.....	60
Figure 15: Site of Dust 1	62
Figure 16: Site of Dust 2.....	63
Figure 17: Test coupon with 6 pairs of parallel electrodes used in preliminary tests.....	64
Figure 18: Comb structure test coupons	65

Figure 19: Schematics of comb structure test coupon	65
Figure 20: Test coupons with different dust deposition densities.....	68
Figure 21: Relative humidity step-up profile.....	69
Figure 22: Temperature step-up profile	70
Figure 23: Resistance monitoring in THB test	73
Figure 24: Moisture soak plot of different specimens.	81
Figure 25: Bode plot at different RHs at dust deposition density 2X at 40°C (Dust 1). (a) Bode magnitude plot, (b) Phase angle plot.	83
Figure 26: Impedance magnitude trend over the tested relative humidity range for control boards and Dust 1 deposited boards with a deposition density of 1X or 3X at 40°C.....	84
Figure 27: Dependence of critical transition range on dust deposition density based on average results of three samples at 40°C. (a) Dust 1, (b) Dust 2.	86
Figure 28: Temperature effects on impedance magnitude at 20 Hz at different dust deposition densities at 90% (Dust 1).	87
Figure 29: Comparison of impedance data of test boards deposited with different dusts under RH tests.....	89
Figure 30: Critical transition ranges of different dusts.	89
Figure 31: Comparison of impedance data of test boards deposited with different dusts under temperature test.....	91
Figure 32: The resistance monitoring plot of a control sample.	92
Figure 33: The resistance-monitoring plot of a test sample deposited with Dust 3.....	92
Figure 34: ECM on Dust 3 deposited test board.....	94

Figure 35: ECM on Dust 2 deposited test board showing metal migration over the fibers	94
Figure 36: Corrosion on Dust 1 deposited test board.	95
Figure 37: ECM on Dust 4 deposited test board.....	96
Figure 38: Mass change of a mixed salt particle with relative humidity.	99
Figure 39: Schematic drawing of dust particles deposited on the substrate at 1X and 4X.	100
Figure 40: Equivalent circuit used for impedance measurement on dust contaminated test boards.....	102
Figure 41: Bode plot at different temperatures at dust deposition density 1X at 90% RH (Dust 1). (a) Bode magnitude plot, (b) Phase angle plot.	103
Figure 42: Impedance magnitude and extracted bulk resistance at different temperatures with 90% RH (Dust 1, 1X).	105
Figure 43: Degradation factors of different dusts in the RH tests at 40°C.....	108
Figure 44: Degradation factors of different dusts in the temperature tests at 80% RH..	108
Figure 45: Conductivity of different dusts in the RH tests at 40°C. (a) based on R_{bulk} .(b) based on impedance magnitude($ Z $)......	109
Figure 46: XRF spectrum of the component lead.....	117
Figure 47: Optical image of the failed QSP component.....	117
Figure 48: X-Ray image of the failed leads	118
Figure 49: SEM image of shorted leads in example 1	118
Figure 50: EDS mapping of the area shown in Figure 49.....	119
Figure 51: SEM image of Sn-Pb dendrites mixed with dust particles.....	121

Figure 52: SEM image of dendrite growth between leads.....	122
Figure 53: Results of EDS mapping analysis on the substrate between leads.....	122
Figure 54: SEM image of front end of the migration path (close to the anode).....	122
Figure 55: Magnified SEM image with metal oxides/hydroxides and dust particles.....	123
Figure 56: SEM image of a dust formed path.....	124
Figure 57: Proposed test methodology for dust evaluation	130

Chapter 1: Introduction

The reliability of electronic product has been an active research area with the rapid growth of the electronics industry. The reliability of electronics is usually affected by the manufacture process and operating environments. Common concerns are related to contaminations, mechanical, thermal and chemical stresses and strains. Contaminations of electronic products originate from chemicals that are either left on the product during manufacture process, or materials accumulated after the manufacture. Contaminations from use environments can be divided into two main classes, gas and dust. This thesis concerns the reliability impact of dust contaminations

Dust is a ubiquitous component of the environments in which we live and work. It is one of the most common contaminations for electronic devices and equipment. The impact of dust on reliability has been reported and attracted researchers attention since the early 1990s, *e.g.* [6][8][11][12]. It has recently become a more active research area in reliability due to the new challenges in the operating environments. Most electronic devices used to stay in a well-controlled indoor environment, where 95% percent of dust particles more than 1 micron in diameter are typically removed by standard office filtration system. The development of telecommunication networks has resulted in more electronic functionality in outdoor locations, such as telecommunication cabinets, which are usually located close to customers in outdoor environments. In addition, free air cooling methods are being adopted by information and communication companies,

including Intel, Google, and Microsoft, as a means of reducing energy costs and greenhouse gas emissions [1][2]. This method uses ambient outdoor air to cool the equipment directly, thereby reducing the energy consumed in cooling and conditioning the air. In a free-air cooled data center, for example, there is usually minimal contamination control under fresh air conditions in data centers, thus, dust contamination could be significant. The increasing power density brought on by shrinking feature size in electronic devices requires that enhanced cooling be provided to equipment cabinets. This cooling is frequently accomplished using forced air. As air velocity across surfaces increases, dust particle deposition velocity also increases, up to 100 times [8]. This greatly enhanced accumulation rate leads to rapid deposition of particles on circuit boards, component, and the leads which connect them. Dust has become a critical environmental factor to impact the reliability of the electronics.

Compositional analysis of dust has been conducted to understand their effects on reliability [3] [30] [4] [29] [28]. It was shown that dust has a complex nature in that it contains more than tens of compositions [28]. Dusts from different locations can have similar compositions but differ in the weight percentages of the substances. Dust can serve as a source of ion contaminations, which can dissolve in moisture film and form conductive paths under certain temperature and relative humidity conditions [12]. There are two major failure mechanisms associated with ion contaminations: loss of impedance (i.e., loss of surface insulation resistance) and electrochemical metal migration between traces. Some experimental studies of dust have been conducted in the past [11] [6] [5] [10] [57]. Some experiments were conducted using artificial dust, that is, a mixture of

various chemical compounds to simulate the effect of natural dust. The others use natural dusts collected from field. There are also industry standard dusts such as Arizona road dust which have been used in reliability tests [87][11].

Among the published results on dust, there is still a lack of experimental study, particularly with natural dusts. There are published results on failures that are caused by dust. But the experiment is not well controlled and the data is not well analyzed. In addition, there are many speculations on the effects of dust, drawn from the research results in ion contaminations [12][5]. For example, since dust contains hygroscopic salts, it has been claimed that the impact of dust is determined by the critical relative humidity of the hygroscopic compounds in the dust [12][34][78][6]. Thus it is recommended that the most important parameter in dictating the impact of dust is relative humidity [5]. These claims are not supported by data due to the lack of experimental studies with natural dusts.

Natural dust is difficult to obtain in quantities needed for experiments, and it is a complex mixture with many substances; researchers tend to use a single salt, a mixture of a few chemicals, or mixtures of a few chemicals with Arizona test dust as substitutes [11][6][8]. However, the use of the mixtures is not yet justified with experimental data. For example, if there were evidence that dusts from different locations caused impedance degradation and the variations in the impedance degradation were negligible, then one would have more confidence in using a mixture with known compositions or an existing standard dust in place of all natural dusts for reliability tests. If experiments show that the variation

is large, using a single dust as the representative of dusts in the field is not sufficient. It remains to show whether the Arizona test dust is a good representative for all natural dusts.

The variation in dust compositions has led to the question of how to characterize dusts. It has been discussed that dust can be categorized by their locations, or characterized based on their ion species, concentrations, or pH of the solutions [83][88][89]. It remains to learn what characteristics can be used to classify dusts regarding the failure mechanisms such as loss of impedance or ECM.

This thesis presents an experimental study of the impact of natural dusts on reliability. Natural dusts were collected from different locations. Four different dust samples were compared in order to evaluate the differences in their impacts on reliability: natural outdoor and indoor dust samples from Massachusetts, U.S., natural outdoor dust from Tianjin, China, and the ISO standard test dust (Arizona test dust). Dust samples were transferred onto the test boards with comb structure using volatile solvent, by which the dust deposition densities on the printed test boards are well controlled and verified by the weight change before and after dust deposition on different boards. In addition to the conventional DC measurement, Electrochemical impedance spectroscopy and equivalent circuit modeling were adopted in this study. EIS was shown to help understand the underlying mechanisms of ion contaminations [90][91][92]. The impact of dust on loss of impedance in printed circuit boards was determined under controlled temperature (20°C to 60°C) and relative humidity (50% to 95%) conditions. The impact of dust on

electrochemical migration and corrosion was evaluated under temperature-humidity-bias tests (50°C, 90% RH and 10 VDC). Time-to-failure was quantified. To further analyze the differences in the characteristics, moisture sorption test, SEM/EDS compositional analysis, ion species/concentration analysis, and conductivity and pH measurements of the dust aqueous solution were performed.

The experiments with natural dust has demonstrated dust contamination on PCB in controlled temperature (20°C to 60°C) and relative humidity (50% to 95%) conditions can cause loss-of-impedance failures. It is also demonstrated that natural dust at 50°C / 90% RH with 10V bias can cause electrochemical migration. Critical transition ranges of relative humidity were identified for different types of dusts. Beyond the critical range, the impedance of contaminated PCBs showed a sudden drop and degraded by orders of magnitude. The critical transition range provides evidence to support the argument that the impact of dust on loss of impedance is largely dependent on the CRH of its hygroscopic compounds.

Large variations were observed in the comparison of different dusts. The impedance of PCBs contaminated with natural dust was lower than that of the boards contaminated with ISO dust in the temperature and relative humidity tests by orders of magnitude (up to 10^3). A degradation factor to quantify the degradation of impedance for different dust was established to measure the difference in impedance between contaminated boards and clean boards. All four dusts show different degradation factors and the Arizona test dust has the lowest degradation factor. All the natural dust contaminated test boards

showed lower times-to-failure (up to 4 times) than the ISO test dust in the temperature-humidity-bias tests. The experimental data indicated that variations of different dusts in impedance degradation and time-to-failure in ECM tests are not negligible. It also demonstrated that using the ISO standard test dust in place of natural dust samples for reliability evaluation could lead to inaccurate results.

Among the different ways of characterizing dust, it was found that moisture sorption capability test characterized the hygroscopic property of dust and can be used to classify different dusts regarding the loss of impedance failure. The dust with the highest weight gain in the moisture sorption capability test had the highest impedance degradation. Ion species/concentration or conductivity of dust aqueous solution can be used to classify dust regarding the electrochemical migration related failures. Dust with the highest ion concentration and conductivity had the lowest time-to-failure.

In addition to the experimental study, failure analysis of a number of field return products in telecom industry was performed. The field return products exhibited the same failure mechanisms as produced in the lab tests, which further confirms the applicability of the experimental results.

This thesis is organized as the following. Chapter 2 reviews the background on dust. Chapter 3 discusses failure mechanisms related to dust, test methods and time-to-failure models in the literature. Chapter 4 reviews the impedance measurement and equivalent circuit modeling. Chapter 5 discusses the experimental approach employed in this thesis

to investigate the effects of dust. Chapter 6 presents the experimental results from the research. Chapter 7 discusses the findings in the experiments. Chapter 8 presents failure analysis of field failures caused by dust contaminations. Chapter 9 concludes this thesis with a summary.

Chapter 2: Background on Dust

This chapter introduces the basic properties of natural dust and discusses dust samples used in reliability tests.

Natural Dust Properties

Dust is defined as fine, dry particle matter consisting of particles of earth or waste matter lying on the ground or on surfaces or carried in the air. In the electronics and electrical industries, there is no formal definition of dust in the electronic industry. A variety names have been applied to dust including atmospheric dust, airborne particles, and particulate contaminations. Dust is known to have a complex nature in terms of its composition and characteristics. Dust from different locations can have similar compositions, but the weight percentages of the composite substances may differ. Three critical properties of natural dust are discussed in this chapter: dust particle size, dust compositions and dust contaminant levels in the literature.

Dust particle sizes and sources

Based on the size the dust particles, they are categorized in two groups: *fine mode* particles and *coarse mode* particles [30]. The fine mode particles are defined as the diameter of the particle less or equal to 2.5 μm . They are normally generated through the condensation of low-volatility gases, followed by the coalescence of a number of these nuclei to create larger particles. For example, ammonium sulfate in the dust is normally formed by combination of gaseous ammonium and sulfur dioxide. The name

“accumulation mode” is also used for the fine particle group. The coarse mode group is defined as the diameter of the particles greater than 2.5 μm . They are generated by a variety of mechanical processes such as wind-blowing of soil dust, breaking ocean wave of sea salt and industrial machining. There is no feasible way to convert the smaller particles into larger particles or vice versa. As a result, the physical and chemical properties of the two modes can be treated quite independently. The typical size range for some types of aerosol particles is shown in Figure 1.

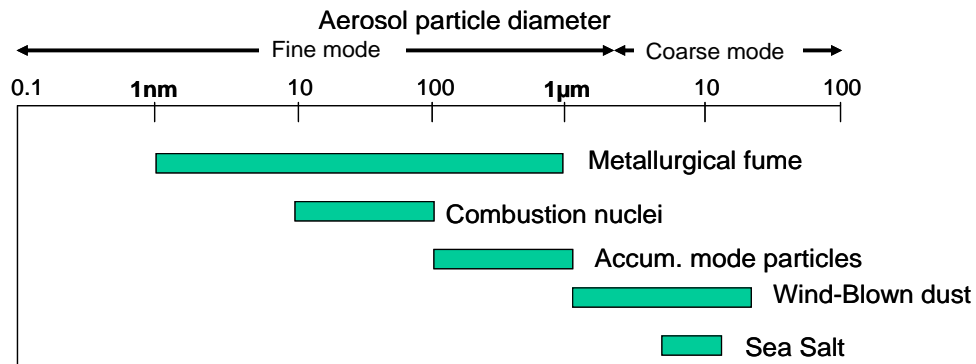


Figure 1: Typical size ranges for some types of aerosol particles

The number of the two groups of particles is generally different as well. Accumulation mode particles outnumber those in the coarse mode by a factor of a thousand or more, and have around ten times the surface area. Because the particle volume is proportional to the cube of the radius, so the ensemble volume of the coarse mode particles approaches that of the fine mode particles. Figure 2 shows the normalized frequency plots of the number and volume distribution as a function of the grand average 1969 Pasadena aerosol [4].

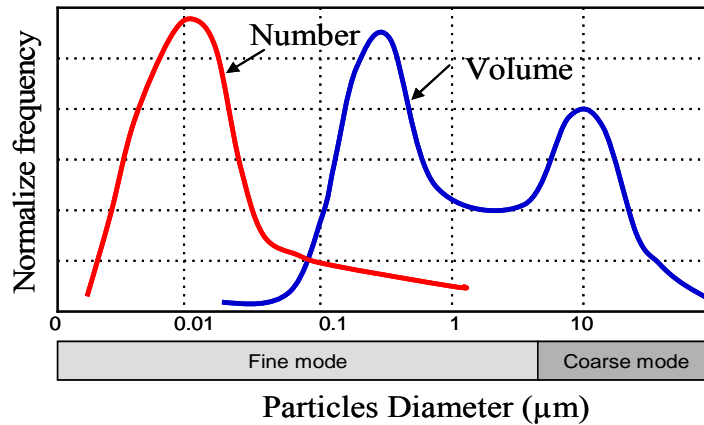


Figure 2: Schematic drawing of normalized frequency plots of the number and volume distribution as a function of the grand average 1969 Pasadena aerosol

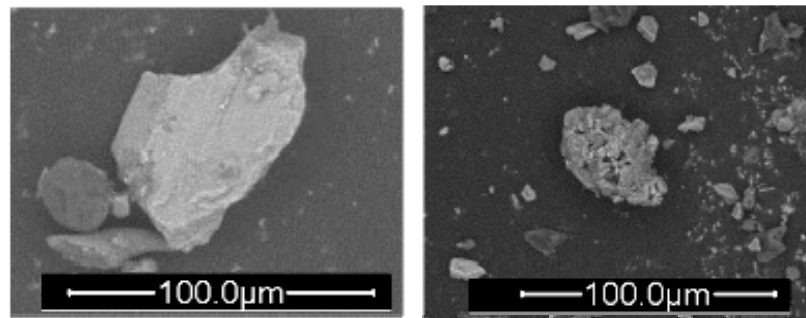
Compositions and key ions

Dust particles consist of both inorganic and organic substances, but the inorganic substances typically outweigh the organic substances. Some of the inorganic compounds are water-soluble salts. There are many types of inorganic mineral particles in dust [29], including quartz sand (SiO_2), feldspar (KAlSi_3O_8 - $\text{NaAlSi}_3\text{O}_8$ - $\text{CaAl}_2\text{Si}_2\text{O}_8$), calcite (CaCO_3), mica ($\text{SiO}_2 \cdot \text{Al}_2\text{O}_3 \cdot \text{K}_2\text{O} \cdot \text{Na}_2\text{O} \cdot \text{H}_2\text{O}$), and gypsum ($\text{CaSO}_4 \cdot 2\text{H}_2\text{O}$). Some of their inorganic compounds are water-soluble salts. The relative content of the main minerals is listed in Table 1. X-ray powder diffraction (XRPD), electron probe microanalysis (EPMA) and transmission electron microscopy (TEM) have been used to analyze the mineral [28]. Organic substances in dust include carbon black, fibers, and organic ions such as formate (COOH^-) and acetate (CH_3COO^-) [4]. Organic compounds can be analyzed by gas chromatography/mass spectrometry (GC/MS). The weight percentage of organic compounds and carbon black can be evaluated by thermo gravimetric analysis (TGA).

Table 1: Relative contents of main mineral particles in dust.

Minerals	Main Compositions	Relative Contents	
		Nature dust (size < 250 μm)	Fine particles (size < 10 μm)
Quartz	SiO_2	1	1
Feldspar	$\text{KAlSi}_3\text{O}_8\text{-NaAlSi}_3\text{O}_8\text{-CaAl}_2\text{Si}_2\text{O}_8$	0.77	0.8
Calcite	CaCO_3	0.48	1.91
Mica	$\text{SiO}_2\cdot\text{Al}_2\text{O}_3\cdot\text{K}_2\text{O}\cdot\text{Na}_2\text{O}\cdot\text{H}_2\text{O}$	0.41	2.24
Gypsum	$\text{CaSO}_4\cdot 2\text{H}_2\text{O}$	0.05	0.72

Dust particles with sharp boundaries are normally mineral dust particles, as shown in Figure 3 (a). Some dust particles are agglomerations of many particulates, which together form multi-layer structures, as shown in Figure 3 (b). Mineral particles normally form the core, and inorganic salts and organic materials are attached to that core [4], as illustrated in Figure 4.



(a) Mineral dust particles (b) Multi-layer structure dust particles

Figure 3: Examples of dust particles.

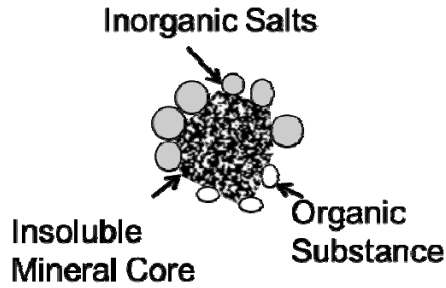


Figure 4: Schematic drawing of multi-layer structure of dust.

The ionic contents in dust particles are of interest when considering the impact of dust on reliability because they can dissolve in water and conduct electricity. When dust dissolves in water, the major cations and anions are NH_4^+ , K^+ , Na^+ , Ca^{2+} , Mg^{2+} , Cl^- , F^- , NO_3^- , and SO_4^{2-} [29]. In fine dust particles, the ionic components are mainly sulfate and ammonium. The ammonium to sulfate ratio is generally one to two. The formula can be written as $(\text{NH}_4)_{2-x}\text{H}_x\text{SO}_4$, where x can be 0 or 1. In coarse particles, sulfate, ammonium, calcium, magnesium, sodium, and chloride are the most prevalent ionic components, with large local variations for magnesium, sodium, and chloride [12].

Next, chemical and electrochemical properties of some ions often found in dust or encountered in PCBs are discussed, including chloride, bromide, sulfate, sodium, ammonium and potassium [13].

Chloride (Cl^-)

Chloride is one of the most detrimental materials in dust. Chlorides will generally accelerate electrochemical failure mechanisms, such as metal migration and electrolytic corrosion, when combined with moisture and an electrical bias.

Minzari et al. [56] researched the effect of chloride contamination content on the electrochemical migration of a Sn metal layer of chip resistors in a condensed environment. It was found that a higher chloride concentration (10 ppm~1000 ppm) increases the dissolution rate of Sn metal at the anode, makes the dendrites grow more branches over a wider area, and increases the amount of dissolved Sn ions at the anode so that they exceed the solubility limit and lead to the precipitation of tin hydroxides when combined with a relatively high potential (12 V). Additionally, dendrites grown at a higher chloride concentration bear a larger resistance, due to the mixture of Sn dendrites and tin hydroxides. The charges that pass through the electrolyte at a higher concentration of chloride are lower, due to the intermittent burning and re-growth of dendrites.

Bumiller, et al [69] observed that chloride can trigger dendritic growth and uniform corrosion on HASL plated copper metallizations depending on the chloride contamination levels used. A 10 V bias was applied across copper metallizations (6.25 mil, 12.5 mil and 25 mil spacings) contaminated by controlled surface chloride concentrations under 85°C and 85%RH for 168 hours. It was found that below 20 $\mu\text{g}/\text{in}^2$ of chloride, dendritic growth dominated. From 20 $\mu\text{g}/\text{in}^2$ to 50 $\mu\text{g}/\text{in}^2$, both dendrites and uniform corrosion occurred. Above 50 $\mu\text{g}/\text{in}^2$, uniform corrosion dominated.

Weekes [70] investigated the added amount of chloride by soldering process to bare PCBs. It was found that 3 $\mu\text{g}/\text{in}^2$ was added to bare PCBs by using no-clean flux and 8 $\mu\text{g}/\text{in}^2$ was added by using water soluble flux. SIR testing and ion chromatography (IC)

testing were also conducted to test the maximum acceptable amounts of chloride on bare board and assembled boards. It was found that when using no clean flux $2.5 \mu\text{g}/\text{in}^2$ and $3 \mu\text{g}/\text{in}^2$ were the maximum acceptable amounts for bare boards and assembled boards, respectively, and $6 \mu\text{g}/\text{in}^2$ and $8 \mu\text{g}/\text{in}^2$ when using water soluble flux.

Flux chemistry directly influences the tolerance for chloride on an assembly. An assembly processed with high-solids rosin fluxes (rosin activated (RA) or rosin mildly activated (RMA)) can tolerate higher levels of chloride due to the encapsulating nature of the rosin. No-clean fluxes, in which very low levels of rosin or resin are used, do not have this encapsulating protection. Therefore, they require lower levels of chloride in flux on final assemblies. IPC [71] recommends a $10 \mu\text{g}/\text{in}^2$ NaCl equivalent ionic residue as the maximum acceptable contamination level for PCBs, while the National Defense Centre for Environmental Excellence (NDCEE) recommends a $2.5 \mu\text{g}/\text{in}^2$ as the maximum acceptable contamination level for chloride on PCBs [73].

Bromide (Br^-)

Bromide is generally attributable to the bromide fire retardant added to epoxy-glass laminates for fire resistance. At high temperatures such as 1000°C [74], the flame retardant material decomposes into a mixture of HBr and Br_2 gases, which, in turn, dissolve into the surface moisture film and turn into bromide ions. The emission of HBr gas reached a peak at 375°C when a brominated epoxy resin (26% bromine by weight) is heated from 100°C to 700°C at a constant ramp rate of 10°C per minute [75]. Bromide can also come from solder masks, marking inks, or fluxes that have a bromide activator

material. When from the fire retardant, bromine is not a material that typically degrades the long-term reliability of electronic assemblies. If bromide comes from a flux residue, it can be as corrosive as other halides. Since hydrobromic acid is a strong acid, bromide does not change the pH value in the moisture film. Since bromide has a slightly higher mobility ($78.15 \text{ S}\cdot\text{cm}^2/\text{mol}$) [76] than chloride ions, bromide can also increase the conductivity of the surface moisture film when it exists in the film, thus lowering the surface insulation resistance (SIR).

Most bromide salts are soluble, except CuBr , AgBr , and PbBr_2 , which have very low solubility. Therefore, when Cu^+ , Ag^+ , and Pb^{2+} exist with bromide, they can precipitate out locally before leading to metal migration. The level of bromide varies depending on the porosity of the laminate and/or mask, the degree of over/under cure of the laminate or mask, or the exposure times to reflow temperatures.

For epoxy-glass laminate, bromide levels typically fall within the range of $0\sim 7 \mu\text{g}/\text{in}^2$, depending on the amount of fire retardant materials added [70]. With several exposures to reflow conditions, $6\sim 7 \mu\text{g}/\text{in}^2$ bromide can be added to the surface by using no-clean and water soluble flux [70]. Bumiller et al [69] found that the bromide on the surface detected to be $0.1 \mu\text{g}/\text{in}^2$ prior to SIR testing (85°C , $85\% \text{ RH}$ and 10 V) increased to about $12 \mu\text{g}/\text{in}^2$ after the testing. Since water soluble flux requires cleaning, the maximum acceptable amount for bromide on bare boards using water soluble flux is $15 \mu\text{g}/\text{in}^2$ compared to $5.5 \mu\text{g}/\text{in}^2$ when using no clean flux [70]. A maximum acceptable bromide

contamination level of 15 $\mu\text{g}/\text{in}^2$ on PCBs is recommended by the National Defense Centre for Environmental Excellence (NDCEE).

Sulfate (SO_4^{2-})

Sulfate, when present in sufficient quantity, can be harmful for electronic assemblies. Sulfates can come from a variety of sources, such as sulfur-bearing papers or plastics, etching, or acid processes in fabrication, but these residues most often originate from tap water rinsing / cleaning. One possible source of high sulfate may be the solder mask itself. Some solder mask formulations incorporate sulfur-bearing compounds as fillers, dyes, and matting agents.

Another source of sulfate is the fine air born particles (0.05~2 μm), which are rich in $(\text{NH}_4)_2\text{SO}_4$ [77]. When the fine particles are adsorbed onto the surface of PCBs and dissolve into the moisture film, they create an electrolyte consisting of SO_4^{2-} and NH_4^+ with a weak acidity, although a critical humidity is required to enable the moisture film to transport metal ions. Because it is more difficult to remove these fine particles by air circulation systems, compared to coarse particles (2~15 μm) [77], they pose a serious corrosion problem to exposed electronic systems, either indoors or outdoors.

When the bare board is subjected to the ion chromatography extraction procedure, the sulfates are pulled from the mask. As with bromide, when the sulfate residues are from within the mask itself, they are not detrimental. However, the existence of sulfate ions can increase the surface moisture film conductivity and help increase the metal ion

stability in the film through complexation, thus increasing the probability of metal migration. When sulfate levels start rising appreciably above $3.0 \mu\text{g}/\text{in}^2$, a sulfate-bearing chemical, such as sodium/ammonium persulfate or sulfuric acid, is suspected to be used in the process. As a conservative stance, a sulfate level above $3.0 \mu\text{g}/\text{in}^2$ is considered to be corrosive and detrimental to circuit reliability.

Sodium (Na^+)

The standard electrode potential of Na relative to the standard hydrogen electrode potential is -2.71 V [14], so Na metal is highly reductive. That is why sodium exists in the environment only as a compound and never as a free element.

Na^+ is very stable in water, always existing as counter ions to many anions, with the most abundant sodium compound being NaCl in sea water. In general, the sodium compound is highly soluble in water, especially when the counter anions are halides, sulfates, nitrates, carboxylates, and carbonates, with the exception of sodium bismuthate (NaBiO_3) [15]. The limiting ionic conductivity of Na^+ is $50.11 \text{ S}\cdot\text{cm}^2/\text{mol}$, almost two thirds that of chloride ions, so the existence of Na^+ in the surface moisture film can increase the conductivity and lower the SIR of PCBs.

In electronics manufacturing, Na^+ is found in some fluxes as the counter ion to the acid activator, such as sodium succinate or sodium adipate. It is also found in the solder mask as absorbed residue and can be conductive through or on top of the mask. Levels of less than $3.0 \mu\text{g}/\text{in}^2$ have good field performance.

Ammonium (NH_4^+)

Ammonium can be the product of the chemical reaction of ammonia (NH_3) with hydrogen ions. When one or more hydrogen atoms of ammonia are replaced by organic substituents, such as the alkyl and aryl groups, the derivative $\text{NH}_n\text{R}_{3-n}$ is called amine. If n is 2, it is called the primary amine; if n is 1, it is called the secondary amine; and if n is zero, it is called the tertiary amine. So, amines are structurally analogous to ammonia, still containing nitrogen as the key atom. Amines with some inorganic acids are often used as activators in soldering flux. Much of the amines used in electronic assembly are in board fabrication as etchants, HASL flux residues and some water soluble fluxes and solder paste materials.

Ammonium (NH_4^+) is mildly acidic ($pK_a=9.25$) [16], through the dissociation of ammonium ions into ammonia and hydrogen ions. Ammonium can complex with hydroxide ions, leaving hydrogen ions in the solution to be acidic. Most of the ammonium salts are very soluble in water. Since the limiting ionic conductivity of ammonium ions is $73.7 \text{ S}\cdot\text{cm}^2/\text{mol}$ [14], almost equally conductive as potassium ions and chloride ions, the existence of ammonium can also lower the SIR of PCBs when moisture is present.

Potassium (K^+)

Similar to sodium, potassium metal is highly reductive, so potassium exists in nature only as compounds. Since its standard electrode potential is -2.92 V [14], even lower than

sodium, it is more reductive than sodium. But, potassium ions are very stable in water. One effect of potassium and sodium ions is that the potassium and sodium ions, as the supporting electrolytes in the electroplating of microvias, can provide a better filling capability than hydrogen ions [17].

Potassium compounds generally have excellent water solubility, due to the high hydration energy of the K^+ ion. The potassium ion is colorless in water. Since the limiting ionic conductivity of potassium ions is $73.5 \text{ S}\cdot\text{cm}^2/\text{mol}$, it is almost equally as conductive as ammonium ions and chloride ions, and more conductive than sodium ions. Potassium in electronics is found in the dry film solder mask materials. The amount of potassium found in electronics is typically low, but a concentration level greater than $3.0 \mu\text{g}/\text{in}^2$ has been seen to cause leakage problems.

Indoor and outdoor dust contamination levels

The density of dust in the air and the weight percentage of some key dust compositions vary from location to location, depending on the distance to pollution sources and local pollution control. Some researchers categorize dusts as urban, industrial, or marine, based on their original location. The combined mass of fine and coarse particles in the atmosphere is frequently referred to as the total suspended particulate (TSP). The TSP of dust varies from country to country. So far there was no standard which provides the criteria for dust deposition density [28] related to dust impact on the reliability of electronics. The critical deposition density is related to the composition of dust contamination.

Some recent studies [78] have shown that typical TSP levels are 30–40 $\mu\text{g}/\text{m}^3$ outdoors and 5 $\mu\text{g}/\text{m}^3$ indoors for telecommunications equipment rooms in the U.S. Typical sulfate levels are 4–6 $\mu\text{g}/\text{m}^3$ outdoors and 0.6–0.8 $\mu\text{g}/\text{m}^3$ indoors. In many parts of Asia, the TSP concentration of dust is much higher. TSP levels in excess of 200 $\mu\text{g}/\text{m}^3$ have frequently been measured outdoors. The sulfate portion of this mass is frequently in excess of 15 $\mu\text{g}/\text{m}^3$. Indoor TSP concentrations are frequently in excess of 30 $\mu\text{g}/\text{m}^3$. The Telecorida standard GR-63-CORE [54] lists the dust contaminant levels based on their study. The average yearly levels of indoor and outdoor contaminants are 20 $\mu\text{g}/\text{m}^3$ and 90 $\mu\text{g}/\text{m}^3$, respectively.

Dust Samples Used in Accelerated Tests

Researchers used different dust samples to evaluate dust impact. One key difference is the dust compositions used in the tests. Some tests use a single or mixture of known substance like hygroscopic salts to simulate the natural dust. The others use natural dusts collected from indoor or outdoor environments. There are also standard dusts (such as Arizona road dust) which can be purchased. It has been suggested that the compositions of dust particles are too simple which may not be able to represent the complexity of real dust.

DeNure and Sproles [11] used hygroscopic salts to simulate some of the most severe conditions found in service environments to test the dust impact on connectors. The salt composition was similar to that of natural dusts, except that nitrates were not used for

safety reasons. Hard mineral particles were included to provide a substance with the mechanical strength to hold the contacts apart if the dust got into the interface. The mineral particles used were Arizona road dust. Table 2 shows the composition of the test dust used in [11].

Table 2: Composition of test dust used in other research

Component	Weight %
Arizona Road Dust	66
NaHCO ₃	1
KCl	1
NH ₄ HPO ₄	3
(NH ₄) ₂ SO ₄	29

Sandroff and Burnett [6] identified a single salt to simulate SIR degradation failures related to hygroscopic dust. The effects of different salts on PCB insulation resistance were studied, with varied relative humidities. Sodium sulfide provides the highest sensitivity in resistance variation over the humidity range of 30~100%. Although it is not typically found in airborne hygroscopic dust, it offers a controllable technique to simulate the loss of SIR. Therefore, a 1/10M sodium sulfide solution was used to qualify the printed circuit boards.

Lin and Zhang used natural dust collected from fields to evaluate dust effect on corrosion [10]. The dust samples were collected from three locations: an office area in Beijing, a storehouse in Shanghai, and a workshop in Shanghai. The collected dust particles were dissolved in distilled water. The solution was dispersed by an ultrasonic cleaner, heated

and naturally cooled down, and filtered by filter paper. The dust solution was dripped on the test sheet with a burette, after each previous droplet of solution evaporated.

GR-63-CORE [54] describes a “Hygroscopic Dust Test Method”, in which the PCBAs is coated with a single component hygroscopic solution with undefined composition and then exposed to high humidity to lower the SIR. This test requires products to pass functional tests after moisture soak.

There are some standard test dusts, such as ISO and ASHREA test dust as listed in Table 3. They are intended for the use of testing air filters and air cleaners. All of them contain a large percentage (up to 100%) of natural earth dust obtained in raw form from Arizona Test Dust. Arizona test dust is the dust that settles out of the air behind or around tractors or implements operating in the Salt River Valley, Arizona. The composition of Arizona test dust is listed in Table 4.

Table 3: Composition of Standard Test Dust

Test Dust	Arizona Test Dust	Carbon Black Power	Milled Cotton Linters
ISO 12103 -1, A1 Ultra fine Test Dust	100% (1 - 20 um)		
ISO 12103 -1, A2 Fine Test Dust	100% (1 - 120 um)		
ISO 12103 -1, A3 Medium Test Dust	100% (1 - 120 um)		
ISO 12103 -1, A4 Coarse Test Dust	100% (1 - 200 um)		
ASHREA Test Dust #1	72% (ISO A2)	23%	5%
ASHREA Test Dust #2	93.5% (ISO A2)		6.50%

Table 4: Composition of Arizona Test Dust

Chemical Ingredient	Weight Percentage (%)
SiO ₂	68 - 76
Al ₂ O ₃	10 - 15
Fe ₂ O ₃	2 - 5
Na ₂ O	2 - 4
CaO	2 - 5
MgO	1 - 2
TiO ₂	0.5 - 1.0
K ₂ O	2 - 5

Chapter 3: Dust related Failure Mechanisms, Test Methods and Models

Dust can increase the risk of several different failure mechanisms in PCBs [12]. In the presence of dust, a thicker water film can be formed on the substrate of PCBs due to moisture sorption by hygroscopic materials in the dust and capillary attraction by mineral particles. When the water-soluble salts in dust particles dissolve in the water film, they can produce ionic contamination. This can lead to a reduction in SIR to an unacceptable level by forming a conductive path between two adjacent electrodes. The ionic contamination can react with the metals on the board, such as copper traces, component leads, and solder materials, resulting in metal dissolution, which can corrode the metals. Under an electrical field, some metallic ions or metal complexes dissolved in the anode can migrate to the cathode to form dendrites. This failure mechanism is called electrochemical migration (ECM). One of the driving forces of ECM is an electrical field. When metal dendrites span the spacing between adjacent conductors, the leakage current between these conductors will increase. Intermittent failures occur when a dendrite grows, causing an electrical short and then a burn-out, because of the high localized current density. Permanent failures occur if a dendrite carries the current density, leading to a permanent short. The tendency of ion migration is also dependent on the solubility of the corrosion products at the anode. Metal compounds with low solubility product give fewer ions for migration. ECM and corrosion are normally accompanied by current leakage failure, which is measured as SIR degradation. SIR degradation indicates the

presence of ionic contaminants and water film formation on the substrate, which provides the incubation conditions for ECM and corrosion to occur. PCBs deposited with dust may fail very early because of the reduced SIR between the features in the presence of moisturized dust, before the bridging by dendritic growth.

Surface Insulation Resistance Degradation

Surface insulation resistance (SIR) degradation takes place on a printed board between the electric conductors when the conductors are connected by a substrate covered by an electrolyte formed by hygroscopic dust at elevated RH.

Hygroscopy is the ability of a substance to attract and hold water molecules from the surrounding environment. This is achieved through either absorption or adsorption. Hygroscopic substances include both water soluble and water insoluble materials. Examples are cellulose fibers such as cotton and paper, sugar, sulfuric acid, many fertilizer chemicals, many salts (including table salt), and a wide variety of other substances. Natural dust contains a lot of hygroscopic substances.

If there is a deposit of dust contamination with *water soluble* impurity on the substrate, an additional mechanism of liquid water formation will be triggered [7]. The impurity can be ionic or non-ionic as long as it is water soluble and substances like sugar may be quite effective [79]. The real difference between the ionic and non-ionic impurities, however, will be in the conductivity of thus liquefied water. Also, ionic substances form two or more species upon dissolution.

SIR degradation of a printed circuit board by hygroscopic dust is believed to follow two steps [34]: water condensation on impurities at a critical RH; bridging of the dust deposit between conductors.

When the relative humidity exceeds a critical RH, which corresponds to the water chemical potential of the saturated solution, water will condense until an equilibrium is established. In the context of hygroscopic dust we usually refer to this event as *deliquescence*. It is a first order phase transition from solid to solution that occurs at a relative humidity that is characteristic to the solid ingredient [80]. If it merely forms a crystalline hydrate it is termed hygroscopic. The relative humidity level is referred to as *Critical Relative Humidity* (CRH) in [71]. It is defined as the temperature and humidity level at which a material will begin to absorb water vapor from the air.

The values for CRH are tabulated in the literature for many substances shown in Table 5. For ammonium hydrogen sulfate, NH_4HSO_4 , as the main ingredient of hygroscopic dust, the CRH equals to 40% at 24°C. Most dusts deliquesce in the 40–80% RH range, which is within the operating range for most electronics. Thus, the presence of hygroscopic dust may cause loss of SIR at a relative humidity level lower than the 60% that is normally expected as the failure trigger point for clean surfaces [9].

Table 5: Critical relative humidity (CRH) for several inorganic compounds

Compound	Temp (°C)	RH (%)
NaCl	20	75
NaSO ₄	25	84
(NH ₄) ₂ SO ₄	25	79

$(\text{NH}_4)\text{HSO}_4$	24	40
$(\text{NH}_4)_3\text{H}(\text{SO}_4)_2$	25	69
NH_4NO_3	24	65

A continuous bridge from particle to particle must be formed in order to have an uninterrupted conductivity path after the deliquescence step. A network of dust particle needs to be formed in order to make a change from an insulator to a conductor between two conductors. The conductivity due to percolation is a very sharp function of surface coverage by dust particles.

Tencer and Weschler used percolation theory to model the threshold of dust mass surface density to cause the bridging [7], [81]. But this model oversimplified dust composition, and was not verified by any experimental data. From the percolation theory it follows that the probability of connectivity is 90% when 53% of possible dust adherence sites are occupied [35]. Assuming a median mass diameter to be $0.52 \mu\text{m}$ and that their density is that of ammonium hydrogen sulfate (NH_4HSO_4), the main dust ingredient (1.78 g/cm^3), Weschler estimated that the bridging will occur at the mass surface concentration of $24.2 \mu\text{g/cm}^2$. Tencer showed that at high humidity the critical surface concentration in such systems is independent of the average particle size or the particle size distribution. Weschler's estimation was based on dry concentration of particles, however, and the diameter of deliquescent particles after they absorb water will be somewhat larger. Dry NH_4HSO_4 increases its cross-section area by a factor of approximately 1.45 at the deliquescence point. Tencer took into account that the particles contain a significant amount of insoluble material (e.g., silica) besides salts, and estimated to use $15 \mu\text{g/cm}^2$ value as the "magic number".

Electrochemical Migration

Electrochemical migration (ECM) is the loss of insulation resistance between two conductors (trace, pad, plated-through hole) due to the growth of conductive metal filaments [36]. The rate of electrochemical migration has four prerequisites: a mobile metal, a voltage gradient, a continuous film, and soluble ions [79]. ECM occurs as a result of metallic ions being dissolved into a medium at the anode and plating out at the cathode in needle- or tree-like dendrites. Such migration may reduce isolation gaps and eventually lead to an electrical short that causes catastrophic failure [40]. [40] shows a schematic representation of ECM the process according to the so-called classical model. The anodically dissolved metal ions (M^{n+}) can migrate to the cathode. They are deposited there by obtaining electrons (e^-) and reducing back to metal. The classical model was first demonstrated for the migration of silver [39]. Further investigations have proven that the model also applies to several other commonly used metals in electronics, such as copper, lead, and tin [40][41].

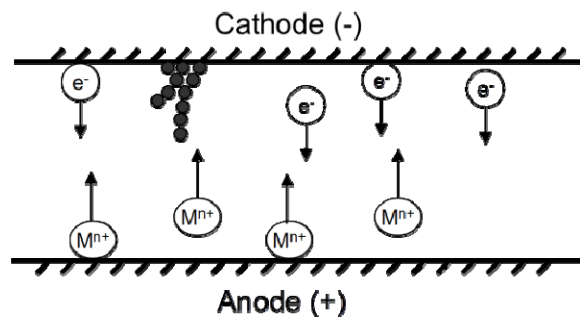


Figure 5: A Schematic Representation of the ECM Phenomenon

Dendrite growth normally develops when an electrolyte bridges two electrodes to form a path. The metal ions are formed by anodic dissolution. Anodic corrosion involves the

oxidation of metals to generate cations at the anode. Dissolved ionic contaminants, such as halides, can promote this process. Then, metal ions migrate through the electrolyte under the influence of electromotive forces toward the cathode. Electrochemical metal deposition at the cathode is the last step. As more and more neutral metal deposits on the nuclei, dendrites or dendrite-like structures may grow toward the anode. When a dendrite fully spans the gap between adjacent conductors and touches the anode, a short may occur. The current flowing through a dendrite may burn out part of the dendrite due to Joule heating. This phenomenon can lead to intermittent failures, which can be recurrent if re-growth and fusing occur cyclically. If the dendrites are thick enough to withstand the current, a permanent short can result [42].

Under the bias voltage, the metal at the anode goes into the solution, migrates toward the cathode, and plates out at the cathode. The susceptibility of different metals to ECM is affected by the electrode potential energy of metal ions from metal dissolution. The standard electrode potentials of some main metals used in electronics are listed in Table 6. The metals become more likely to corrode going from the noble metal gold to nickel. Because gold has a high standard electrode potential, an electroless nickel immersion gold (ENIG) finish has a high resistance to ECM. Silver also has a relatively high standard electrode potential, but it is well known for its tendency to form migratory shorts. Silver is more susceptible to migration than other metals because it is anodically very soluble and its hydroxides also have good solubility. Moreover, silver is unlikely to form a passivation oxide layer. Note that the relative position of the material in the list in Table 6 changes in other environments, such as in the presence of sea water.

Table 6: Standard Electrode Potentials in an Aqueous Solution at 25°C

Cathode (Reduction) Half-reaction	Standard Electrode Potential E° (volts)
$\text{Au}^{3+}_{(\text{aq})} + 3\text{e}^- \rightarrow \text{Au}_{(\text{s})}$	1.50
$\text{Ag}^{+}_{(\text{aq})} + \text{e}^- \rightarrow \text{Ag}_{(\text{s})}$	0.80
$\text{Cu}^{2+}_{(\text{aq})} + 2\text{e}^- \rightarrow \text{Cu}_{(\text{s})}$	0.34
$\text{Sn}^{4+}_{(\text{aq})} + 2\text{e}^- \rightarrow \text{Sn}^{2+}_{(\text{aq})}$	0.15
$\text{Pb}^{2+}_{(\text{aq})} + 2\text{e}^- \rightarrow \text{Pb}_{(\text{s})}$	-0.13
$\text{Sn}^{2+}_{(\text{aq})} + 2\text{e}^- \rightarrow \text{Sn}_{(\text{s})}$	-0.14
$\text{Ni}^{2+}_{(\text{aq})} + 2\text{e}^- \rightarrow \text{Ni}_{(\text{s})}$	-0.23

Particulate contaminations, such as airborne dust and gaseous contaminations, can also contribute to ECM processes. Without air-conditioning, gaseous and particulate contaminations in the atmosphere have a larger impact on the corrosion reliability of electronics [82]. During an ECM process, the electrolyte path is formed by the adsorbed moisture layer or water condensation, which has conductive properties. The conductivity of the water layer can be enhanced by dissolved dust or adsorption of some gases that form ions with water.

Electrochemical Corrosion

Electrochemical corrosion is the result of the displacement of one element in one phase (usually in an aqueous solution) by another element originally present in another phase (in the solid form as a metal or alloy). It is always accompanied by a flow of electric current due to displacement. Electrochemical corrosion takes place in a cell in which the less noble material (anode region) corrodes. A complete corrosion cell consists of an anode and a cathode electrically connected by an external electronic path (circuit) and an internal ion path (electrolyte). Three typical types of corrosion cells are discussed below.

Galvanic cells, also known as composition cells, arise when two metals with dissimilar compositions or microstructures come into contact in the presence of an electrolyte. One common example occurs when two single-phase dissimilar metals, such as nickel and gold, come into contact. The metal that is higher in the electrochemical series will be the cathode. The other metal will suffer anodic reactions and corrode. This can also happen with a metal alloy composed of multiple phases, such as an aluminum alloy. The individual phases possess different electrode potentials, resulting in one phase acting as an anode and becoming subject to corrosion.

Concentration cells can occur when electrodes are in contact with different ion concentrations. Consider a metal bathed in an electrolyte containing its own ions. The basic corrosion reaction involves a metal atom losing an electron and entering the electrolyte as an ion. It can proceed both forward and backward, and will eventually reach equilibrium. If a region of the electrolyte (adjacent to the metal) were to exhibit a decreased concentration of metal ions, it would become anodic to the other portions of the metal surface. As a result, this portion of the metal would corrode faster as it increased the local ion concentration. The local corrosion rates are modulated in order to even out ion concentrations within the electrolyte. One of the most common concentration cells is dissolved oxygen. When oxygen has access to a moist metal surface, corrosion is promoted. However, this occurs most often when the oxygen concentration is lowest. As a result, sections of a metal that are covered by dirt or scale will often corrode faster, since the flow of oxygen to these sections is restricted. An

increased corrosion rate will lead to increased residue, further restricting the oxygen flow and worsening the situation. Pitting often results from this “runaway” reaction.

Stress cells can occur when the two electrodes are the same, the electrolyte is uniform, and one electrode is more mechanically stressed than the other. The area of high stress is always the anode of the cell. Stress cells can take on two basic forms. One has its anode established by residual internal stress, such as is created when metal is cold-worked. In the other type of stress cell, the metal is part of some kind of structure that is under high local stress, such as fastened bolts. A stress cell can exist in a single piece of metal where a portion of the metal's microstructure possesses more stored strain energy than the rest of it. Metal atoms are at their lowest strain energy state when located in a regular crystal array. By definition, metal atoms located along grain boundaries are not in a regular crystal array. The increased strain energy at the grain boundaries translates into an electrode potential that is anodic to the metal in the grains. Thus, corrosion can selectively occur along grain boundaries.

Atmospheric corrosion

Atmospheric corrosion is one of the predominant forms of electrochemical corrosion because of the varied working atmospheres for electronic equipment. It is a ubiquitous form of corrosion that affects many types of materials that have been exposed to the environment without first being immersed in a bulk electrolyte. Atmospheric factors affecting corrosion include pollutants (gases, dust, and sea salts), relative humidity, temperature, precipitation (acidity, intensity, duration, and form), solar radiation

(intensity and duration), and wind (speed and direction). Atmospheric corrosion can be classified into dry, damp, and wet categories. Thin moisture films (invisible electrolytes) are created at a certain critical humidity level for corrosion in damp conditions, while wet corrosion is associated with dew, ocean spray, rain water, water splashing, and so on.

Atmospheric corrosion tends to vary significantly in different locations; historically, it has been customary to classify environments as rural, urban, industrial, marine, or combinations of these. These types of atmosphere have been described as follows [83].

- Rural: This category is generally the least corrosive and normally does not contain chemical pollutants, but it does contain organic and inorganic particulates. The principal corrodents are moisture, oxygen, and, to a lesser extent, carbon dioxide (CO₂). Arid or tropical climates represent special extreme cases in the rural category.
- Urban: This type resembles the rural category in that there is little industrial activity. Additional contaminants are of the SO_x and NO_x variety, from motor vehicle and organic fuel emissions.
- Industrial: These atmospheres are associated with heavy industrial manufacturing facilities and can contain concentrations of sulfur dioxide, chlorides, phosphates, and nitrates.
- Marine: Fine windswept chloride particles, deposited on surfaces, characterize this type of atmosphere. Marine atmospheres are usually highly corrosive, depending on wind direction, wind speed, and distance from the coast.

In the presence of thin-film electrolytes, atmospheric corrosion proceeds by balancing anodic and cathodic reactions [59]. The anodic oxidation reaction involves dissolution of the metal, while the cathodic reaction is often assumed to be the oxygen reduction reaction. Corrosive contaminant concentrations can be high in thin electrolyte films, especially under conditions of alternate wetting and drying. Oxygen from the atmosphere is also readily supplied to the electrolyte under thin-film corrosion conditions. The mechanism of atmospheric corrosion is shown in Figure 6, in which the surface is considered as a “theoretical” clean surface for simplicity.

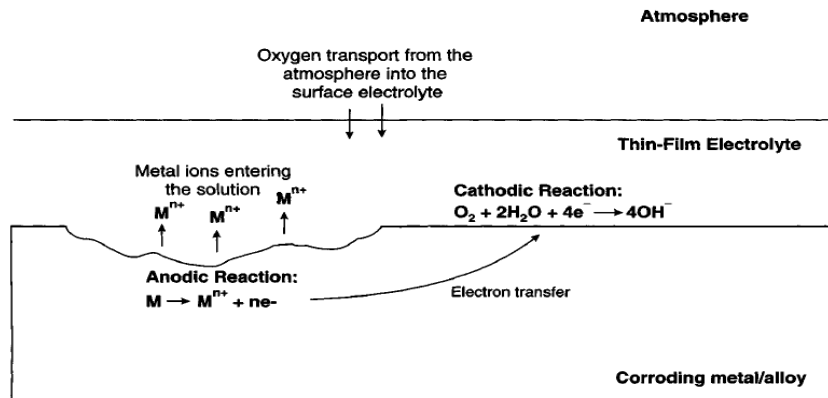
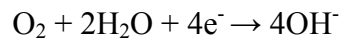


Figure 6: Mechanism of atmospheric corrosion [59]

For atmospheric corrosion in a near-neutral electrolyte solution, the following oxygen reduction reaction is the most likely to occur:



Research has shown that the overall rates of atmospheric corrosion are not controlled by the cathodic oxygen reduction process, but rather by the anodic reaction(s) [60]. The anodic half-cell process is shown in the simplified oxidation reaction as follows:



The formation of corrosion products (metal oxides and hydroxides), the solubility of corrosion products in the surface electrolyte, and the formation of passive films affect the overall rate of the anodic metal dissolution process and cause deviations from simple rate equations assuming activation control. Passive films distinguish themselves from corrosion products in the sense that the former tend to be more tightly adherent, are of lower thickness, and provide a higher degree of protection from corrosive attack.

Available Test methods

Dust testing is still in the process of formalizing and standardizing itself. There is no standard dust chamber available to researchers and electronic product manufacturers. How to deposit dust on a surface or board is still challenge. Testing for the effects of dust could be done by seeding a surface with a measured quantity of dust or by exposing a board to an atmosphere containing a known concentration of dust. Parameters of interest like leakage current, surface insulation resistance, moisture sorption and de-sorption of dust contaminated board as a function of time and RH can be measured through the testing.

Researchers have developed different dust test methods and dust chambers to suit their research needs. Sandroff and Burnett reported a hygroscopic dust exposure test of PCBs [6]. Failures due to hygroscopic dust have been related to a surface insulation resistance lower than the $10^6 \Omega$ range. The effects of different salts on PCB insulation resistance were studied, with varied relative humidities. Some of these salts, such as ammonium hydrogen sulfate or ammonium sulfate, can be found in high concentrations in airborne hygroscopic dust. Sodium sulfide provides the highest sensitivity in resistance variation over the humidity range of 30~100%. Although it is not typically found in airborne hygroscopic dust, it offers a controllable technique to simulate the loss of SIR. Therefore, a 1/10M sodium sulfide solution was used to qualify the circuit boards. It was deposited by spin coating at 600 revolutions per minute (rpm). When small surfaces need to be coated, the salt may be deposited by spin coating. However, this technique might be difficult to use for large circuit boards. Spraying the salt solution can be used as an

alternative. Using ultrasonic atomization, a mist of fine droplets of controlled particulate size can be deposited onto a circuit board rastered in front of a spray-shaping chamber. The calibration of this technique can be done by measuring the mass of salt deposited on the surface. Figure 7 depicts an example geometry that can be used to deposit a saline mist onto a circuit board.

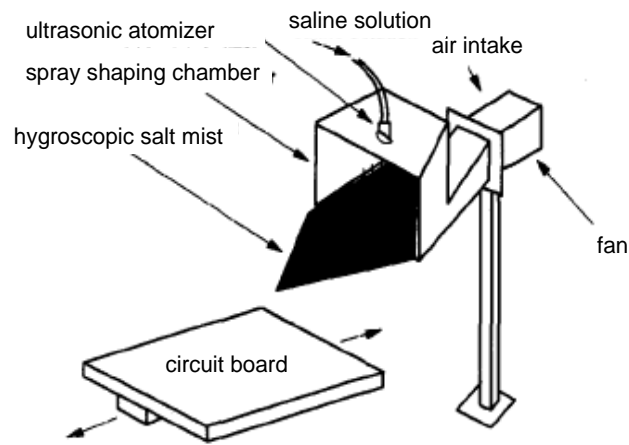


Figure 7: Sketch of the Hygroscopic Salt Mist Deposition System [6]

DeNure and Sproles reported the dust test results for multicontact circuit board connectors [11]. Hygroscopic salts were used to simulate some of the most severe conditions found in service environments. The salt composition was similar to that of natural dusts, except that nitrates were not used for safety reasons. Hard mineral particles were included to provide a substance with the mechanical strength to hold the contacts apart if the dust got into the interface. The mineral particles used were Arizona road dust. A dust chamber was designed for the test, as shown in Figure 8. The chamber is a clear plexiglass box measuring about 325 mm wide by 675 mm high and 200 mm deep. A fan

circulates the air along a path determined by baffles in the chamber. The dust is introduced into the system just above the fan, which directs it downward. The chamfered corners of the chamber direct the airflow clockwise. The test connectors are mounted on the other side of the baffle in the center of the chamber and the dust laden air impinges on them from the bottom. Some dust will stick to the bottom and some will settle out on the top. This represents a typical field use condition, where cooling fans direct air upward through the rack.

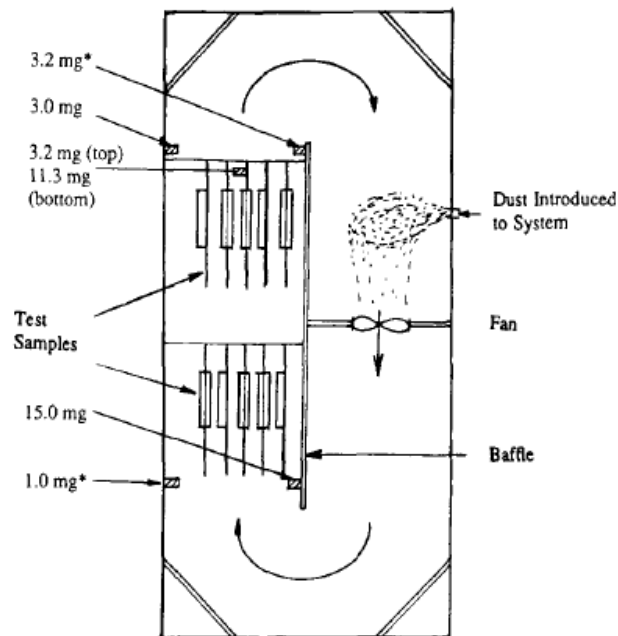


Figure 8: Schematic Representation of Dust Chamber used for Exposure of Test Connectors [11]

Lin and Zhang designed some dust tests to assess dust corrosion [10]. The natural dust samples were collected from three locations. Testing sheets for the experiments were made of phosphor bronze (alloy CA-511: 95.6Cu-4.2Sn-0.2P) coated with nickel and gold on top.

The difference between the work of [10] and this thesis is that the authors of [10] concerned with corrosion rather than loss of impedance and ECM considered in this thesis. They used water solution of dust to see if dust can cause corrosion on thin gold plated surface. The corrosion behavior of dust particles deposited test sheets was also evaluated using seven damp heat cycles. An observation was made that corrosion behavior of different dusts were different. And it was argued that corrosion increased rapidly with relative humidity, even though no definite value of critical relative humidity was observed. The observations in [10] agreed with the experimental results in this thesis.

The collected dust particles were dissolved in distilled water. The solution was dispersed by an ultrasonic cleaner, heated and naturally cooled down, and filtered by filter paper. The dust solution was dripped on the test sheet with a burette, after each previous droplet of solution evaporated. It takes about two hours for one droplet of solution to evaporate at room temperature and 35% relative humidity. The procedure continued until corrosion products were observed on the surface. Corrosion products formed on the test sheet at different rates, depending on the dust samples used. This experiment demonstrated that water-soluble salts are contained in dust. The solution forms electrolytes and corrodes metals.

The corrosion behavior of dust particles was also evaluated by spreading dust on test sheets, followed by seven damp heat cycles, as shown in Figure 9. Natural dust particles were spread on testing sheets (Au/Ni/Cu) at an average density of about $3200/\text{cm}^2$ by

means of a custom-made dust chamber. A simplified diagram of the dust chamber is shown in Figure 10. The dust particles were fed into the dust filler. Electrical fans connected in series blew the particles through an airflow pipe into a dust mixing room and finally into the dust deposition room for about three minutes. The fans were then stopped to allow dust particles to fall freely in the dust deposition room for about thirty minutes. Testing sheets were located horizontally to accept dust particles. The test confirmed that dust does cause corrosion under certain temperature and relative humidity levels.

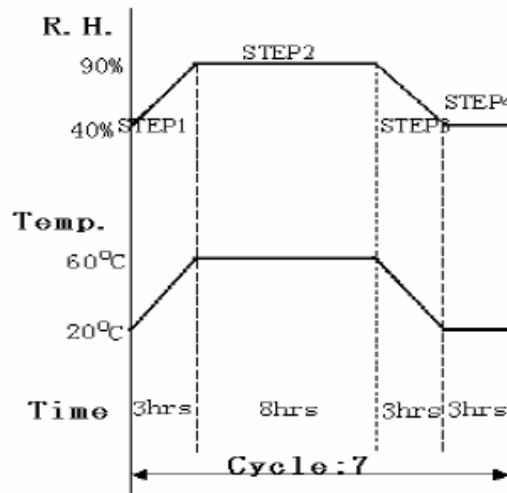


Figure 9: Change of Temperature and Relative Humidity in Damp Heat Experiments [10]

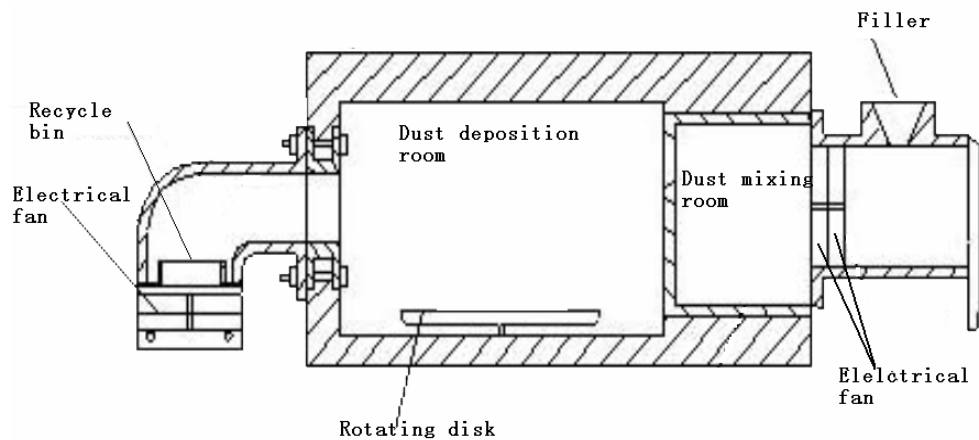


Figure 10: Simplified Diagram of Dust Chamber [10]

THB is a standard test method for assessing loss of SIR and electrochemical migration failures [12]. The normally-used testing conditions are 85°C and 85%RH. However, lower temperatures are considered more appropriate. Higher temperatures can actually reduce the propensity for corrosion or introduce a shift in failure mechanisms. In the meantime, elevated temperature may induce plating dissolution, resulting in changes in the migration mechanism. The relative humidity level is another critical condition in the testing. Since constant humidity is designed to assess reliability in non-condensing environments, there is often a tradeoff between maximizing humidity to induce potential failures while avoiding condensation. This is the primary driver towards setting 93%RH as the industry standard. Relative humidity is often only controllable to $\pm 2\%$, and 95% RH is often considered the maximum controllable relative humidity before condensation within the chamber becomes highly likely. Time-to-failure changes in orders of magnitude with relatively minor changes in relative humidity.

The primary differences in the industrial specifications tend to be in the duration of exposure, with surface insulation resistance tests extending approximately four to seven days, and electrochemical migration tests extending approximately five hundred hours (twenty-one days). For products with no conformal coating, a 40°C/93%RH exposure of three to five days is recommended. An additional two to three days are required for diffusion through the conformal coating.

Time-to-Failure Models

To correlate field environments to the test conditions and develop an appropriate test duration, validated TTF models need to be established to calculate the acceleration factor. TTF models relate accelerating variables, such as temperature, relative humidity, current, and voltage, to time acceleration. Models can be categorized as physical and empirical acceleration models.

The best practice for establishing a TTF model is through the use of a physics-of-failure (PoF) based approach. For well-understood failure mechanisms, a model may be based on physical/chemical theory that describes the failure-causing process over the range of the data and provides extrapolation to use conditions. If there is little understanding of the chemical or physical processes leading to failure, an empirical model may be the only alternative. An empirical model may provide an excellent fit to the available data, but can also provide nonsensical extrapolations.

Arrhenius-based empirical models for ECM

Hornung proposed a mathematical model for dendritic growth based on the Arrhenius empirical model [84], defined as

$$t_f = \frac{\alpha G}{V} \exp\left(\frac{\Delta H}{kT}\right)$$

where t_f is the time-to-failure, α is a proportionality constant, G is the spacing between electrodes, V is the applied voltage, ΔH is the activation energy (eV), k is Boltzman's constant (8.617E-5 eV/K), and T is the applied temperature (K). The dendritic growth of

silver through borosilicate glass under an applied electric field was measured in [84]. The activation energy for this process was determined to be 1.15 ± 0.15 eV and the growth rate was found to have an approximately linear dependence on the applied electric field.

Hornung's model is appropriate for estimating time-to-failure and acceleration factors, but it does not take into account relative humidity, and therefore it is not truly an electrochemical migration model. It also does not take into account ionic contamination, which is one of the primary drivers for ECM in circuit card assemblies. The proportionality constant must also be empirically determined through experimental testing.

The Eyring model expands upon the Arrhenius equation, adding terms for other stresses as necessary. This model is presented in the IPC Surface Insulation Resistance Handbook [85]:

$$t_f = AT^\alpha \exp\left\{\frac{\Delta H}{kT} + \left(B + \frac{C}{T}\right)S_1 + \left(D + \frac{E}{T}\right)S_2 + \Lambda\right\}$$

where A is a scaling constant; ΔH is the activation energy; k is Boltzmann's constant; T is temperature; α , B, C, D, E are constants determining stress interaction; and S_1, S_2, \dots , are stresses, such as humidity or voltage. The Eyring model corrects the multiple stress and synergism problems of the Arrhenius model. However, the complexity of the Eyring model increases dramatically with every added stress. In addition, the stress functions are undefined. The stress could be a natural log, exponential, or some other function.

The Peck model is based on the Eyring equation, with stress terms for relative humidity and voltage. Based on the results of temperature/humidity/bias (THB) testing, the model details the corrosion process as

$$t_f = A_0 RH^{-n} f(v) \exp\left\{\frac{\Delta H}{kT}\right\}$$

where A_0 is a material dependent constant, RH is relative humidity, n is an empirically determined constant (close to 3), and $f(v)$ is an undetermined function of voltage. There are limitations to the Peck model. Firstly, the voltage effect is provided in an undefined state. Secondly, Peck's model also fails to normalize voltage through the use of electric field strength, which is probably the more fundamental driver of migration-based phenomena. Thirdly, the Peck model does not directly take into consideration ionic contamination levels, though decreases in impurity levels followed by increases in activation energy suggest a correlation which has not yet been quantified. Finally, and most critically, the Peck model fails to address the potential for critical stress limitations, below which corrosion-based mechanisms will not initiate.

Physics-of-failure models for ECM

DiGiacomo [55] investigated the migration behavior of silver in encapsulated packages and developed the model

$$t_f = \frac{Q_c}{\beta J_{tip}}$$

where Q_c is the critical amount of metal ions that must migrate to achieve dendritic growth across a gap, β is the degree of oxidation or fraction of active surface changes from metal to metal, and J_{tip} is the current density at the dendrite tip. This model was

derived from the use of the Butler-Volmer equation, which relates electrode potential to current density. However, the inclusion of current density at the dendrite tip makes this model more interesting for academic investigation than for industrial application. Changing the point of focus of the model from current density at the dendrite tip to factors that influence current density would yield a model that evolves from the behavior of the physical mechanism and also incorporates measurable quantities. Current density is a function of conductance and electric field. Conductance is a function of contamination and relative humidity. Therefore, failure behavior can be described in terms of contamination, relative humidity, and electric field.

Empirical linear bi-logarithmic law for atmospheric corrosion

Atmospheric corrosion rates do not follow linear relationships with time and tend to be higher during the early stage. Pourbaix [86] described the so-called linear bi-logarithmic law for atmospheric corrosion to model atmospheric corrosion damage as a function of time. This law was shown to be applicable for different types of atmospheres (rural, marine, and industrial) and for a variety of alloys, such as carbon steels, weathering steels, galvanized steels, and aluminized steels. However, not all alloy and environmental combinations will follow this law. According to the linear bi-logarithmic law,

$$\log_{10}(p) = A + B \log_{10}(t)$$

where p is the corrosion penetration and t is the exposure time. The mean and instantaneous corrosion rate can be expressed by

$$\begin{aligned} \log_{10}(p/t) &= A + (B-1)\log_{10}(t) \\ \log_{10}(dp/dt) &= A + \log_{10}(B) + (B-1)\log_{10}(t) \end{aligned}$$

The atmospheric corrosion rate of a certain metal at a certain location can be described by the two model parameters, A and B. The initial corrosion rate (say, during the first year of exposure) is described by A, while B or (B-1) is a measure of the long-term decrease in the corrosion rate. When $B = 0.5$, the law of corrosion penetration increase is parabolic, with diffusion through the corrosion product layers as the rate-controlling step. At B values appreciably lower than 0.5, the corrosion products show protective, passivating characteristics. Higher B values, above 0.5, are indicative of non-protective corrosion products, such as loosely adherent, flaky rust layers.

An important aspect of the linear bi-logarithmic law is that it facilitates the prediction of corrosion damage in the long term, using shorter exposure tests. In Pourbaix's opinion [86], extrapolation may be valid for up to twenty to thirty years. In such long-term tests, changes in the environment may affect corrosion rates more significantly.

Chapter 4: Impedance Spectroscopy

In this research impedance spectroscopy (IS) method is used to characterize the impact of dust on PCB. IS measures the impedance of a component by scanning across a frequency range. IS method have been widely used in studying electrochemical process, such as those of battery cells, in which context the method is also called *electrochemical impedance spectroscopy* (EIS). To measure the impedance, one applies a small AC signal (often a small voltage perturbation in addition to the DC bias) to the component and investigates the electrical response of a system, including electronically conducting electrodes and material connecting them. EIS measures the relevant interfacial and bulk properties of the system. The resulting EIS data is usually used to construct an equivalent circuit model of the underlying physics. In our work we used the EIS data to investigate the dust effects on different conduction paths.

The electric properties of the component are characterized by the current versus potential curve (polarization curve).

$$V(t) = f(i(t), t)$$

Under the time invariant assumption, the equation can be simplified to

$$V = f(i)$$

During the measurement of impedance spectroscopy, a small AC potential signal is added to the component. The magnitude of the AC signal is often chosen to be much smaller than the working voltage of the component, *i.e.*, $|\tilde{V}| \ll |\bar{V}|$. The total current through the component can be decomposed into DC and AC parts.

$$i = \tilde{i} + \bar{i}$$

The total voltage across the component can be calculated as

$$V = \bar{V} + \tilde{V} = f(\bar{i} + \tilde{i}) \approx f(\bar{i}) + \frac{\partial f}{\partial i} \tilde{i}$$

The impedance of the component is measured as

$$Z(\omega) = \frac{dV}{di} = Z_r + jZ_i$$

In the following some conventional notations from the literature are listed. They are adopted in this chapter. Electric potentials are represented as V or Φ . Electric current are represented as i . The subscript 0 is used to represent the quantities at the equilibrium, e.g., Φ_0 represents the potential at equilibrium. A second subscript k is used to refer to a particular chemical reaction, i.e., $V_{0,k}$ represents the equilibrium potential for a reaction k . In the study of impedance spectroscopy, the tilde symbol is used for AC quantities, e.g., \tilde{V} , and over-line symbol for DC quantities, e.g., \bar{V} .

Models of Electrochemical Reactions

A widely used way to study electrochemical reaction is by *voltammetry*: an analysis method to characterize the relationship between the potential drop of the electrode and the current flowing through the electrode [19]. Electrochemical reactions that cause electric current are called *Faradaic* reactions. In a Faradaic reaction, charge is transferred across an electrified interface as a result. Non-faradaic reactions do not create charge transfer directly. Instead, charge can be associated with movement of electrolyte ions, reorientation of solvent dipoles, or adsorption/desorption, *etc.*, at the electrode-electrolyte interface.

The current density corresponding to a Faradaic reaction can be expressed as a function of an interfacial potential V , the surface concentration of bulk species $C_{i,0}$, as

$$i_f = f(V, c_{i,0}),$$

where the interfacial potential can be considered to be the difference between the potential of the electrode Φ_m and the potential in the electrolyte adjacent to the electrode Φ_0 , measured with respect to the same reference electrode as used to measure the cell potential. This equation represents a general result that can be applied to any electrochemical reaction. This general expression guides development of impedance models from different reaction sequences, which has a major influence on the frequency dependence of the interfacial Faradaic impedance.

Electric current flows in an electrochemical system are controlled by several factors: the rate of chemical reaction at the electrode (electrode kinetics), the net movement of the charge carrying ions flowing in the liquid (mass transfer) and the conductivity of the electrode, liquid, and the connections of the system, which is usually simplified as resistances. Figure 11 shows a polarization curve of an electrochemical reaction from [5]. The potential loss can be decomposed into three contributing factors: *ohmic* loss, *kinetic* controlled loss (also called charge transfer controlled loss) and *mass transfer* controlled loss. The total voltage loss is calculated as the sum of the three components.

$$V_{total} = V_{kinetic} + V_{ohm} + V_{mass}$$

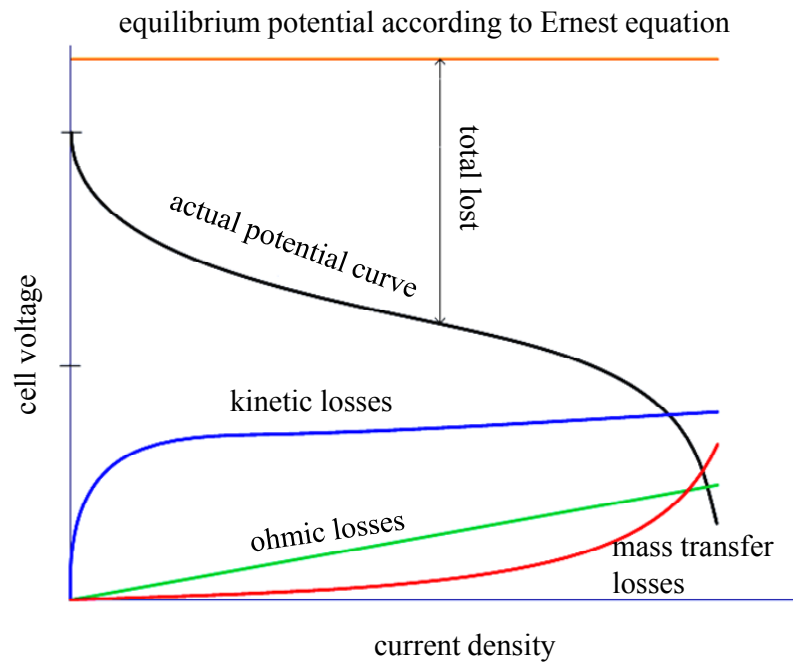
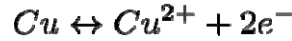


Figure 11 A typical polarization curve of fuel cell and decomposition of the potential losses [5]

When the current flow is very low, the system is in the kinetic controlled region, which is mostly governed by the charge transfer of the chemical reaction. The Butler-Volmer model and Tafel model are often used to describe the voltage-current relation. As the electric current increases, the mass transfer process becomes the limiting factor of the electric current. The mass transfer controlled process is governed by the rate at which the reacting species are carried to the electrode surface, which is then limited by the concentration of the reacting species in the bulk liquid. The voltage and current relationship of a mass transfer controlled system can be derived using Fick's law and the convection-diffusion model of the liquid.

Kinetic Models

Kinetic models are used to study the rate of the electrochemical reactions. All kinetic models are functional approximations of the polarization curve. Tafel equation is a widely used model. Tafel equation considers a Faradaic reaction, anodic or cathodic, e.g.,



When using the Tafel equation, one makes the assumption that the reverse reaction is negligible; thereby simplify the model of the reaction to be irreversible. Tafel equation has the form

$$i = nFk \exp\left(\pm \alpha F \frac{\eta_s}{RT}\right),$$

where the plus sign under the exponent refers to an anodic reaction, and a minus sign to a cathodic reaction;

- $\eta_s = V - V_{0,k}$ is the surface over potential;
- n is the number of electrons involved in the electrode reaction;
- k is the rate constant for the electrode reaction;
- α is called the *charge transfer coefficient*, a constant between 0 and 1;
- F is the Faraday constant;
- R is universal gas constant.

The Tafel equation is sometimes also written in a compact form.

$$i = i_0 \exp\left(\pm \frac{\eta_s}{\beta}\right)$$

where $\beta = RT/\alpha F$. Take the logarithm of both side of the equation, we have

$$V = V_{0,k} + \beta(\log(i) - \log(i_0)),$$

which is a linear equation. Therefore the parameter β is also called the *Tafel slope*.

When the reverse reaction cannot be neglected, the Butler-Volmer equation can be used to model the kinetics of the reaction. In the Butler-Volmer equation, a reaction is considered for both forward (anodic) part and backward (cathodic) part [16]. The equation has the following form.

$$i = i_a + i_c = i_0 \left(\exp\left(\frac{(1-\alpha)n_e F}{RT} \eta_s\right) - \exp\left(\frac{\alpha n_e F}{RT} \eta_s\right) \right)$$

The Butler-Volmer equation has the following properties. When $\eta_s = 0$, $i_a = -i_c = i_0$ and $i = i_a + i_c = 0$. The potential at equilibrium $V_{0,k}$ is called the *equilibrium potential*. α is called the symmetry factor, measures promotion of cathodic reaction. It satisfies $0 \leq \alpha \leq 1$. And α is usually close to 0.5.

In either the Tafel or the Butler-Volmer model, the exchange current density is proportional to $|s_i|c_i(0)$. Specifically, the exchange current density can be described as

$$i_0 = k_c \cdot n \cdot |s_i| \cdot F \cdot c_i(0)$$

where F is the Faraday constant, $c_i(0)$ is the concentration of the species at the interface, s_i is the stoichiometric coefficient, and k_c is the rate constant with respect to concentration.

Mass transfer controlled models

In mass transfer controlled region, the current is controlled by the convection and diffusion of the charge carrying species in the solution. The convection-diffusion equations are obtained by solving the material balance equation.

The convection of electrochemical processes is typically modeled in cylindrical coordinates, which consists of three coordinates: the axial position y , the radial distance r and the angle θ . Figure 17 illustrates the mapping between the Cartesian coordinates and the cylindrical coordinates.

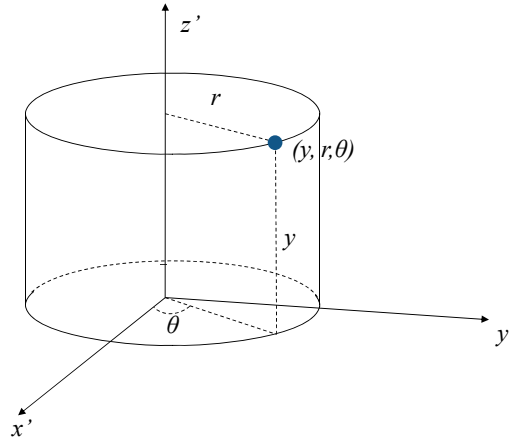


Figure 12: Cylindrical coordinate system

It is commonly assumed that the boundary condition and flow are independent of the radial condition, where the diffusion process is only considered along the axial direction y . The convection-diffusion model is described as

$$\frac{\partial c_i}{\partial t} + v_y \frac{\partial c_i}{\partial y} - D_i \frac{\partial^2 c_i}{\partial y^2} = 0,$$

where v_y is the convection velocity along y axis.

The governing equation of a diffusion process is Fick's second law.

$$J = D \frac{\partial c}{\partial y},$$

where J is the diffusive flux ($\text{mol}/\text{m}^2\text{s}$), which measures the amount of substance flowing through a unit area; and D is the diffusion coefficient or diffusibility of the solution.

In a simplified model, the diffusion layer is assumed to be a constant gradient layer, where concentration of the species distributes linearly in the diffusion layer. The current limit due to mass transfer at cathode can be computed derived from

$$i = -nFD_i \frac{c_i(\infty) - c_i(0)}{\delta_i} \quad (2)$$

where

- D_i is the diffusion coefficient

$c_i(0)$ and $c_i(\infty)$ are the concentration of the active species at the surface and in the bulk solution, respectively.

In a mass transfer controlled process, define the *mass transfer limited current density* as

$$i_{lim} \equiv -nFD_i \frac{c_i(\infty)}{\delta_i} \quad (3)$$

The above definition is not based on physically measurable current or its components, rather it is an artificial quantity that roughly correspond to the measurable concentration of the bulk solution. And substitute (3) into (2), we have

$$i = -nFD_i \frac{c_i(\infty) - c_i(0)}{\delta_i} \quad (4)$$

Because the mass transfer control zone is far from the equilibrium point, Tafel equation is used to model the kinetics. Some further manipulation gives the relationship between the overall current and the mass transfer limited current density.

$$\begin{aligned}
i &= -k_c \delta_i \frac{i - i_{lim}}{D_i} \exp(-b_c \eta_s) \\
i &= -\frac{k_c \delta_i}{D_i} \exp(-b_c \eta_s) \cdot i + \frac{k_c \delta_i}{D_i} \exp(-b_c \eta_s) \cdot i_{lim} \\
\left(1 + \frac{k_c \delta_i}{D_i} \exp(-b_c \eta_s)\right) \cdot i &= \frac{k_c \delta_i}{D_i} \exp(-b_c \eta_s) \cdot i_{lim}
\end{aligned} \tag{5}$$

The equation establishes the relationship between the mass transfer limited current density and the limit on the total current density. Note that the mass transfer limited current density is proportional related to the concentration of the bulk solution. The above equation states that the overall current in a mass transfer controlled process is proportional limited by the concentration.

Define the kinetic current density based on the bulk concentration as

$$i_k \equiv -K_c n F c_i(\infty) \exp(-b_c \eta_s) \tag{6}$$

Divide (6) by (3), we have

$$\frac{i_k}{i_{lim}} = \frac{K_c \delta_i}{D_i} \exp(-b_c \eta_s) \tag{7}$$

Substitute the term on both sides of (5) using (7), we have

$$\left(1 + \frac{i_k}{i_{lim}}\right) i = i_k \tag{8}$$

Divide both side of the equation by $(i \cdot i_k)$, we have

$$\frac{1}{i_k} + \frac{1}{i_{lim}} = \frac{1}{i} \tag{9}$$

Equation (9) gives the relationship between the measurable total current density and the two quantities defined as the kinetic current density and mass transfer limited current density.

Equivalent Circuit Modeling

The impedance of the electrochemical processes is usually decomposed into two parts: the bulk resistance and the interfacial impedance. The interfacial impedance is frequently modeled as a combination of Warburg impedance, charge transfer resistance, and double layer capacitance.

Electrical double layer capacitance

When electrodes are placed in electrolyte, a capacitance may arise due to charge redistribution at liquid/solid interfaces. The redistributed particles with charge form a structure called *electrical double layer*. The double layer structure has two parallel layers of charges on the surface of an electrode. The inner layer consists of ions adsorbed directly at the surface of the electrode. The electrical surface charge is built up by the non-electric affinity of charge. The surface charge can be due to a host of chemical reactions or because of externally applied voltage source. A number of electrically charged ions are attracted to the surface by the Coulomb force and form an outer layer. The outer layer creates a countercharge of the layer with the same magnitude, and thus electrically screens the inner layer. This outer layer is loosely associated with electrode surface, because it is made of free ions that move in the electrolyte under the influence of electric attraction and thermal motion rather than being firmly anchored. A schematic representation of an electrical double layer is shown in Figure 13.

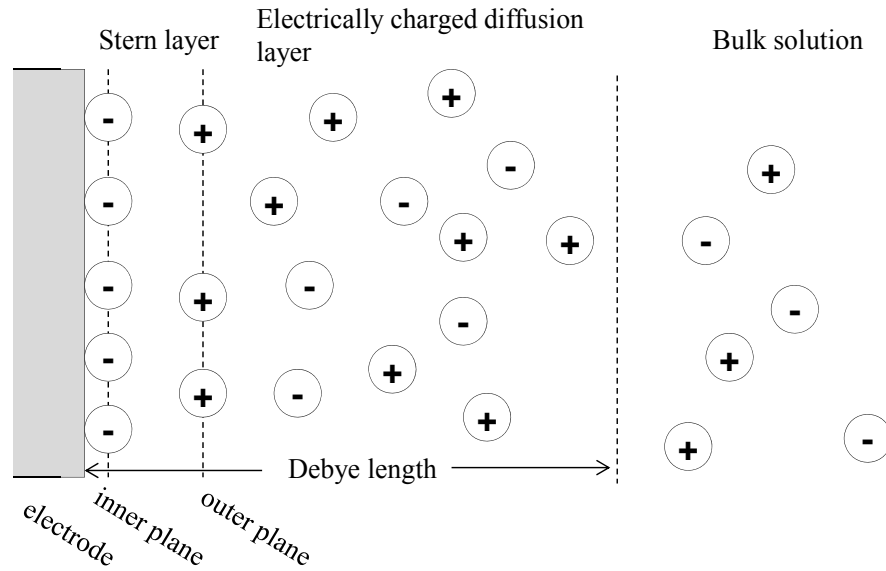


Figure 13: Double layer structure (adapted from [16])

The Gouy-Chapman-Stern model is most commonly used to describe the double layer. In this combined model, some of the counter ions specifically attract to the surface charge layer and build up an inner sub-layer, called Stern layer or Helmholtz layer. The outer part of the second layer is called the diffuse layer or Gouy-Chapman layer.

For flat surfaces, the double layer thickness is characterized by the so-called Debye length (κ^{-1}) defined by:

$$\kappa^2 = F^2 \sum_i \frac{c_i z_i}{\epsilon_0 \epsilon_m RT},$$

where the valences (z) have sign included, for a symmetrical electrolyte $z_+ = -z_- = z$.

One of the key characteristics of double layer is its differential capacitance (C_{dl}), which is expressed by the equation:

$$C_{dl} = \frac{d\sigma}{d\Phi} = \epsilon_0 \epsilon_m \kappa \cosh \frac{F\phi_d}{2RT}$$

where

- σ is the surface charge, the amount electric charge carried by the first layer.
- Φ is the electric surface potential, the potential difference between the bulk of electrolyte and the electrode surface, and
- Φ_d is the *Stern potential*, which is defined as the electric potential on the external boundary of the Stern layer versus the bulk electrolyte.

Warburg impedance

Warburg impedance was invented to describe the impedance caused by diffusion controlled chemical reactions. Assuming a stagnant diffusion process where natural convection is ignored. The Fick's law is simplified as

$$\frac{\partial c_i}{\partial t} - D_i \frac{\partial^2 c_i}{\partial y^2} = 0$$

Consider the experiment in EIS, where the concentration can be decomposed into DC and AC components.

$$c_i = c_i + \text{Re} \{ \tilde{c}_i e^{j\omega t} \}$$

Under the assumption of EIS, the diffusion rate is much slower than the measuring frequency such that the concentration is constant at the time of measurement. The dynamics of DC component are ignored; Fick's law can be rewritten in terms of the AC components.

$$j\omega \tilde{c}_i - D_i \frac{d^2 \tilde{c}_i}{dy^2} = 0$$

Recall the dimensionless quantity $\theta_i(y) = c_i(y)/c_i(0)$. In terms of the dimensionless quantity θ_i , the Fick's law can be rewritten as

$$j\omega\theta_i - D_i \frac{\partial^2 \theta_i}{\partial y^2} = 0$$

The solution of the above equation is $\theta_i(y) = e^{-y\sqrt{j\omega/D_i}}$.

To calculate the equivalent impedance, compute the inverse derivative of θ_i with respect to y at 0.

$$\frac{1}{\theta_i'(0)} = -\frac{1}{\sqrt{j\omega/D_i}}$$

Following the equations of the Randles circuit, we know

$$Z_D(\omega)/Z_D(0) = -\frac{\tilde{c}_i(0)}{d\tilde{c}/dy|_{y=0}} = \frac{1}{\sqrt{j\omega/D_i}}$$

The impedance Z_D is called the *Warburg impedance*, which is frequently referred to as W .

Randles Circuit Model

The corrosion of metal in an aqueous medium is normally influenced by the rate of transport of reactants to the electrode surface. The impedance response for such a system requires the considerations of both kinetic and mass transfer process. Randles circuit is a widely used equivalent electrical circuit derived from such a system. It consists of an active electrolyte resistance R_S in series with the parallel combination of the double-layer capacitance C_{dl} and an impedance of a faradaic reaction. See Figure 14 for a diagram of the Randles circuit.

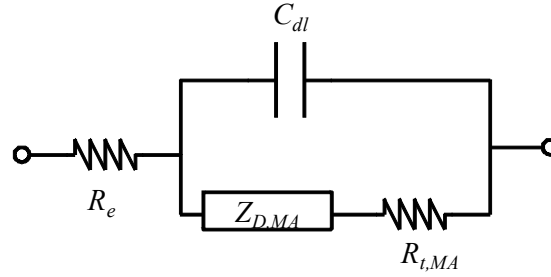
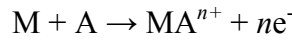


Figure 14: Randles circuit

The reaction mechanism is given as



The steady state current density can be calculated by the kinetic model of Tafel equation, which is a function of both concentration of species A at the electrode surface and the potential difference between the electrode and the solution adjacent to the electrode.

$$\bar{i}_{MA} = K_{MA} \bar{c}_{A,0} \exp(b_{MA} \bar{V})$$

The oscillating component of the current density is given by

$$\tilde{i}_{MA} = K_{MA} b_{MA} \bar{c}_{A,0} \exp(b_{MA} \bar{V}) \tilde{V} + K_{MA} \exp(b_{MA} \bar{V}) \tilde{c}_{A,0}$$

where $\tilde{c}_{A,0}$ represents the oscillating component of the concentration of species A evaluated at the electrode surface.

Due to the concurrence of the mass transfer process, the steady-state current density can be expressed according to the Fick's law.

$$\bar{i}_{MA} = -n_{MA} F D_A \left. \frac{d\bar{c}_A}{dy} \right|_{y=0}$$

which can be expressed in terms of the oscillating contributions as

$$\tilde{i}_{MA} = -n_{MA}FD_A \left. \frac{d\tilde{c}_A}{dy} \right|_{y=0}$$

The surface concentration $\tilde{C}_{A,0}$ can be eliminated from the two oscillating current equations to obtain

$$\tilde{i}_{MA} = \frac{\tilde{V}}{R_{t,MA} + Z_{D,MA}}$$

Where

$$Z_{D,MA} = \frac{\delta_A}{n_{MA}FD_A\tilde{c}_{A,0}} \frac{1}{b_{MA}} \left(-\frac{1}{\tilde{\theta}'_A(0)} \right)$$

is the convective-diffusion impedance, and the charge-transfer resistance for reaction is defined in terms of kinetic parameters to be

$$R_{t,MA} = (K_{MA}b_{MA}\tilde{c}_{A,0}\exp(b_{MA}\bar{V}))^{-1}$$

Based on the impedance response associated with Faradaic reactions, the system impedance response is obtained in terms of capacitance and electrolyte resistance

$$Z_{MA}(\omega) = R_c + \frac{R_{t,MA} + Z_{D,MA}(\omega)}{1 + j\omega (R_{t,MA} + Z_{D,MA}(\omega)) C_{dl}}$$

The electrical circuit in Figure 14 yields the impedance response equivalent to the above equation for a single Faradaic reaction coupled with a mass transfer.

Chapter 5: Methodology

Different Natural Dusts and Standard Test Dust

Four different dust samples were used in this study including three natural dust and one ISO test dust. Three dust samples were natural dust collected from fields. Dust 1 was collected from an outdoor multiple-level garage in the urban area of Boston, Massachusetts. The samples were collected on the second and third floors, see Figure 15. Dust 2 was collected from a computer room in an office building in Boston, Massachusetts. The office space is equipped with an air conditioning system, see Figure 16. Dust 3 was collected from an outdoor multiple-level garage located in the city of Tianjin, located in the east coast of China. Dust 4 is an ISO standard test dust (ISO 12103 -1, A2 Fine Test Dust) purchased from Powder Technology, Inc.

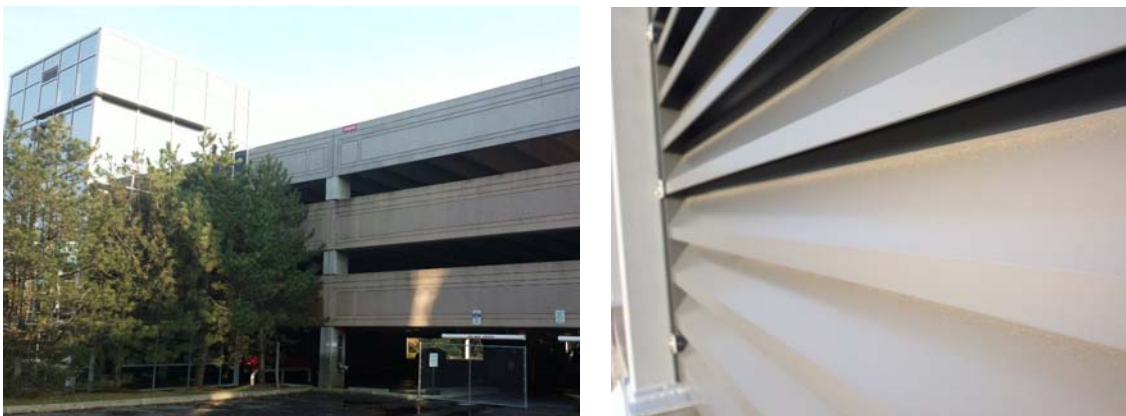


Figure 15: Site of Dust 1

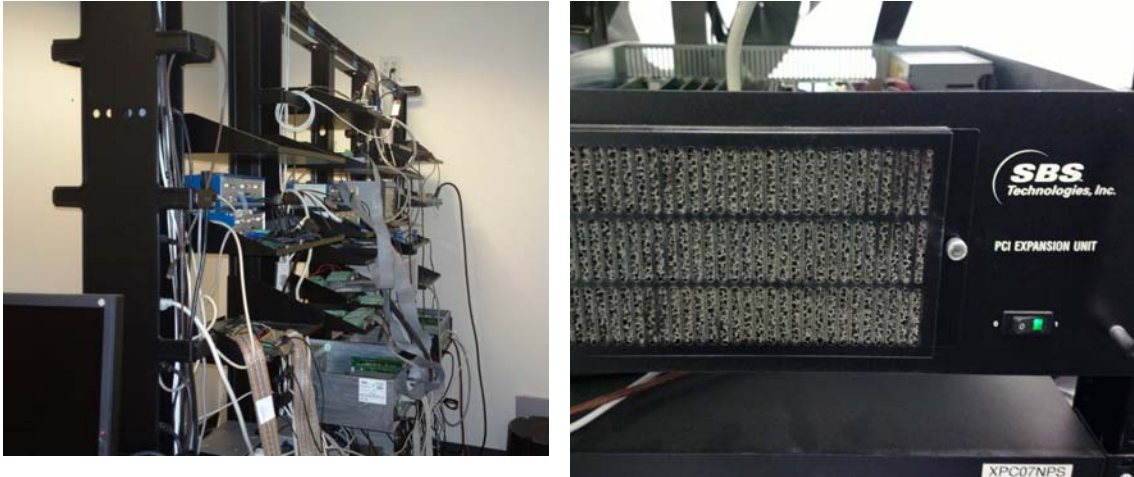


Figure 16: Site of Dust 2

Design of Test Coupon

The impedance of a contaminated surface area is dependent on the shape, geometry and material of the test vehicle. Since there are few experimental data on measuring the surface impedance in presence of dust, a preliminary test was conducted to determine the appropriate amount of dust deposition and trace spacing for the test coupons. The parameters were chosen so that the range of impedance for the tested samples is within the capacity of the measuring equipment. Once the parameters are experimentally determined, they were used to in the final test vehicle and experiments for larger sample size.

The test coupons for the preliminary test were designed with adjustable spacing to allow manual calibration. The pairs of copper electrode strips were placed on a FR-4 board, where they could be moved toward or apart from each other. Once the spacing is set, the electrodes were fastened with plastic fixtures and mounting hardware. Two parallel copper electrodes with a length of 200 mm were selected in this group of study. There

are 6 pairs of parallel electrodes on each board. Figure 17 shows one of the test boards used in the preliminary test. The spacing was set as 0.25 mm. A thickness gauge was used to set the spacing and control parallelism of the two electrodes. We used an optical microscope to verify the spacing setting. The board was FR-4 board with a thickness of 0.062" (1.57 mm). The copper electrodes were made by copper foil with a thickness of 0.007" (0.18 mm). Guard traces were added on the test coupons to reduce the noise of high impedance line. The appropriate spacing between copper traces and appropriate amount of dust deposition were determined in the preliminary tests.

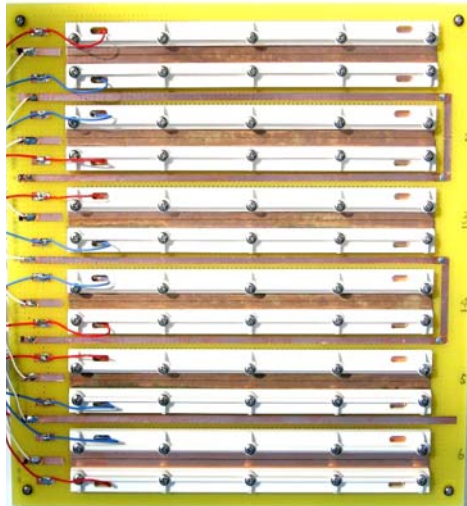


Figure 17: Test coupon with 6 pairs of parallel electrodes used in preliminary tests

The final test coupons were designed using comb structures with the determined trace spacing. Comb structure test coupons are manufactured with bare copper electrodes, see Figure 18. The size of the boards was designed to be 76 mm by 82 mm. The spacing between the interdigitated electrodes was designed to be 0.305 mm. The substrate was FR-4 laminate with a thickness of 1.600 mm. The copper trace of the comb structure had a thickness of 0.035 mm. Guard traces were added on the test boards to reduce the noise

Estimation of Dust Deposition Density

In the GR-63-CORE [54], it provides the average yearly levels of indoor and outdoor contaminants based on measurements with a dichotomous sampler. The sampler size-fractionates the collected particles into two modes: fine particles (less than or equal to 2.5 μm) and coarse particles (from 2.5 to 15.0 μm). Particles are collected on Teflon membrane filters and weighed to determine TSP. Collection times range from 1 to 7 days. TSP – Dichot 15 is the total suspended particulates determined using a dichotomous sampler with a 15- μm inlet.

Table 7: Average Yearly Levels of Indoor/Outdoor Contaminants

Contaminant	Indoor	Outdoor
Airborne Particles (TSP – Dichot 15)	20 $\mu\text{g}/\text{m}^3$	90 $\mu\text{g}/\text{m}^3$
Coarse Particles	<10 $\mu\text{g}/\text{m}^3$	50 $\mu\text{g}/\text{m}^3$
Fine Particles	15 $\mu\text{g}/\text{m}^3$	50 $\mu\text{g}/\text{m}^3$

Dust particle surface deposition density can be calculated if their concentrations are known and a deposition velocity appropriate for the airflow conditions can be estimated. While the available data on deposition velocities are not entirely consistent and are sparse for some conditions, a guideline suggested in [6] is listed in Table 8. Deposition velocity is strongly dependent on airflow velocity and particle size. The deposition velocities for the mineral/biological particles are dominated by gravitation and thus increase with size. Deposition velocities for the smallest particles (0.01~0.1 μm) are dominated by their diffusivity, while the mature pollutants (0.1~1 μm) are affected by both factors.

Table 8: Deposition Velocities for Airborne Particles (cm/s)

Airflow velocity	Particle Size 0.01~0.1 um	Particle Size 0.1~1.0 um	Particle Size 1~15 um
Outdoor (250~1000 cm/s)	0.6~6	0.6	0.6
Office building (2~4 cm/s)	0.009~0.6	0.006	0.6

The deposition velocity for particles size 0.1~1 um and 1~15 um are used for fine particle and coarse particles, respectively. The dust mass surface deposition density of outdoor coarse particles is calculated as follows:

$$50 \mu\text{g}/\text{m}^3 \times 0.6 \text{ cm}/\text{s} \times 1 \text{ yr} = \frac{50 \mu\text{g} \times (0.6 \times 0.394) \text{ in} \times (365 \times 24 \times 60^2) \text{ s}}{61023 \text{ in}^3 \times \text{s}} = 6108 \mu\text{g}/\text{in}^2$$

The surface deposition density for both indoor and outdoor dust contaminants are summarized in Table 9 during a one-year period.

Table 9: Surface Deposition Density of Dust per Year

Contaminant	Indoor	Outdoor
Airborne Particles	1.2 mg /in ²	12.2 mg /in ²
Coarse Particles	1.2 mg /in ²	6.1 mg /in ²
Fine Particles	1.8E-3 mg /in ²	6.1 mg /in ²

For this estimation, it indicates that a dust position density of 1 mg/in² is approximately equivalent to one-year indoor or one-month outdoor dust accumulation in the field.

Dust Deposition

Volatile solvent was used to transfer the dust particles onto the test coupons. Small quantities of dust particles (around 500 mg) were suspended in a 99.9% isopropyl alcohol (IPA) solution and then distributed onto the test coupons using a transfer pipette. IPA is a

cleaning solvent commonly used in surface mount manufacturing production. IPA volatilizes quickly, thereby leaving the dust deposits on the coupon surface. The dust deposition density was estimated by the weight change before and after dust deposition. Four different deposition density of dust was used: $1\pm 0.1 \text{ mg/in}^2$, $2\pm 0.2 \text{ mg/in}^2$, $3\pm 0.3 \text{ mg/in}^2$ and $4\pm 0.4 \text{ mg/in}^2$, denoted as 1X, 2X, 3X and 4X, respectively. The test coupons were inspected under an optical microscope and a scanning electronic microscope (SEM) at different magnifications to verify the uniformity of the dust distribution. The microscopic images showed that the dust distribution was even in general, although there were clusters in some areas. Optical images of test coupons with different levels of dust deposition are shown in Figure 3. Impedance measurements of the test coupons with the same deposition density further confirmed the consistency of the deposition. For test coupons deposited with the same deposition density, the measured impedance is less than 0.1 decade away from each other at each frequency measurement point.

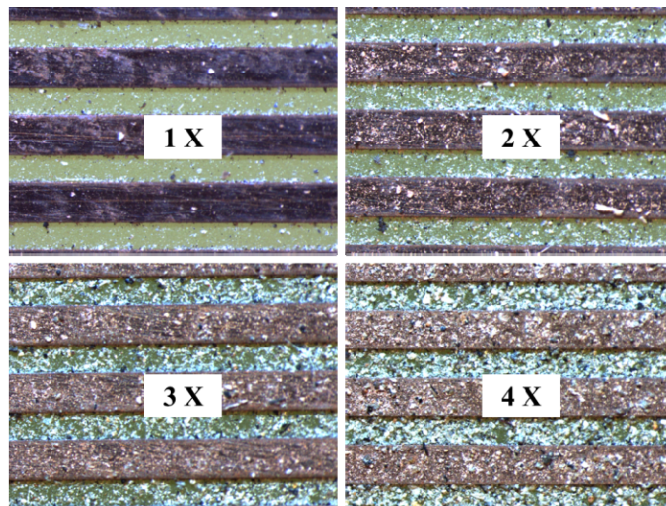


Figure 20: Test coupons with different dust deposition densities

Experimental Approach

This research investigated the interactions between dust deposits and environmental factors including RH and temperature. The RH and temperature effects were examined separately. The first group of tests examined the RH effect, which was conducted at different RHs while keeping a constant temperature. The dust deposition densities of test coupons varied from 1X to 4X. During the course of testing, a constant temperature of 40°C was maintained, while the RH was controlled to cover the range from 50% to 95%. The ramp rate between the plateaus (soaking periods) was less than 1% per minute. No electrical field was applied between the impedance measurements. The RH profile is shown in Figure 21. The measurements were taken 30 minutes after the set-point of RH has reached to allow the chemical process to reach a stable point. The measurement times are illustrated as arrows in Figure 21.

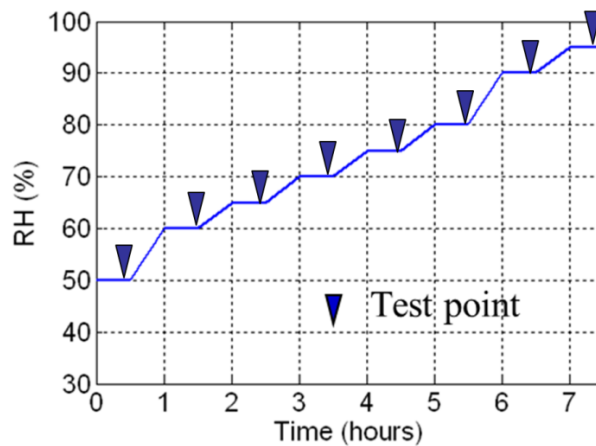


Figure 21: Relative humidity step-up profile.

A second group of tests was conducted at different temperatures. Four different levels of dust deposition densities were used. During the testing, the relative humidity was kept

constant at 90% and the temperature was varied from 20°C to 60°C. The ramp rate between the plateaus was less than 2°C per minute. No electrical field was applied. The measurements were taken 30 minutes after the set-point of RH has reached to allow the chemical process to reach a stable point. The temperature profile is shown in Figure 22.

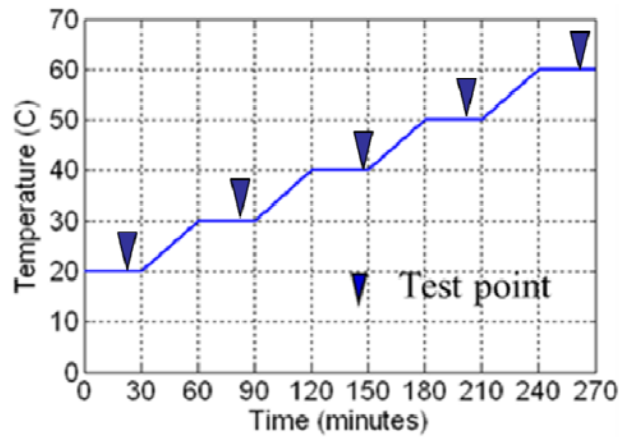


Figure 22: Temperature step-up profile

To evaluate the differences in impedance due to dust deposition density, four different levels of dust deposition densities were chosen. During the comparison tests of different dusts, only one deposition density was used. Clean boards without dust deposition were used as control samples for each group of tests. The sample size for each condition was 3 boards.

To evaluate the ECM failures, tests were performed at a constant temperature at 50°C and 90% RH with a 10 VDC electrical field. This is referred to as a temperature-relative humidity-bias (THB) [18]. It produces voltage-assisted corrosion related failure mechanisms and quantifies the time-to-failure (TTF) of different dust-deposited test boards. There is no standard testing to evaluate the impact of dust on the loss of

impedance caused by ECM and corrosion. The testing conditions are frequently chosen without considering the physics of failure. The ECM process occurs by a sequence of steps consisting of path formation, electrodisolution, ion transport, electrodeposition, and dendrite growth [62]. The duration of ECM evaluation is normally between 500 and 1000 hours, due to the long period of the path formation step [63] [64], which makes testing impractical for industrial adoption. In this research, the following approach is adopted. First, the critical RH range and temperature conditions are identified. Then, an appropriate combination of these environmental parameters is selected for the dust in ECM evaluation. Thus, the path formation step is shortened, and the ECM or corrosion failures are successfully reproduced in five days.

The test matrix and sample size are summarized in Table 10.

Table 10: Test matrix.

	Dust 1										Comparison Tests														
Temp	40 °C					20~60 °C					40 °C					20~60 °C					50 °C				
RH	50~95%					90%					50~95%					80%					90%				
Bias	No					10 VDC																			
Dust	-	D1				-	D1				-	D1	D2	D3	D4	-	D1	D2	D3	D4	-	D1	D2	D3	D4
Dust Deposition Density *	CTL	1X	2X	3X	4X	CTL	1X	2X	3X	4X	CTL	2X	2X	2X	2X	CTL	2X	2X	2X	2X	CTL	2X	2X	2X	2X
Sample Size	3	3	3	3	3	3	3	3	3	3	3	3	3	3	3	3	3	3	3	3	3	4	4	4	4
Test Duration	15 hrs					10 hrs					15 hrs					10 hrs					144 hrs				
Test Measurement	Impedance Measurement at 25 mV					Impedance Measurement at 25 mV					Impedance Measurement at 25 mV					Impedance Measurement at 25 mV					Resistance Monitoring at 10 VDC				

Test Measurement

In this research, AC measurements were used when the reliability tests were performed without electrical fields in the temperature effect and RH effect tests. The impedance data of test boards were collected during the testing at each temperature and RH steps. AC impedance spectroscopy was measured by scanning a frequency range from 20 Hz to 2 MHz using an Agilent E4980A Precision LCR Meter. An AC voltage at the level of 25 mV was applied for about 2 minutes to take the measurement.

Continuous resistance monitoring using DC voltage was employed in the THB test. A current limiting resistor of 500 ohms was connected in series with the test board. A data logger was used to provide continuous monitoring of the voltage across the resistor. The power supply was set at 10 VDC in the constant voltage mode. Figure 23 shows the schematic diagram of the measurement circuit. The resistance of the dust contaminated area across the comb structure was calculated through the continuously measured voltage value of the fixed resistor and the voltage of the power supply.

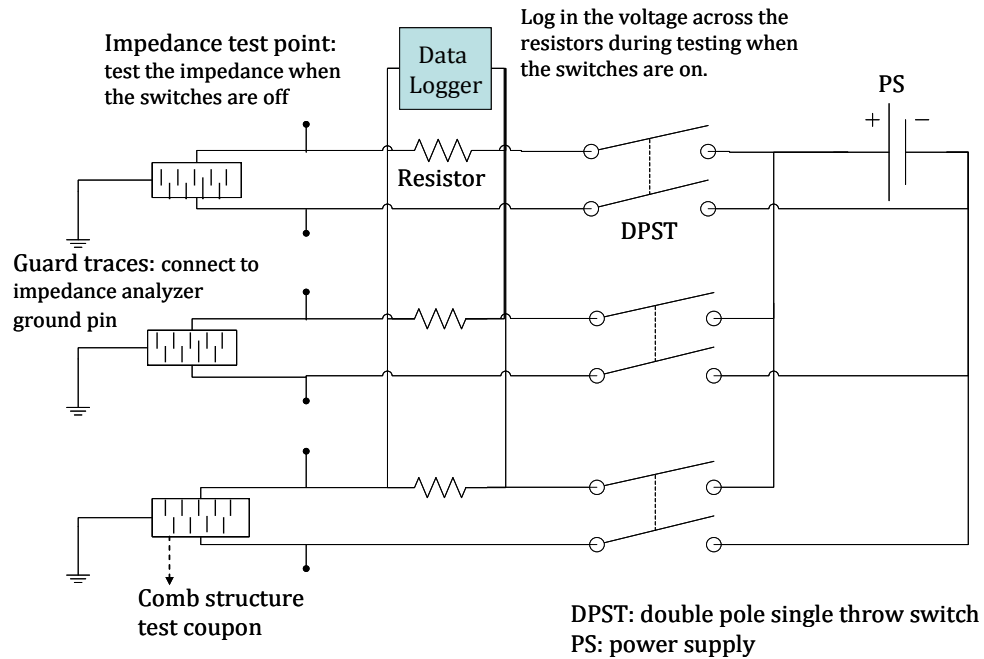


Figure 23: Resistance monitoring in THB test

Resistance monitoring was performed by applying a DC voltage and measuring the electric current. The resistance value is then calculated based on Ohm's law. This method has been used in industry to quantify the contamination levels of printed circuit boards [85]. Generally, the applied electrical voltage is in the range of 10V -100V [62], [63]. However, the results of DC resistance measurement may not accurately reflect the electric properties of the system because the migration of ions does not strictly follow Ohm's law [12]. Moreover, DC measurement requires a constant voltage applied on the test sample for an extended period. The external electrical field at 10-100V can cause polarization on the electrodes, and result in an increase in the measured resistance [72]. Additionally, DC resistance measurement may not be applicable for real conditions. For example, if an analysis of a system during the start-up process is desired, where there is

no externally applied electrical field in the system, the DC measurement cannot be applied.

Electrochemical impedance spectroscopy (EIS), which is widely used in electrochemistry, was adopted in this study. This approach includes the small signal measurement of the electrical response of a system of interest and subsequent analysis of the response to yield detailed system description, such as an equivalent circuit model, about the physiochemical properties of the system [23]. Compared to DC measurement, EIS data contain more information and can be used to calculate resistance, inductance, capacitance, and other nonlinear components such as Warburg impedance. In EIS, a very small voltage (at the millivolts level) is applied to avoid polarization at the electrodes. Thus, EIS measurement is useful where DC measurement is either inaccurate or inapplicable.

Chapter 6: Experimental Results

Characterization of Different Dusts

Characterization of the dust samples was conducted through a series of analyses: the anionic and cationic contents were quantified through ion chromatograph (IC) analysis; compositional/morphological analysis of different dust samples was conducted through scanning electron microscope-energy dispersive spectroscopy (SEM-EDS) analysis; aqueous solutions produced from dust samples were used to measure the pH and conductivity; a moisture soaking study was conducted to measure the moisture sorption abilities of different dust samples.

Ion Chromatography Analysis

A known mass of dust sample of 1 gram was added to 100 mg of DI water at an ambient temperature of 25°C for 10 minutes. Any un-dissolved dust particles were filtered out to produce an extracted dust sample solution, which was analyzed for anionic and cationic content using an IC. Results were calculated using following Equation:

$$\text{Analyte} \left(\frac{\mu\text{g}}{\text{g}} \right) = \frac{[\text{Concentration in Extract} \left(\frac{\mu\text{g}}{\text{g}} \right)] \cdot [\text{Weight of Extraction (g)}]}{[\text{Weight of Sample (g)}]}$$

The ion analysis results are shown in Table 11. If the ion concentration was less than 60 ppm, it could not be detected by the equipment and is labeled as “None Detected (ND)” in the table. Dust 3 had the highest total ion concentration, while Dust 4 had the lowest.

Dust 3 had high concentrations of sulfate, nitrate, and calcium ions that exceeded 10,000 ppm.

Table 11: Ion analysis results.

Ion	Dust 1 (ppm)	Dust 2 (ppm)	Dust 3 (ppm)	Dust 4 (ppm)
Fluoride (F ⁻)	ND	219	316	ND
Chloride (Cl ⁻)	2970	4820	4910	446
Nitrite (NO ₂ ⁻)	ND	ND	ND	ND
Bromide (Br ⁻)	ND	ND	ND	ND
Nitrate (NO ₃ ⁻)	6220	10200	19900	130
Sulfate (SO ₄ ²⁻)	3450	12600	52100	77.9
Phosphate (PO ₄ ³⁻)	ND	295	66.1	42.8
Lithium (Li ⁺)	ND	ND	ND	ND
Sodium (Na ⁺)	6400	10800	2560	328
Ammonium (NH ₄ ⁺)	206	540	1050	367
Potassium (K ⁺)	481	4470	1160	644
Magnesium (Mg ²⁺)	278	691	2600	298
Calcium (Ca ²⁺)	2690	5210	24000	3710
Total	22695	49845	108662	6044

SEM-EDS Analysis

SEM-EDS analysis was conducted to obtain a more comprehensive understanding of the compositions of the dust samples. Based on the EDS area mapping analysis, the major elements detected in the three natural dust samples were: *C, O, Na, Mg, Al, Si, S, Cl, K,* and *Ca*. The results indicated the existence of naturally abundant inorganic minerals. Big variations were found among the three natural dust samples in terms of weight percentages of *Na, Mg, S,* and *Cl*. Due to the limited sensitivity of EDS for low atomic order elements, elements such as nitrogen (N) and hydrogen (H) cannot be detected, even if they are present.

Based on both the EDS and IC analysis results, the dominant minerals in the three natural dust samples include quartz (SiO_2), feldspar (KAlSi_3O_8 - $\text{NaAlSi}_3\text{O}_8$ - $\text{CaAl}_2\text{Si}_2\text{O}_8$), calcite (CaCO_3), gypsum ($\text{CaSO}_4 \cdot 2\text{H}_2\text{O}$), and mica ($\text{SiO}_2 \cdot \text{Al}_2\text{O}_3 \cdot \text{K}_2\text{O} \cdot \text{Na}_2\text{O} \cdot \text{H}_2\text{O}$), most of which are the abundant minerals in the earth's crust. Chlorine (Cl) and sulfur (S) were also detected on some of the dust particles. It is believed that they are the constituents of inorganic salts adhering to some mineral particles [93][94].

pH and Conductivity

Dust samples were characterized by measuring the pH and conductivity of the aqueous solutions that were produced from them. We dissolved 250 mg of dust particles in 10 mL of deionized (DI) water of 18.2 meg-ohm grade, and measured the aqueous solution with a pH and electro-conductivity (EC) meter. The measurement results at an ambient temperature of 22°C are summarized in Table 12. The control sample was DI water, which had a pH of 6.8. DI water theoretically should have a pH of 7, with an equal amount of hydrogen (H^+) ions and hydroxide (OH^-) ions. However, as the water sits in open air, carbon dioxide (CO_2) begins dissolving into the water, forming carbonic acid. A small amount of absorption of CO_2 would drop the pH to less than 7. The three natural dust samples (Dust 1, Dust 2, and Dust 3) were all acidic with pH values between 5 and 6, while the ISO test dust (Dust 4) was basic with a pH of 9.3.

Table 12: pH and conductivity measurements at 22°C.

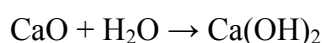
Sample Description	pH	Conductivity ($\mu\text{S}/\text{cm}$)
DI water (control)	6.8	<2
Dust 1	5.5	1640
Dust 2	5.3	2680
Dust 3	5.5	3645
Dust 4	9.3	106

The pH of Dust 4 was basic, which can be explained by its key composition. Based on the material datasheet of Dust 4 (ISO test dust – A2), there is a large weight percentage of silicon dioxide and different metal oxides, as listed in Table 13.

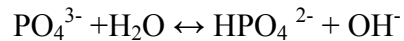
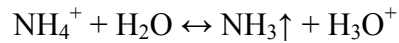
Table 13: Chemical compositions of Dust 4 (ISO test dust).

Chemical Ingredient	Weight Percentage (%)
SiO_2	68 - 76
Al_2O_3	10 - 15
Fe_2O_3	2 - 5
Na_2O	2 - 4
CaO	2 - 5
MgO	1 - 2
TiO_2	0.5 - 1.0
K_2O	2 - 5

Silicon dioxide does not react with water. Aluminum oxide, iron (III) oxide, and titanium dioxide are insoluble in water. The other metal oxides are basic oxides, which means that they react with water to form a base. Some examples are shown below.



In contrast to Dust 4, the aqueous solutions produced from the natural dust samples were acidic. This was related to the ionization and hydrolysis of the dominant substances in the dust samples. Ion analysis showed that the natural dust contains weak base cations of ammonium ion (NH_4^+), which can hydrolyze to form H_3O^+ with acidic properties. The phosphate ion produces hydroxide ions in the hydrolysis steps as shown below, causing the solution to be basic. When the concentration of ammonium ions outweighed the phosphate ions, the overall solution became acidic.



The ion analysis cannot directly detect the hydrogen ion concentration due to the limitation of the IC standards. NH_4HSO_4 and $(\text{NH}_4)_2\text{SO}_4$ are two common water soluble salts detected in the dust samples. The identification of ammonium and sulfate ions indicated the presence of NH_4HSO_4 and $(\text{NH}_4)_2\text{SO}_4$ in the natural dust collected in this study. The ionization of NH_4HSO_4 can produce hydrogen ions.



The conductivity of an aqueous solution can be approximated using the following relationship:

$$EC = \sum(C_i \times f_i)$$

where EC is the electrical conductivity in the unit of $\mu\text{S}/\text{cm}$, C_i is the concentration of ionic species i in the solution with a unit of mg/L , and f_i is the conductivity factor for ionic species i . The conductivity factor due to divalent cations is more than that of the mono-valent cations. The above statement is not true for anions. For example, the

conductivity factors for chloride (Cl^-), sulfate (SO_4^{2-}), and nitrate (NO_3^-) are 2.14, 1.54, and 1.15 $\mu\text{S}/\text{cm}$ per mg/L , respectively.

The conductivity differed among the tested dust samples. Dust 3 showed the highest conductivity, 3645 $\mu\text{S}/\text{cm}$, which was about 34 times the conductivity of Dust 4. The conductivity of the DI water was less than the lowest detection limit of the EC meter, which is 2 $\mu\text{S}/\text{cm}$.

The conductivity of the aqueous solution produced from different dust samples is a function of the ion concentrations, as shown in Equation (2). Dust 3 has the highest total ion concentration, 108,662 ppm, and the highest conductivity, 3,645 $\mu\text{S}/\text{cm}$. Dust 4 has the lowest total ion concentration, 6,044 ppm, and the lowest conductivity, 106 $\mu\text{S}/\text{cm}$.

Moisture Sorption Study

The moisture sorption study was conducted on 5 different specimens: the four dust samples and a comb structure test board. Before soaking, the specimens were baked for 48 hours at $125 \pm 5/0$ °C. This step removed the moisture from the specimen. The weights of the specimens did not change during the last portion of the bake out, which indicated that moisture content in the specimens had reached the equilibrium with the baking environment. After the bake out, the weight of the specimens was considered to be the dry weight. Then, the specimens were soaked at 90% RH and 50°C for 5 days. The

weights of the specimens, known as the wet weight, were recorded. The weight gain at any time t during the soaking phase is calculated using the following Equation.

$$Weight_Gain(t)(\%) = \frac{(wet_weight(t) - dry_weight) \cdot 100}{dry_weight}$$

Figure 24 shows the weight gain of all the specimens. It can be seen that the weight gains stabilized after 48 hours for all specimens. The intervals between readouts were shorter in the first 8 hours than in the later period of the soaking test, since more rapid weight changes were expected in the early stage.

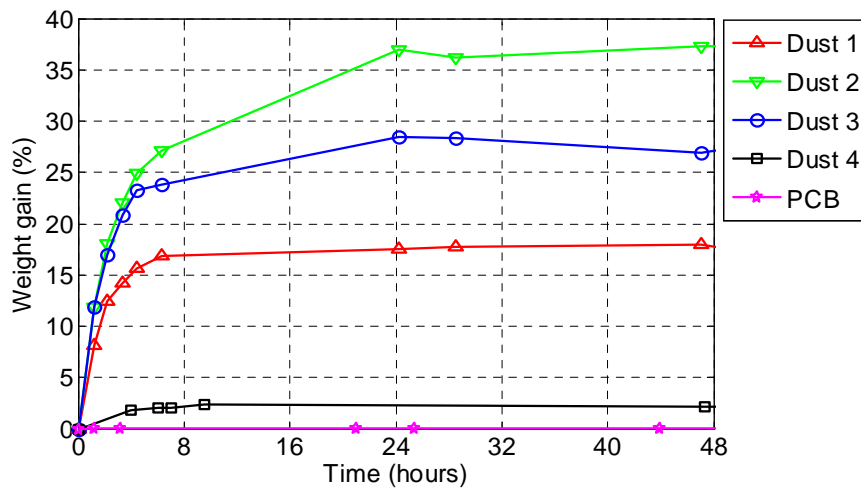


Figure 24: Moisture soak plot of different specimens.

Table 14 summarizes the percentages of weight gain of the different specimens at the end of 48 hours. The weight gain was normalized to the dry weight found after 48 hours of baking. Dust 2 had the highest weight gain of 37%, followed by Dust 3 (27%), and Dust

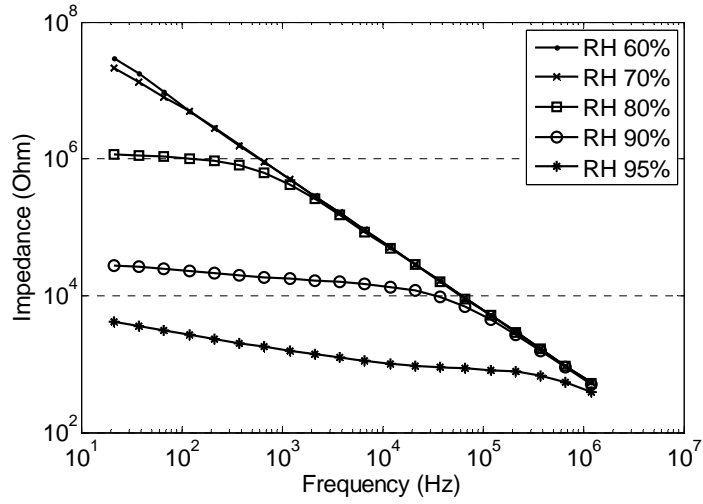
1 (18%). Dust 4 (ISO test dust) had the lowest weight gain among the four dust samples, 2.5%. The weight of the comb structure test board only increased 0.25%, which indicated that dust is a stronger moisture absorber than the dust contaminated test board.

Table 14: Weight gain at 48 hrs.

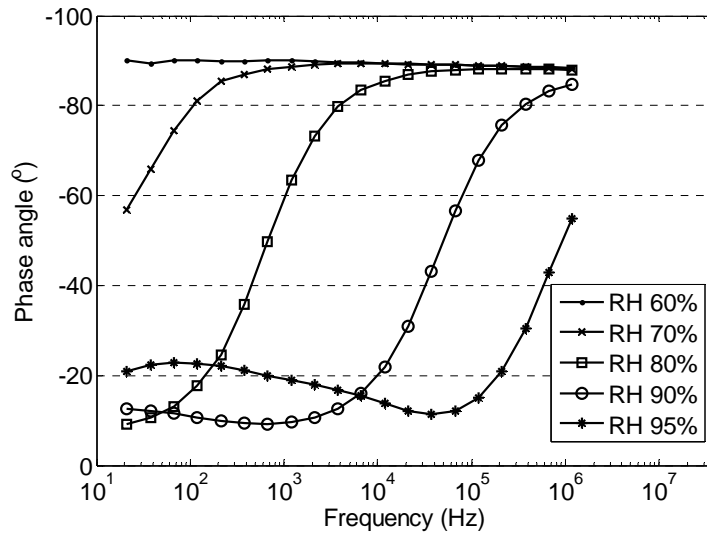
Specimen	Weight gain
Dust 1	18%
Dust 2	37%
Dust 3	27%
Dust 4	2.5%
Test Board	0.25%

Relative Humidity Effect

Relative humidity tests were performed for Dust 1 and Dust 3. Figure 25 show the Bode magnitude and phase angle plots of a test coupon at the dust deposition density of 2X and at different RH levels. The impedance magnitude at the lower end (20 Hz) was extracted the impedance data at 20 Hz over the tested RH range. The results were based to plot the trend over the tested RH range for different deposition density levels. Figure 25 shows on tests with a constant temperature of 40°C and RH values varying from 50% to 95%. For Dust 1, the test coupons with each of the four different dust deposition densities showed similar trends. At lower RH levels (e.g, from 50% to 70% for 1X deposition density and 50% to 65% for 3X deposition density), the impedance was relatively constant above 10^7 ohms. When the RH reached a certain range, the impedance of the test coupons between two electrodes started degrading by orders of magnitude. When the RH was at 95%, the impedance values for the test coupons were in the range of 10^3 to 10^5 ohms.



(a)



(b)

Figure 25: Bode plot at different RHs at dust deposition density 2X at 40°C (Dust 1). (a) Bode magnitude plot, (b) Phase angle plot.

The RH range between the start of impedance degradation and a failure threshold of 10^6 ohms is defined as the critical transition range. The starting point was defined as the RH level above which impedance drops by 10% of its initial value (which is the impedance

value measured at 50% RH), and the end point of the critical transition range is defined as the RH level when impedance is at the failure threshold of 10^6 ohms shown in Figure 26. In this group of a total of 12 test boards, the initial impedance was around 10^7 ohms, and 10% of its initial value was 10^6 ohms. For example, at dust deposition density 3X, the starting point of the critical transition range was 65%, since above 65% (at 70% RH) the impedance dropped to 5×10^6 ohms. The impedance decreased by more than 10% of the initial value. The end point of the CRH range was 78%, at which the impedance was 10^6 ohms. The critical transition ranges of RH for the dust samples were identified in Figure 26.

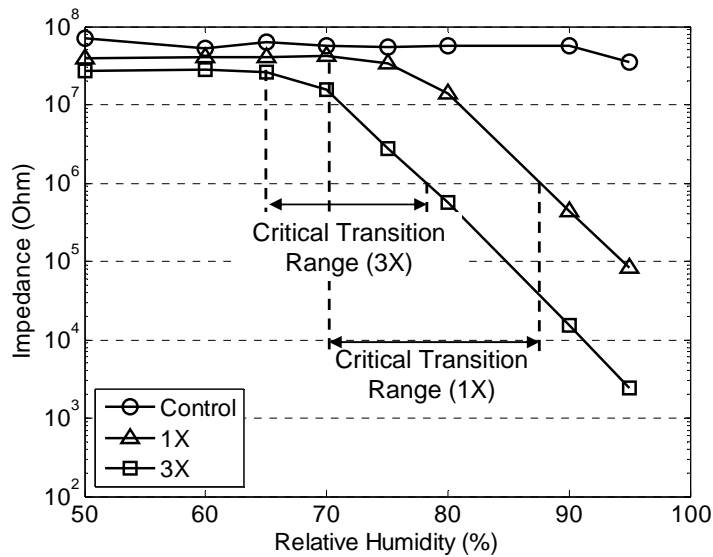
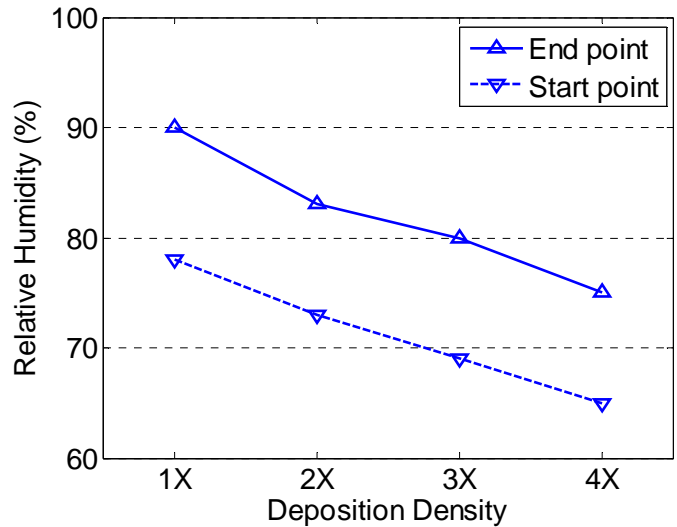


Figure 26: Impedance magnitude trend over the tested relative humidity range for control boards and Dust 1 deposited boards with a deposition density of 1X or 3X at 40°C.

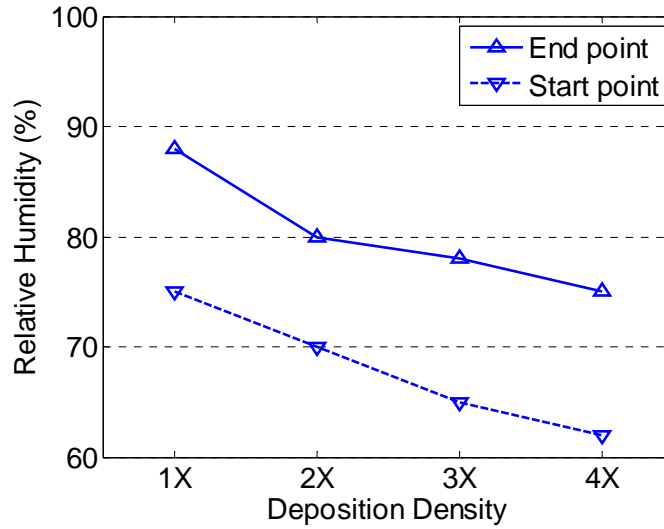
The identified critical transition range varied with the dust deposition density. With an increase in dust deposition density, the critical range shifted to lower values. Figure 26 shows that the impedance never dropped below 5×10^7 ohms over the tested range of RH

for the control group. Figure 27 (a) shows the relationship between the start and end points of the critical transition range and the dust deposition density for dust 1. Both the starting points and the end points are the averaged results of the three samples.

Critical transition ranges of RH were also identified on Dust 2 at different dust deposition densities. The start and end points of the transition ranges of Dust 2 were different compared to those of Dust 1 at the same deposition density. The transition range of Dust 2 showed a similar dependency on dust deposition density as Dust 1. Figure 27 (b) shows that the start and end points of the critical transition range decreased with an increase in the deposition density for Dust 2.



(a)



(b)

Figure 27: Dependence of critical transition range on dust deposition density based on average results of three samples at 40°C. (a) Dust 1, (b) Dust 2.

Temperature Effect

Figure 28 shows the results from the tests with a constant RH of 90% and a temperature varying from 20°C to 60°C. The magnitude of the impedance at 20 Hz taken from the Bode magnitude plot of Dust 1 was shown in Figure 28 over the tested temperature range. The test coupons included the boards deposited with four different dust deposition densities and 3 control boards without dust deposition. They all showed similar monotonic decrease with temperature. The impedance dropped around one order of magnitude for each 10°C increase in temperature in the range of 20°C to 50°C. As the temperature reached between 50°C and 60°C, the measured impedance did not change significantly. This trend was consistent for two different types of dust at different deposition densities.

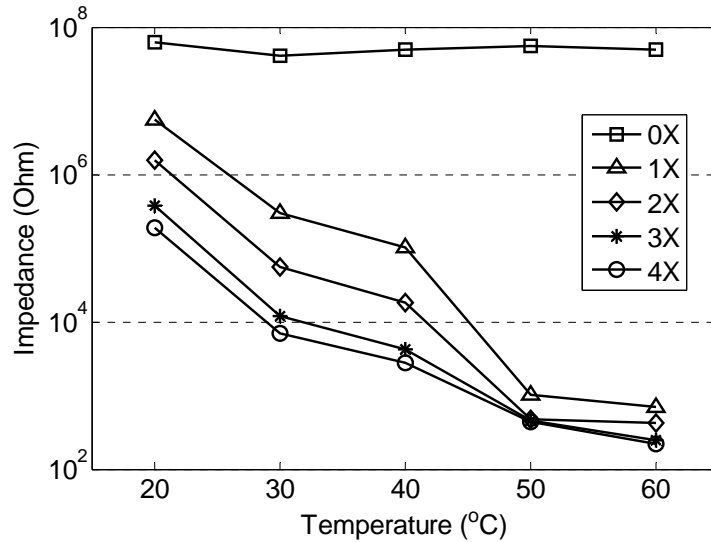


Figure 28: Temperature effects on impedance magnitude at 20 Hz at different dust deposition densities at 90% (Dust 1).

Comparison of Different Dusts

In the comparison study of different dust, RH tests and temperature tests were conducted and THB tests were performed to include the electrical field effect. Control samples (test boards without dust deposits) with a sample size of 3 were included in each group of tests.

Varying Relative Humidity Tests

Figure 29 shows the impedance data of test boards deposited with different dust samples during the RH test. The RH varied from 40% to 95% with a constant temperature of 40°C. The impedance data were measured at 20 Hz over the tested RH range. Four different types of dust were deposited at the same deposition density of $2 \pm 0.2 \text{ mg/in}^2$. At lower RH levels less than 50%, the impedance stabilized at a value greater than 10^7 ohms and had little change as shown in Figure 29. Several data points overlapped when the RH

value was low. The critical transition region of RH can be observed in Figure 30. When the RH increased to the critical range, the impedances of the test boards between two electrodes started decaying in orders of magnitude per 10% RH increase over the RH range. The control samples had a higher impedance value compared to the other groups, greater than 10^7 ohms, in the RH test showing less than 0.5 decade of drop of impedance over the tested RH range.

The critical transition ranges varied for test boards deposited with different dust samples. The failure threshold was chosen to be 10^6 ohms. If the impedance of a test board drops equal to or below this threshold, it is considered a failure due to loss of impedance. Therefore, the test conditions of 85%, 60%, 82%, and 90% RH at 40°C experienced loss of impedance failure for the test boards deposited with Dusts 1, 2, 3, and 4, respectively. Linear interpolation is used when the data do not have a point match at the failure threshold exactly.

A lower RH value for failure indicates that the dust is 'easier' to cause the loss of impedance. The impact of dust on loss of impedance was evaluated based on the RH values at which the impedance of the samples crossed the failure threshold at 10^6 ohms. When a dust sample had a greater impact on the loss of impedance, the impedance of the test sample dropped at a higher rate with the increase of RH, resulting in a lower RH value at the failure threshold. Dust 2 had the greatest impact, while Dust 4 had the lowest impact based on this criterion. The impedance values of Dust 2 deposited test boards reached the failure threshold of 10^6 ohms when the RH stepped up to 60% RH. In

comparison, the impedance of test boards deposited with Dust 4 (ISO test dust) dropped below the threshold until the RH was stepped up to 90%.

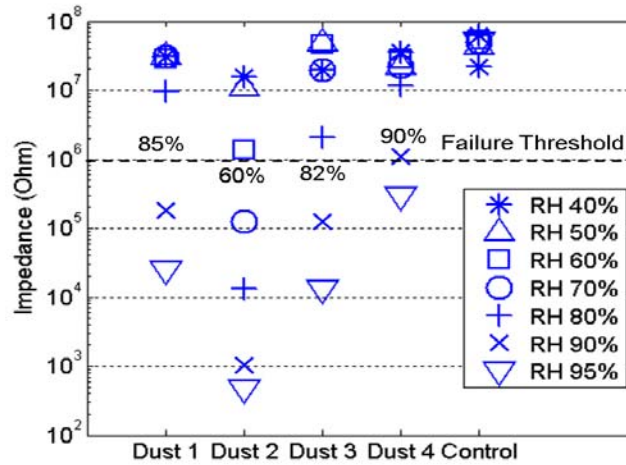


Figure 29: Comparison of impedance data of test boards deposited with different dusts under RH tests

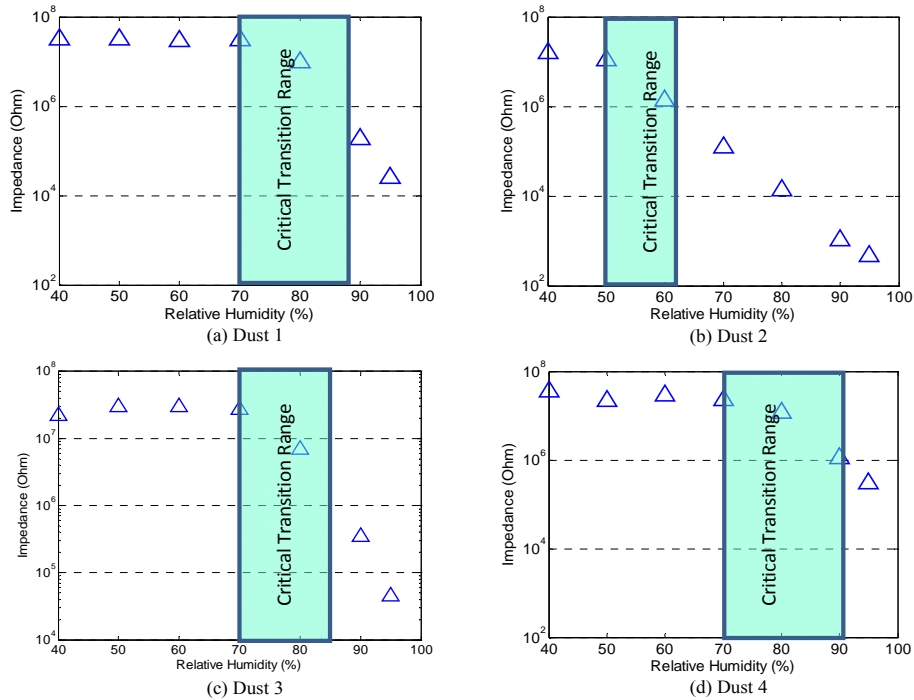


Figure 30: Critical transition ranges of different dusts.

Varying Temperature Tests

Figure 31 shows the impedance data of test boards deposited with different dust samples of the same deposition density under a varying temperature test. The impedance data were measured at 20 Hz. The temperature varied from 20°C to 60°C, with a constant RH of 80%. The impedance data showed a monotonic decrease with temperature for all dust samples, as shown in Figure 28.

The failure threshold of 10^6 ohms was applied in this test. Figure 31 shows that the test conditions of 26°C, less than 20°C, 20°C, and 60°C at 80% RH resulted in a loss of impedance for the test boards deposited with Dusts 1, 2, 3 and 4, respectively.

The impact of dust on loss of impedance was evaluated based on the temperature values at which the impedance of the samples crossed the failure threshold of 10^6 ohms. The impact of dust contributed to the difference in the impedance of the dust contaminated samples and the control samples. When a dust sample had a greater impact on the loss of impedance, the impedance of the test sample dropped to a lower level with the increase of temperature, resulting in a lower temperature value at the failure threshold. Dust 2 had the greatest impact, while Dust 4 had the lowest impact based on this criterion.

The impedance value of Dust 2 was approximately one magnitude below 10^6 ohms when the RH was 20°C. For Dust 4 (ISO test dust), the impedance did not drop below the threshold as the temperature reached 60°C.

Dust 1 and Dust 3 had a slightly higher temperature value at the failure threshold than Dust 2, but all the three natural dust showed much lower temperature values than Dust 4. Therefore, the impacts of dust on loss-of impedance with the change of temperature were different among the tested dust samples.

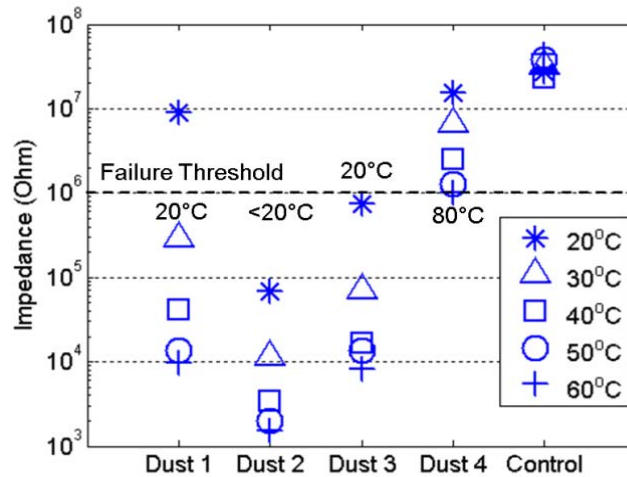


Figure 31: Comparison of impedance data of test boards deposited with different dusts under temperature test

Impact of Dust during Temperature-Humidity-Bias Test

The critical RH range and temperature conditions were identified in the previous tests. The THB tests were conducted at 50°C and 90% RH with an electrical field of 10 VDC. The environmental conditions were chosen to shorten the conductive path formation step. The total test duration was 144 hours. Test boards were deposited with different dust samples at the same dust deposition density of $2 \pm 0.2 \text{ mg/in}^2$. The failure criterion was defined as one decade drop from the initial resistance value in this group of tests. A resistance monitoring plot of a control sample is shown in Figure 32. The resistance

remained over 10^8 ohms without dropping during the entire test period. A resistance plot of a Dust 3 deposited test board with 3 consecutive resistance drops is shown in Figure 33. The initial value of the resistance is at 10^6 ohms. The time that the second drop occurred (~ 7 hours) was considered as the failure point since the resistance value is below 10^5 ohms, which is one decade lower than the initial value of 10^6 ohms.

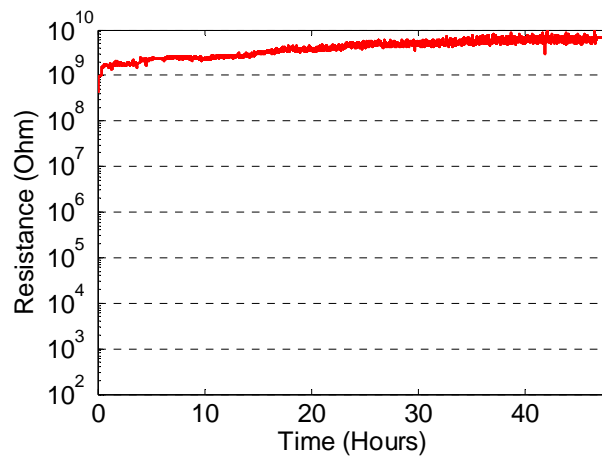


Figure 32: The resistance monitoring plot of a control sample.

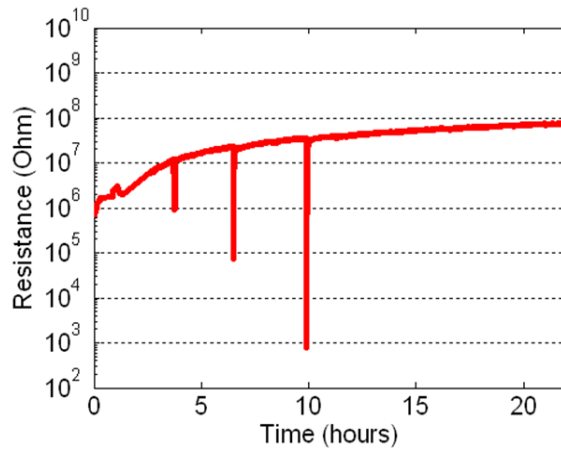


Figure 33: The resistance-monitoring plot of a test sample deposited with Dust 3.

Different dust samples exhibited dissimilar TTFs. The TTFs of different dust deposited test boards are summarized in Table 15. The tests were suspended if the boards had not failed by 144 hours, shown as a letter “S” in the TTF column. No failures were observed in the control group, which had a higher resistance value across the tested period than the dust-deposited groups.

Table 15: Summary of the time-to-failures of different types of dust.

Dust Type	Sample	TTF (hrs)	Averaged TTF (hrs)
Dust 1	1	142	115
	2	S*	
	3	S*	
	4	30	
Dust 2	1	71	85
	2	71	
	3	54	
	4	S*	
Dust 3	1	7	29
	2	28	
	3	30	
	4	50	
Dust 4	1	42	119
	2	S*	
	3	S*	
	4	S*	
Control	1	S*	>144
	2	S*	
	3	S*	

In the four groups of dust-deposited test boards, the group with Dust 3 had the lowest average TTF, 29 hours. All four test boards in this group failed. The failed samples were removed from the test chamber and examined by optical microscope and SEM-EDS. ECM and corrosion were observed in more than 10 places for every board in this group. Cu, S, and Cl were detected in the ECM area. Figure 34 shows the metal migration between two electrodes on a Dust 3 deposited test board.

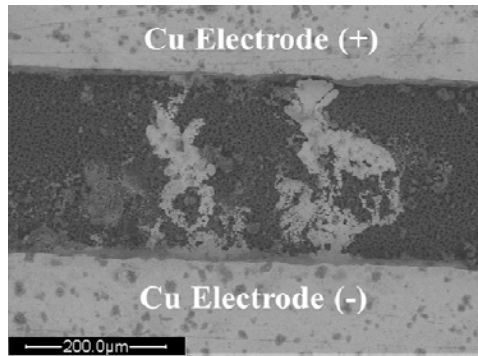


Figure 34: ECM on Dust 3 deposited test board

Dust 2 deposited test boards had the second shortest average TTF of 85 hours. One of the four test boards did not fail at the end of the 144 hour testing and was suspended. 144 hours was used for the suspended board in the calculation. Therefore, the actual TTF is greater than 85 hours. The same calculation was applied to other groups for any suspended board. For the failed boards, ECM and corrosion were observed under the SEM in multiple places. In some places, the copper migrated over the fiber (see the white box area in Figure 35). This is because fiber can absorb moisture and form a conductive path, thereby promoting metal migration under an electrical field.

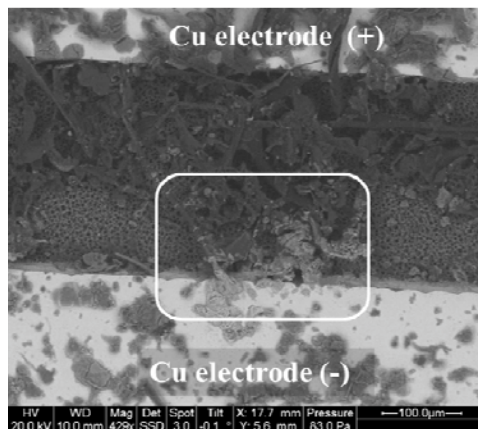


Figure 35: ECM on Dust 2 deposited test board showing metal migration over the fibers

Dust 1 deposited test boards had the third shortest TTF of 115 hours. Two of the four test boards were suspended. Corrosion was observed under the SEM in more than 10 places for both the failed and un-failed boards in this group (see Figure 36). It was because if the corrosion products did not bridge two adjacent electrodes, the drop of impedance did not reach the failure criteria. Cu and Cl were detected on the corroded areas. It is believed that Cl was dissolved from the dust contamination and caused the corrosion of copper.

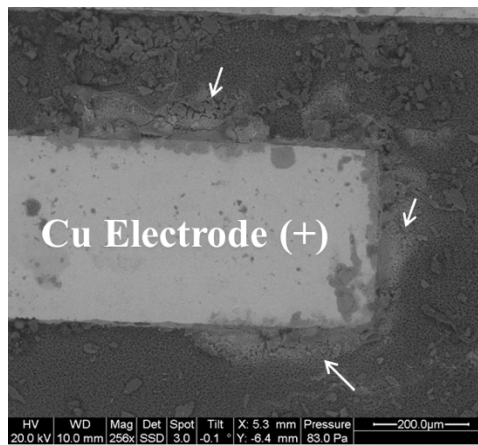
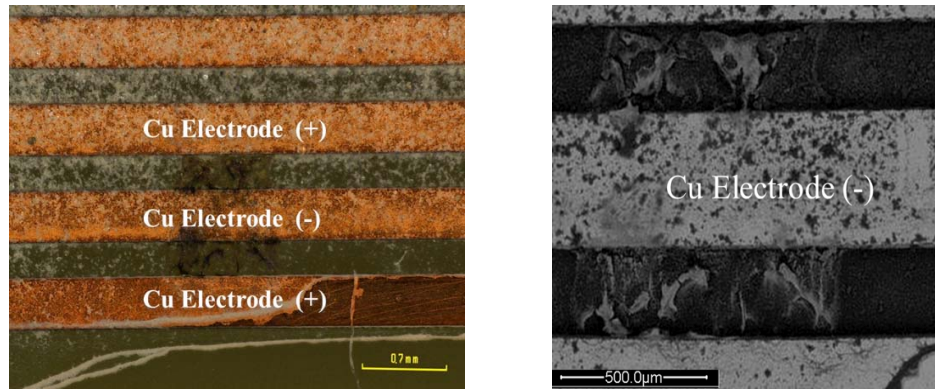


Figure 36: Corrosion on Dust 1 deposited test board.

The test boards deposited with Dust 4 had the highest average TTF among the four groups, 119 hours. Only one board failed during testing. No corrosion or ECM was observed, except in one location in the failed board. Both optical and SEM images of the failure site are shown in Figure 37. Metal migration was observed. Cu and Br were detected on the migrated areas. Bromide was not detected in the compositional analysis of Dust 4 (ISO test dust), as shown in Table 15. Thus, Br is believed to have leached from the FR4 substrate of the test board, as FR-4 epoxy resin systems typically employ

bromine to facilitate flame-resistant properties in FR-4 glass epoxy laminates. Therefore this failure was not directly related to the dust contamination on the board.



(a) Optical image

(b) SEM image

Figure 37: ECM on Dust 4 deposited test board

Chapter 7: Discussions

Relative Humidity Effect

When dust was present at the surface of the substrate, it was distributed across the space between the conductors on the PCB as well as on the copper traces. Note that some dust particles were also deposited on the surface of the copper traces. With dust contamination, moisture was attracted between adjacent electrodes through physical and chemical processes. Some components in the dust were hygroscopic substances, such as salts and organic compounds, which increased the total moisture sorption capacity through absorbing or adsorbing water molecules from the atmosphere. The soluble substances transitioned from solid particulate on the surface to a concentrated liquid layer through the deliquescent process. Capillary condensation was another process that caused the increasing moisture content. Instead of taking place on the surface, it took place in a porous medium by multilayer adsorption from the vapor; thus it contributed little to the formation of a continuous water path on the PCB surface [95]. On the dust deposited test boards, capillary condensation could occur in the porous mineral particles, in dust particle surface cracks, or between the glass fibers in the PCBs.

As RH approached the starting point of the critical transition range, the salts began to deliquesce. There exists some water concentrated on the water soluble salts or mineral particles with salts attached. The wetting of the surface was controlled largely by the soluble contaminants; thus the liquid layer was likely to be very concentrated. Since the

amount of water was limited, it had not yet formed a continuous path that would allow the ions to move freely to carry current.

The deliquescence process takes place when the RH reaches the CRH of the mixed salts in the dust samples. At or above the CRH, water soluble salts absorb relatively large amounts of water from the atmosphere if exposed to it, forming a liquid solution. As the RH exceeded the CRH of the mixed salts in the dust samples, the deliquescence process continued to proceed by absorbing more vapor from the atmosphere. When the water absorbed in the deliquescent particles increased with RH, the size and mass of the particles increased. The solid particles transformed into saline droplets. As the RH continued to increase, the droplets connected to each other to form a continuous path, causing significant impedance degradation. This occurred at the starting point of the critical transition range.

The starting points of the critical transition ranges of RH were dependent on the CRH of the mixed salts in the dust. The natural dust samples were a mixture of different substances, which included a number of deliquescent compounds, such as NaCl, NaNO₃, NH₄HSO₄, (NH₄)₂SO₄. These compounds have different CRHs, as shown in Table 16 [82]. For example, the CRH of NH₄HSO₄ is 39% at 25°C, whereas it is 75% at 25°C for NaCl. The CRH of the mixed salts in the dust was affected by the weight percentages of the different deliquescent substances. Dust 2 contained more ions, such as Cl⁻, SO₄²⁻ and NO₃⁻. It is believed that Dust 2 had more water soluble salts with low CRH, such as

NH_4HSO_4 , MgCl_2 . Therefore, the Dust 2 deposited board had a lower starting point of critical transition range compared to Dust 1 at the same deposition density.

Table 16: CRH of possible inorganic compounds in dust samples at 25°C.

Compound	CRH (%)
NaCl	75
NaSO ₄	84
(NH ₄) ₂ SO ₄	79
NH ₄ HSO ₄	39
MgCl ₂	32
NaNO ₃	74

The critical transition range depends on the CRH of the mixture of salts in dust, but it is different from the CRH. A schematic plot of the particle mass change of the mixed salt particles with RH during a deliquescence process is shown in Figure 38 which is reproduced from [96]. When the environmental RH reached the CRH, the deliquescent substances in the dust samples began to absorb moisture. Impedance degradation was observed when a continuous conductive path formed, which occurred as a result of the deliquescence process. Therefore, the starting point of the critical transition range is expected to be higher than the CRH of the mixed salts in the dust.

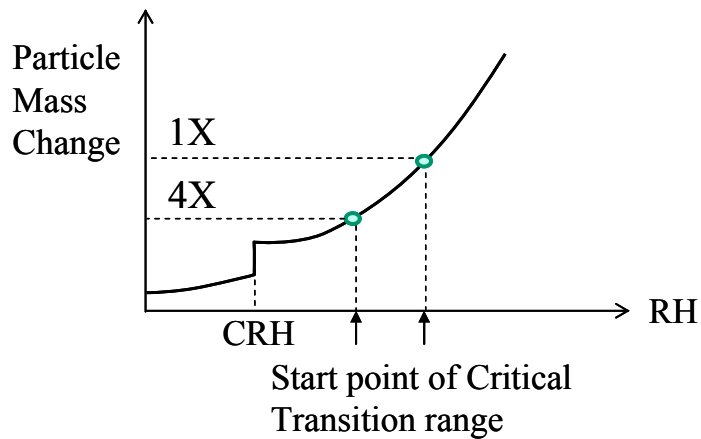


Figure 38: Mass change of a mixed salt particle with relative humidity.

With the increase of dust deposition density, the starting point of the transition ranges decreased for both dusts. This is due to the reduced spacing between dust particles at a higher deposition density. A schematic drawing of dust particles deposited on the substrates at two different deposition densities of 1X and 4X is shown in Figure 39. The mineral particles are illustrated as polygons. The black dots represent the mixed salts that are either attached on the mineral particles or directly onto the substrate. The grey areas represent the size increasing of the mixed salts after absorbing a large amount of water from the atmosphere during the deliquescence process. During the deliquescence process, the mixed-salts absorb water, increase in size and mass, and eventually form a liquid. When the liquid covers the distance between particles, a continuous conductive path is formed and followed by measured impedance degradation. As shown in Figure 39, the distances between mixed salts were shorter at a higher dust deposition density, requiring less water sorption to form a continuous conductive path.

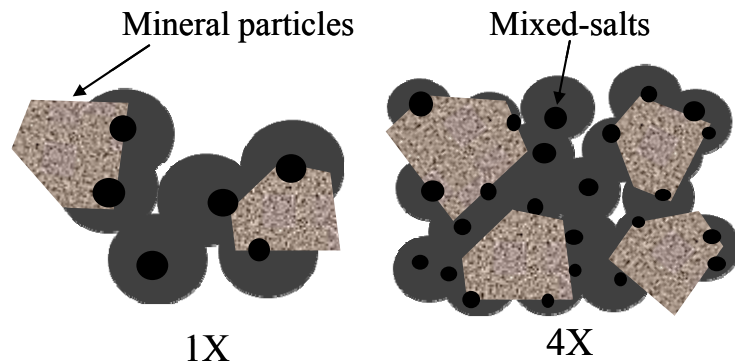


Figure 39: Schematic drawing of dust particles deposited on the substrate at 1X and 4X.

Temperature Effect

The impedance decreased as the temperature increased. As the temperature reached between 50°C and 60°C, the impedance did not change significantly. An equivalent circuit model of the impedance data was used to understand the failure mechanism of the impedance trend in the temperature tests. The measured impedance was decomposed into two parts: the bulk resistance and the interfacial impedance. The bulk resistance was the ohmic resistance of the electrolyte between the two electrodes formed by a water film with ions from dust contaminants. The interfacial impedance was determined by the Faradaic reactions and diffusion-controlled processes, both of which occurred at the interface between the electrode and the electrolyte. The interfacial impedance sometimes cannot be modeled as a resistor strictly following Ohm's law due to the presence of capacitive and non-linear components. The interfacial impedance is frequently modeled as a combination of Warburg impedance, charge transfer resistance, and double layer capacitance.

Figure 40 shows the equivalent circuit used to model the impedance data. Due to the complex nature of dust, there could be multiple chemical reactions that occur at the interfaces. Similar to [90], the circuit was simplified by combining the electric components that correspond to multiple possible chemical reactions at the two electrodes and disregarding the chemical reaction related to the formation of an oxide layer or other corrosion products on the electrodes. A modified Randles circuit from EIS literature was used to model the electric properties of the dust contamination between the two electrodes [22]. The bulk property of the system consisted of the bulk resistance (R_{bulk})

and the comb structure capacitance (C_{comb}). The bulk resistance is referred to as solution resistance in some EIS literature. As expected of any medium between electrodes, there is a capacitive response to AC voltage [97]. C_{comb} reflects the dielectric property of the space and FR-4 composite substrate between the interdigitated electrodes of the comb structure test board. The interfacial properties of the system is shown in the dotted box (see Figure 40) including the double layer capacitance (C_{DL}), charge transfer resistance (R_{CT}), and Warburg impedance (Z_W). In this research the values of Warburg impedance were not extracted from the equivalent circuit, because an accurate extraction of this element requires measurement at very low frequencies (below 1 Hz) [22], [97].

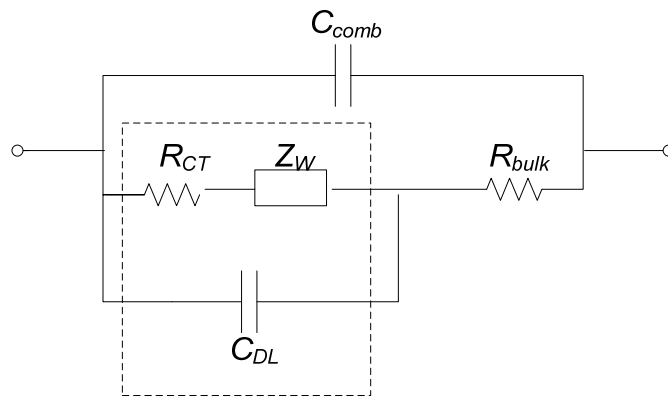
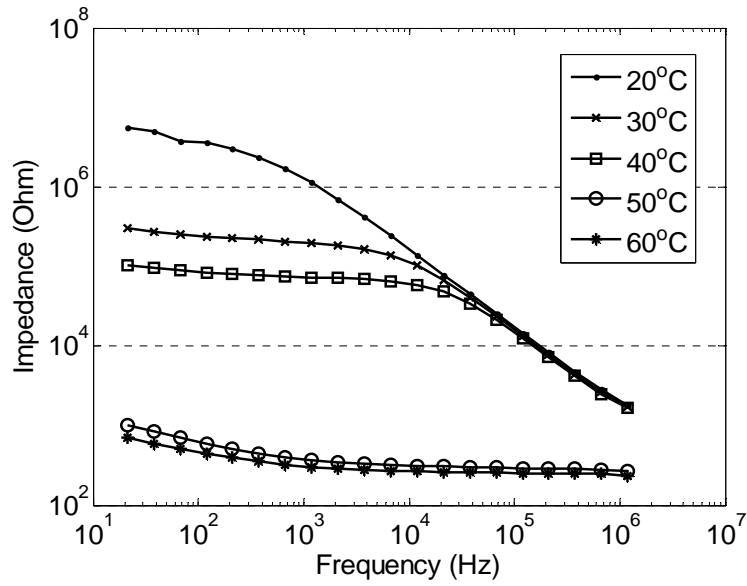
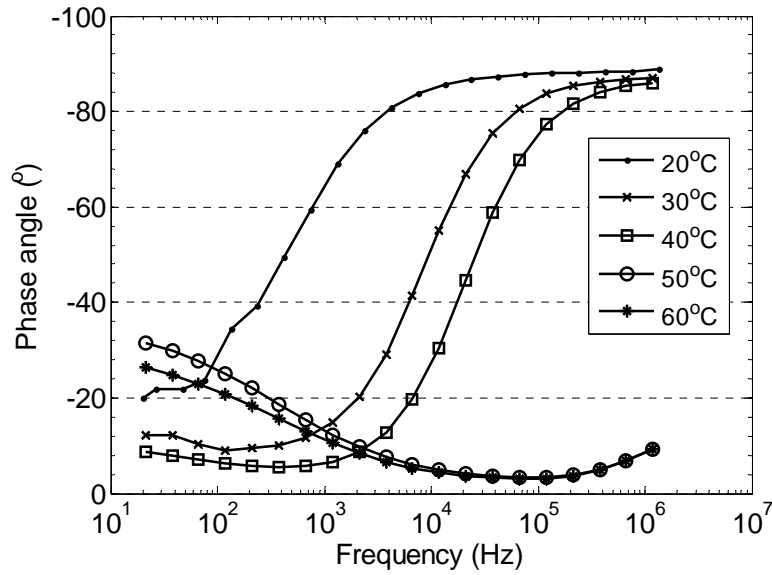


Figure 40: Equivalent circuit used for impedance measurement on dust contaminated test boards.



(a)



(b)

Figure 41: Bode plot at different temperatures at dust deposition density 1X at 90% RH (Dust 1). (a) Bode magnitude plot, (b) Phase angle plot.

Figure 41 shows the Bode magnitude and phase angle plots of a test coupon at the dust deposition density of 1X and at different temperature levels. The goodness of fit of the modeled parameters at different temperatures was evaluated using the equation below and is summarized in the last row of Table 17.

$$\sqrt{\frac{\sum_{i=1}^n (\log |Z_{i,mo}| - \log |Z_{i,me}|)^2}{n}} \quad (1)$$

Where $Z_{i,mo}$ is the modeled impedance at one of the frequencies, $Z_{i,me}$ is the measured impedance at one of the frequencies, and n the number of frequency points over the tested frequency range ($n = 201$ in this paper). In this study, the focus is the degradation of the bulk resistance as it is directly related to the effect of dust. Table 17 shows the extracted bulk resistance values from the data in the temperature tests. From the extracted values of R_{bulk} , it can be seen that as the temperature increased R_{bulk} decreased greatly. Figure 42 shows the trends of the impedance magnitude and the bulk resistance during the temperature tests. Both the impedance magnitude and R_{bulk} decreased as the temperature increased. At lower temperature between 20°C and 40°C, the differences between the impedance magnitudes and R_{bulk} were much less than one order of magnitude. At higher temperature between 50°C and 60°C, R_{bulk} was more than one order of magnitude lower than the impedance magnitude, indicating that the bulk resistance was not the dominant element in the impedance path. This difference is believed to result from the interfacial impedance. Due to the lack of data at low frequencies, these elements, such as diffusion-controlled impedance and charge transfer resistance, were not extracted. More in-depth analysis can be performed if more measurement points at lower frequencies were

available. Also a more sophisticated model with electrical elements associated with possible chemical reactions will be considered in future work.

Table 17: Summary of the results of mathematical fit to the equivalent circuit at different temperatures with 90% RH (Dust 1, 1X).

Parameters	20°C	30°C	40°C	50°C	60°C
R_{bulk}	2.91E+06	1.74E+05	6.50E+04	8.03E+01	7.87E+01
Residuals	9.00E-02	8.70E-02	5.00E-02	1.20E-03	1.20E-03

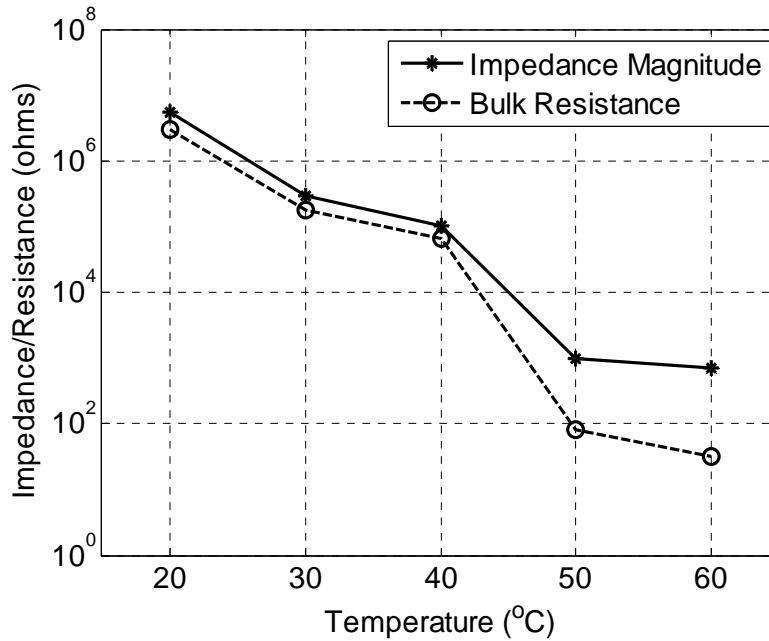


Figure 42: Impedance magnitude and extracted bulk resistance at different temperatures with 90% RH (Dust 1, 1X).

R_{bulk} describes the impedance of the solution formed by dust contamination. Its value depends on the continuity and thickness of the water film as well as the concentration of the charge-carrying ions in the water film. As temperature increased, the CRH of the mixed salts in the dust decreased [96]. As a result, more moisture was absorbed to form a thicker water film at a constant RH of 90% (above the CRH of the mixed salts in dust).

Meanwhile, the solubility of some inorganic compounds found in dust and corrosion products, such as CuCl_2 and NaCl , increase with temperature. Solubility measures the ability of a substance to dissolve in a fixed quantity of a solvent to form a saturated solution. As the solubility increases with temperature, more ions dissolved into the water film. The increased amount of water and the increased amount of ions contributed to the decrease of measured R_{bulk} .

Other Factors

The moisture adsorption of the PCB material can be neglected compared to the effect of dust. At 90% RH, a uniform water layer was adsorbed on the PCBs, as predicted by the Brunauer Emmett–Teller (BET) model in [9]. The thickness of the adsorbed layer on the PCB is related to the properties of the PCB material. More water will be adsorbed on hydrophilic surfaces compared to hydrophobic surfaces. The layers adsorbed on the PCB did not result in a significant impedance drop in the control test boards over the tested RH and temperature ranges as shown in Figure 28.

The presence of inert mineral materials that are not deliquescent may render the water film less continuous due to capillary action. Water condensation can form and make a continuous path around them. If mixed salts were attached on mineral particles with a multilayer structure, water condensation could cover inert particles. More tests using well controlled inert materials in terms of dimensions and concentrations should be conducted to investigate their effects.

Comparison of Different Dusts

The test results from varying temperature and RH studies indicated the impact of dust on loss of impedance. The failure threshold was set to be 10^6 ohms for both tests. Dust 2 had the greatest impact, while Dust 4 had the lowest impact based on this criterion for both tests, as shown in Table 18.

A degradation factor is defined in this paper to measure the difference in impedances between dust contaminated boards and control boards. The impedance (Z) includes a real component (Z') and an imaginary component (Z''), as given in $Z = Z' + jZ''$. Absolute impedance ($|Z|$) is used to characterize the impact of dust, defined as $|Z| = \sqrt{(Z')^2 + (Z'')^2}$.

The degradation factor (DF) for a dust sample is calculated as

$$DF_{T,RH,dust} = \log_{10} \left(\frac{|Z_{T,RH,control}|}{|Z_{T,RH,dust}|} \right)$$

where $Z_{T,RH,control}$ is the measured impedance at a temperature and relative humidity condition for the control samples, $Z_{T,RH,dust}$ is the measured impedance at the same temperature and relative humidity condition for the dust contaminated samples. The DF quantifies how much the impedance degrades due to the dust contaminations.

The DF varies for different dusts in the RH and temperature tests. The DFs calculated for RH test and temperature tests are shown in Figure 43 and Figure 44, respectively. All four dusts show different degradation factors. Dust 2 had the highest DFs over the tested ranges of RH and temperature. Dust 4 (ISO test dust) has the lowest DF over the tested temperature range. Dust 4 has the lowest DF in the RH test above 80%.

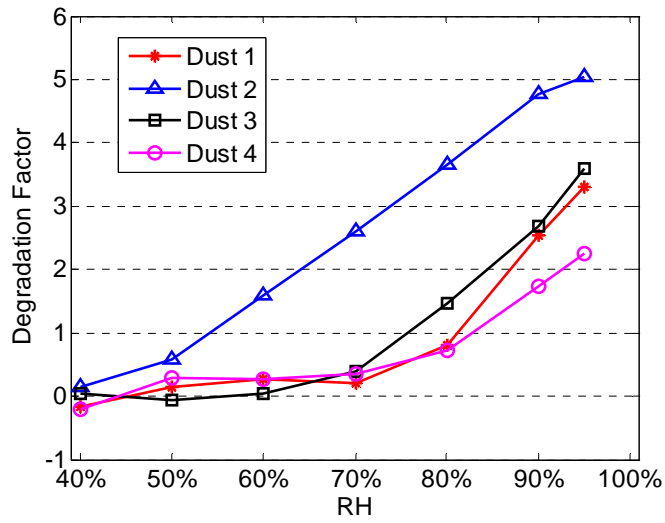


Figure 43: Degradation factors of different dusts in the RH tests at 40°C

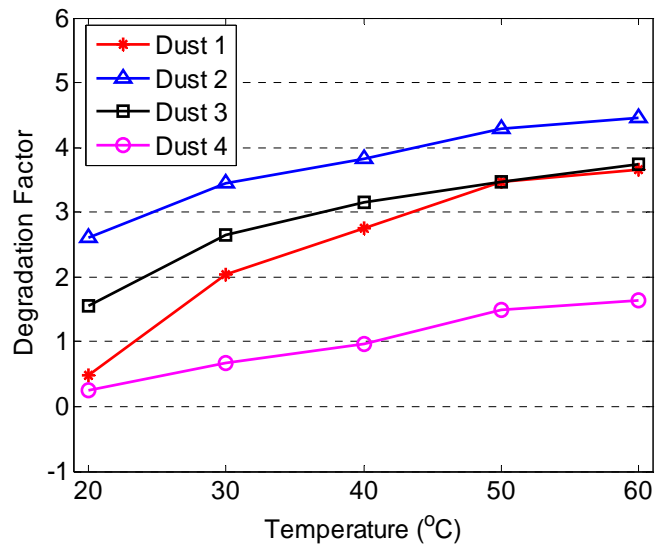


Figure 44: Degradation factors of different dusts in the temperature tests at 80% RH

In order to obtain a geometry-independent quantity, the conductivity was calculated from bulk resistance (R_{bulk}) and impedance magnitude ($|Z|$) extracted from the results in the RH tests for different dust contaminated boards (Spacing is 0.0254 cm). It was assumed that

the electrolyte formed by dust layer is distributed over the substrate surface as a film of uniform thickness. The conductivity for different dust-contaminated boards is plotted at different relative humidifies, as shown in Figure 45. Dust 2 showed the highest conductivity among the four dust samples, and Dust 4 had the lowest value over the tested RH range. The order of the four dust samples was consistent based on the calculations from both bulk resistance and impedance magnitude.

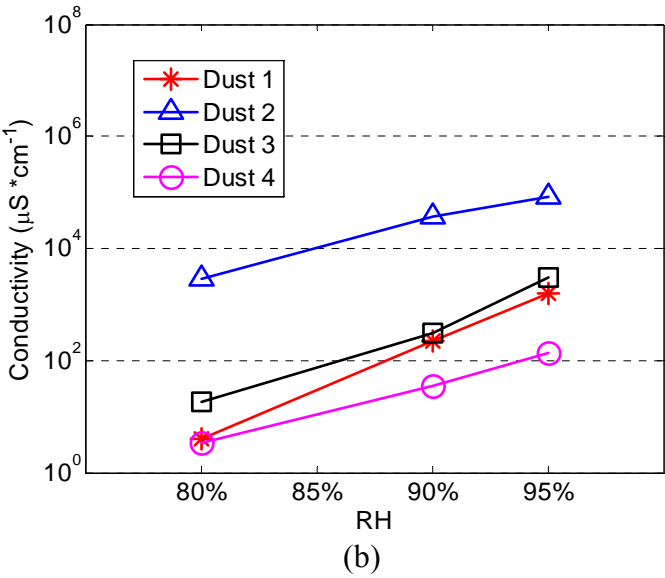
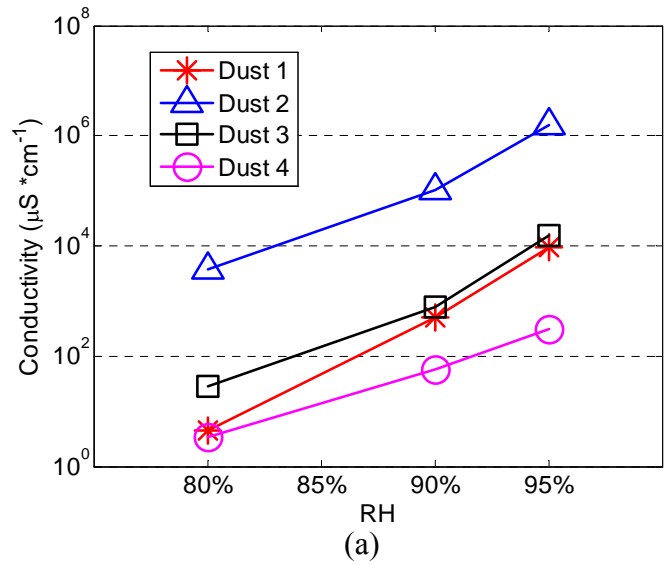


Figure 45: Conductivity of different dusts in the RH tests at 40°C. (a) based on R_{bulk} . (b) based on impedance magnitude $|Z|$.

Table 18 also showed a strong correlation between the moisture sorption ability of the dust and the impact on loss of impedance for these two tests. The dust with greater moisture sorption ability had greater impact on loss of impedance. A dust sample that has the greater moisture sorption ability can absorb or adsorb more moisture compared to the others at the same temperature and RH conditions. When the dust was deposited on the test boards, more moisture can be obtained on the PCB substrate, which is the prerequisite for the ions to dissolve from the dust contamination into the water film. Therefore, conductive paths were formed between two adjacent conductors, resulting in the loss of impedance.

The moisture sorption ability was determined by the percentage of hygroscopic substances, linen or fiber, and dust particle size distribution. The hygroscopic material is one of the critical compositions in the dust contamination, which can absorb and adsorb a large amount of water molecules from the atmosphere to increase the moisture content in the dust when its CRH is reached. Fibers in the dust absorb water by holding the water molecules in the space of the fiber structure or through chemistry due to the presence of cellulose in most fibers. Smaller dust particles have more surface area than larger dust particles, which can attract more water on the surface.

Dust 2 had relatively high hygroscopic substances as verified by the IC analysis. In addition, the average particle size of indoor Dust 2 was smaller than outdoor dust (Dust 1 and Dust 3), as Dust 2 was collected in a computer room with an air conditioning and

filtration system. Dust 2 also contained a more fibers compared to other dust samples, which also contributed to the high moisture sorption ability. In comparison, Dust 1 and Dust 3 contained a large amount of mineral particles, which can absorb less moisture compared to fibers. Moisture sorption ability of dust is the primary indicator on the loss of impedance in the temperature and RH tests.

Table 18: Summary of test results of different dust types

Tests		Dust 1	Dust 2	Dust 3	Dust 4
Characteristics of Dust	Moisture sorption @ 48 hrs	17%	37%	27%	2.5%
	Conductivity ($\mu\text{s}/\text{cm}$)	1640	2680	3645	106
	pH	5.5	5.3	5.5	9.3
	IC analysis (ppm)	22,695	49,845	108,662	6,044
Tests	RH Test	85%	60%	82%	90%
	Temperature Test	25°C	< 20°C	20°C	60°C
	TTF in THB (hours)	115	85	29	119

The leakage current between two conductors was carried by the ions in the water film on the substrate. The ions were dissolved from the dust contamination. The more ions, the higher the current, therefore the lower the impedance. One way to evaluate the impact of dust on impedance is to dissolve the dust samples in water and measure the conductivity of the aqueous solutions. The conductivity of dust aqueous solution can also be determined from the ion concentrations, as it is a function of the ion species and concentration in the water shown in Equation (2). However, the conductivity of dust solution is not the only criteria for the evaluation. Since the water film is the prerequisite for ionization to happen, without a continuous water film, a conductive path with ions cannot be formed. And due to the small amount of water, the water film is saturated with

dissolved ions [18]. The experiment data showed that the amount of absorbed water was still the predominant limiting factor compared to conductivity of water solution or the ion concentrations. For example, Dust 2 had the highest moisture sorption ability (37%) and the second highest conductivity (2680 $\mu\text{s}/\text{cm}$), while Dust 3 had the second highest moisture sorption ability (27%) and the highest conductivity (3645 $\mu\text{s}/\text{cm}$) in the dust samples. The test boards contaminated with Dust 2 and Dust 3 had a RH value of 60% and 82% as the failure threshold of 10^6 ohms, as shown in Table 18.

Dust contaminated test boards showed reduced lives compared to the control samples under the testing condition of 50°C, 90% RH, and 10 VDC. The TTFs for different dust types were quantified. The results showed that Dust 3 had the shortest life, followed by Dust 2, Dust 1, and Dust 4. Failure analysis of the failed boards showed that drops in resistance were caused by either ECM or corrosion products bridging adjacent conductors. ECM or corrosion was caused by the reactions of dissolved ions from the dust with the copper electrode material. If the reaction products migrated through a water film under the electrical field, ECM occurred. Dust 3 had the highest total ion concentration, and it also had the highest ion concentrations of chloride, sulfate, ammonium, and nitrate. The concentrations of ionic contaminations of Cl^- and SO_4^{2-} were the major contributing factors compared to other ions due to their corrosive nature. Chloride may cause corrosion of copper, depending on the concentration of chloride. The first step is the formation of CuCl , which may then undergo hydrolysis or oxygen reduction to form Cu_2O . Thus, the dissolution reaction occurs through the formation of a CuCl^{2-} soluble complex at specific sites, leading to the formation of micro-pits in the

initial stage of pitting. The soluble complex can migrate to the cathode, which increases the corrosion rate at a high chloride concentration ($> 10^{-3}$ M). When the sulfate co-exists with chloride, it can react with copper to form soluble corrosion products of CuSO_4 , which tends to migrate, thereby accelerating the corrosion process. The experimental results agreed with the statement. Dust 3 contains more sulfate ions than the other types of dust. More incidents of metal migration were observed in PCBs contaminated with Dust 3 than in Dust 1 and 2, due to the formation of soluble copper sulfate, which tends to migrate under electrical fields.

ECM and corrosion are caused by the electrochemical reactions between the metal conductors and the ionic contaminations in the dust in presence of moisture and under a bias. Both ECM and corrosion are results of the dissolution of metallic ions from the electrodes. ECM process consists of a sequence of steps, including path formation, metal dissolution, ion transport, metal deposition, and dendrite growth, where the dust contamination contributes to the path formation and metal dissolution steps. In the path formation step, dust can absorb a large amount of water to form a continuous water film as a conductive path. The reactive ions in the dust contamination dissolve into the water film and then react with the metal to cause metal dissolution. All species of ions dissolved from the dust into the water film can increase conductivity thus degrading impedance, however, only the reactive ions can cause metal dissolution, therefore only these ions promotes ECM or corrosion during the metal dissolution step. Both the ion species in the dust and dust moisture sorption ability should be taken into consideration when evaluating the ECM and corrosion failures.

The ISO test dust (Dust 4) is largely different from the natural dust collected from the field (Dust 1, 2 and 3) not only in the basic characteristic but also the impact on reliability. Dust 4 is largely composed of metal oxides from the mineral particles. It does not contain as many water soluble salts and natural fibers as those in the natural dust samples. As a result, natural dust had more than 8 times higher moisture sorption ability and 16 times higher conductivity than the ISO test dust sample, as shown in Table 18. As moisture sorption and conductivity are the key factors identified in this thesis, Dust 4 had the least impact on loss of impedance, metal migration and corrosion failures. Experimental results agreed with this observation. In the RH tests, the drop of impedance below the threshold was reached when the RH was stepped up to 90%. In the temperature tests, the failure point was reached when the temperature was increased to 60°C. Both values were much higher than those of the natural dusts, indicating that ISO dust is less likely than the natural dusts to cause loss of impedance failures under the same operating conditions of PCBs. In the THB tests, only one failure site was found in Dust 4 contaminated test samples. In addition, bromine was observed on the failure site. Since bromine was not detected in the dust samples through the IC analysis, the failure is likely due to leaching from the PCB boards, rather than from the dust contamination. Hence, the ISO dust did not cause metal migration or corrosion failures in the THB tests. The comparison results of ISO dust and the natural dust demonstrated that the ISO test dust is not an adequate representative of the natural dust.

Chapter 8: Field Data

This chapter presents analysis of a number of field failure PCBA samples due to ECM in presence of dust contaminations. The field samples used in this thesis are from telecommunication equipments used in un-controlled, out-door operating environment. The PCBAs used Sn-Pb solder paste and Sn hot air solder leveling (HASL) board finish. The design of the board was qualified through temperature-humidity-bias (THB) testing conducted at 85°C/85%RH, where it exhibited a good corrosion and ECM resistance. However, they failed in the field in a short period of time. Shorted leads were found in multiple places of the boards by electrical verification. And some of them are found to be caused by ECM.

Failure analysis was conducted on the boards including visual inspection under stereomicroscope, surface ionic contamination analysis by ion chromatography (IC), metal migration identification by X-Ray imaging, bulk chemical analysis by X-Ray fluorescence (XRF) analysis, as well as a semi-quantitative identification of the chemical compounds by scanning electron microscopy/X-ray energy spectroscopy (SEM/EDS).

Visual inspection showed particulate contaminations accumulated between leads of the surface mount components. The particulate contamination on the board was collected with a cotton swab, and then dissolved in a 75/25 v/v isopropanol (IPA)/H₂O solution. Some anions including nitrate (NO₃⁻), sulfate (SO₄²⁻) and chloride (Cl⁻) were identified on

the board by IC analysis. SEM/EDS analysis showed the metal migration between the shorted leads, which consisted of tin, lead and their oxides/hydroxides. In terms of the percentage of tin and lead, it varied based on the sampling location. Elements, such as O, Si, Ba, S, Ca and Br were also detected on the metal migration area, mixed with Sn and Pb dendrites. It indicated the presence of dust particles and dust had caused corrosion or migration [10].

Case Study 1: Solder Metal Migration with Ni/Pb/Au Lead

Finish

Figure 46 show an example of electrochemical migration between component leads. The spacing between two leads is about 250 μm . This component is a quad flat package (QFP) with copper leadframe and Ni/Pd/Au finish. The palladium deposition acts as an oxidation barrier for the underlying nickel, which is the actual bonding/soldering surface. A thin gold flash is applied to further improve the wettability of this finish. The compositions of the component leads were verified using XRF analysis as shown in Figure 46. Ni, Pd and Au, which constitute the three-layer structure of the lead finish material, are shown in the XRF spectrums. Copper as the base material of the leadframe is also revealed by this analysis.

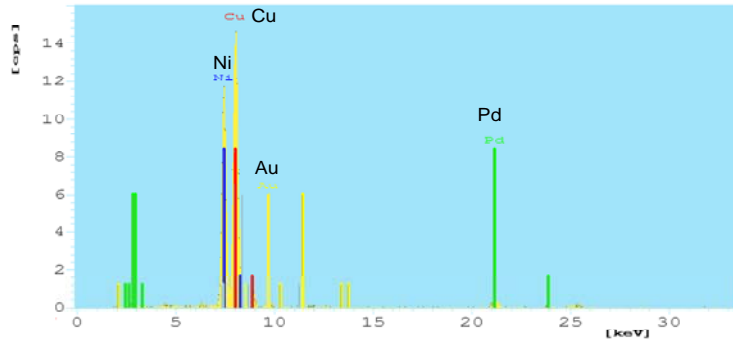


Figure 46: XRF spectrum of the component lead

Figure 47 is an optical image of the failed component with shorted leads. A copper trace connected to the failed package lead was marked by blue ink after electrical verification. A lot of deposits were observed between the failed lead and its neighboring leads.

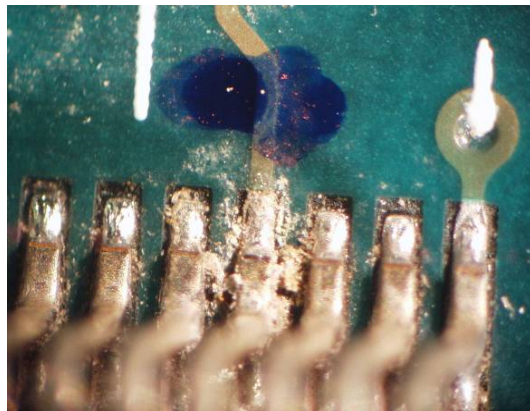


Figure 47: Optical image of the failed QSP component

X-ray analysis was performed on an area of the board with shorted leads. The X-ray image is shown in Figure 48. This X-ray image shows some metal migration between leads as indicated by the arrows. Comparing to Figure 47, it is believed that the deposits between leads are a mixture of migrated metals and particulate contaminations.

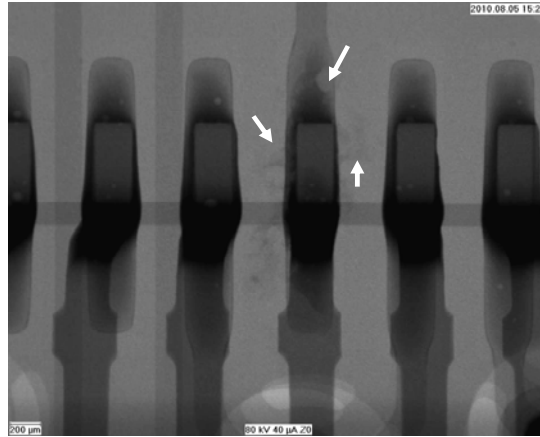


Figure 48: X-Ray image of the failed leads

Figure 49 shows the SEM image of the shorted leads. A lot of deposits are present spanning the space between the adjacent leads. EDS mapping shows that the dominant migrating elements are Sn and Pb, shown in Figure 50. The lead finish materials, Ni and Pd, did not migrate. Copper was exposed at the edge of the component lead due to the pre-plating process. It was also identified at the edge of the copper pad on the PCB. Only a trace level of gold was detected, which was shown in the mapping.

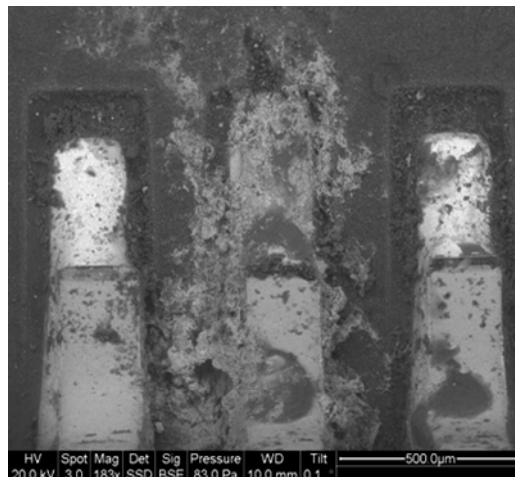


Figure 49: SEM image of shorted leads in example 1

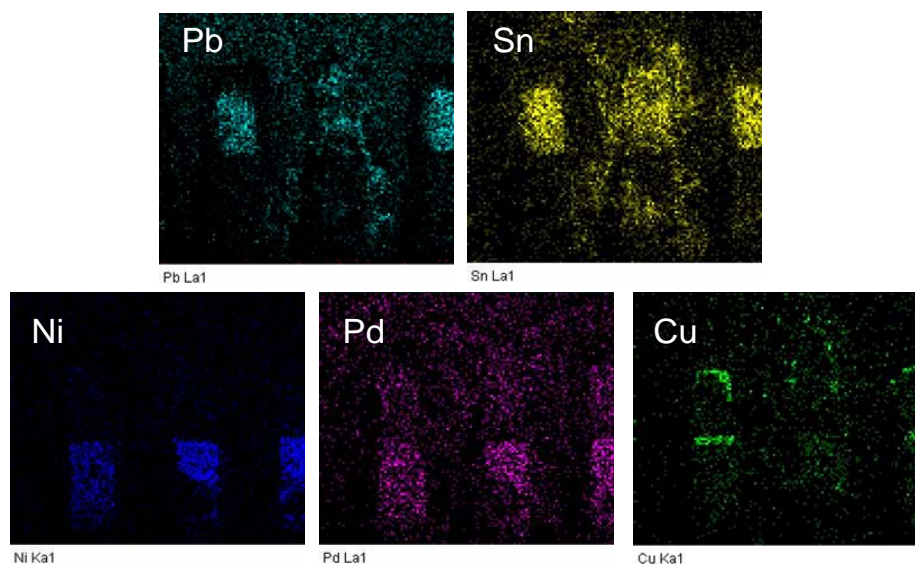


Figure 50: EDS mapping of the area shown in Figure 49

The EDS point analysis was conducted on twelve locations of the deposits between the component leads. The deposits are composed of a mixture of metal oxidation products and dust particles. The probability of presence of each element was summarized in Table 19. The main migrating species were Sn and Pb as well as a very small weight percentage of Cu at some locations. Elements including Si, Ca, Al and S were also detected. The compositions of detected contaminations are very close to dust particles, which normally include quartz sand (SiO_2), feldspar (KAlSi_3O_8 - $\text{NaAlSi}_3\text{O}_8$ - $\text{CaAl}_2\text{Si}_2\text{O}_8$), gypsum ($\text{CaSO}_4 \cdot 2\text{H}_2\text{O}$), etc [28]. Element sulfur may come from gypsum in a form of SO_4^{2-} . It was also possible that sulfur was from $(\text{NH}_4)_2\text{SO}_4$ or NH_4HSO_4 , which are two very common airborne fine mode dust particles. Due to the limited sensitivity for low-Z elements of EDS, elements such as nitrogen (N) and hydrogen (H) cannot be detected, even if they are present.

Table 19: The probability of occurrences of each element on 12 locations

Element	O	Sn	Pb	Si	Al	Cu	S	Ca
Probability of Occurrences	100%	100%	100%	92%	33%	25%	16%	16%

The solder material was eutectic Sn/Pb solder, which had a weight ratio of 63 to 37. The SEM/EDS analysis on the solder material showed a little higher Sn concentration (Sn: Pb= 68:32 at wt%). It can be explained by the Sn-HASL board finish. The percentage of the Sn and Pb in the migratory metals varied from location to location. The average ratio of Sn and Pb on the 12 analyzed points was 84:16 in terms of weight percentage. It showed that Sn was preferentially migrated in this local environment. Pb was more susceptible to migrate compared to Sn in a neutral aqueous solution [37]. As described in section 4.2, the formation of PbSO₄ due to the presence of SO₄²⁻, which is a protective layer, can increase the corrosion resistance of Pb. The dust particles are normally not evenly distributed due to the random deposition process in the field [34]. Therefore, the anions which were dissolved from dust particles had relatively high concentration at some places. It was one of the factors that resulted in the variation of Sn and Pb ratio in the migratory path.

The morphology of dendrite structure was observed under the SEM between shorted leads, shown in Figure 51. There are a lot of fine branches instead of long stick-shape dendrite. The dendrites are composed of small nodular dendrites which are close to each other, shown in (a). The light grey column-like particles are dust particles, which are mainly composed of Ca and O. The dendrites are mixed with the dust particles. The EDS

mapping of the dendrite in (b) indicated that the dendrite structure consisted of metal oxidation of Pb and Sn.

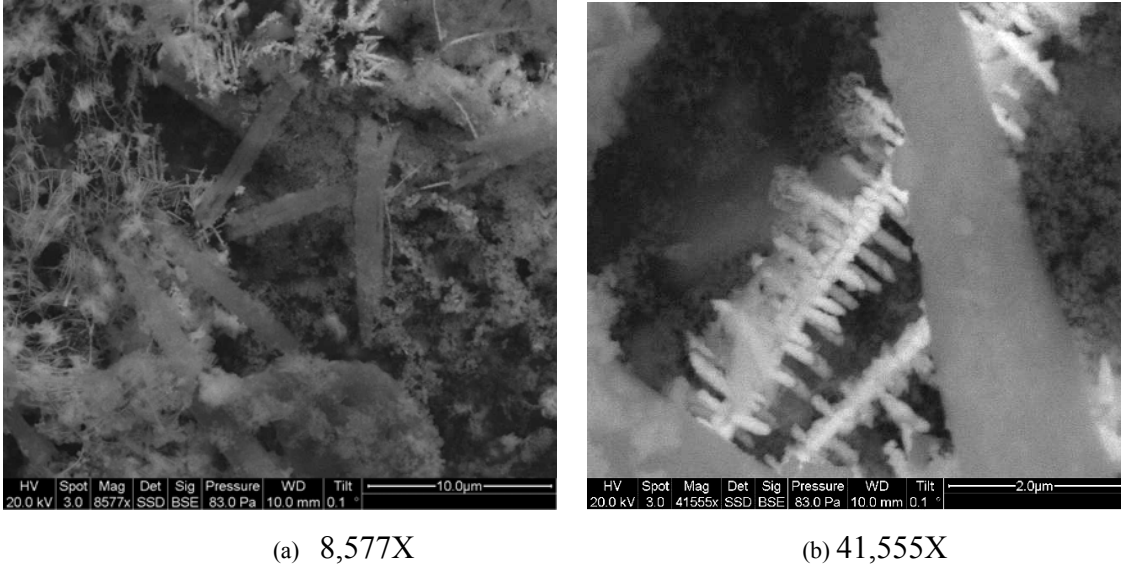


Figure 51: SEM image of Sn-Pb dendrites mixed with dust particles

Case Study 2: Solder Metal Migration with Ni/Pb Lead Finish

Figure 52 shows a SEM image of a migration path that almost spans the two leads. This component is a QFP package with copper leadframe and Ni/Pd finish. The solder paste material is Sn-Pb. Results of EDS mapping on the area indicate that both Sn and Pb are migrated as shown in Figure 53. The migration path started from the lead at the bottom (cathode) of and migrated towards the lead on the top (anode). It appears that the solid metal migration path has not reached the lead on the top.

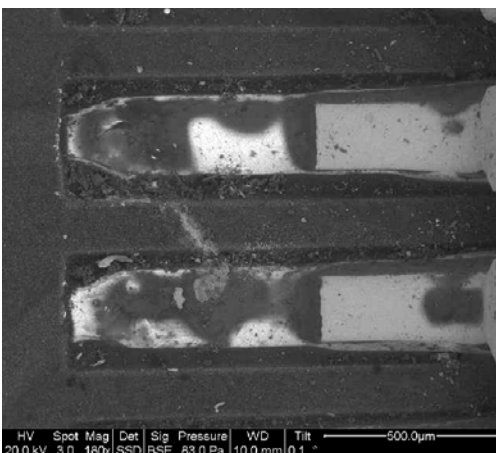


Figure 52: SEM image of dendrite growth between leads

Figure 53: Results of EDS mapping analysis on the substrate between leads

Figure 54 shows the front end of the migration path (close to anode). Some metal particles were dispersed on the substrate and mixed with a lot of particulate contaminations instead of forming a continuous migrating path.

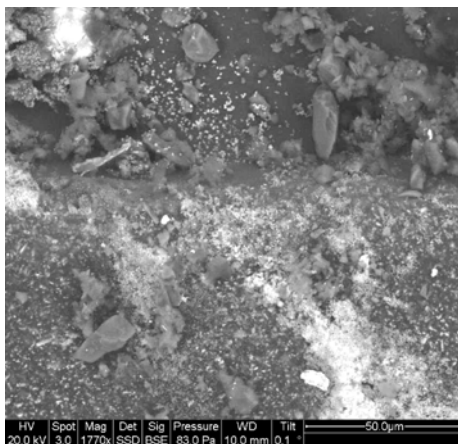


Figure 54: SEM image of front end of the migration path (close to the anode)

High magnification SEM imaging and EDS elemental analysis were performed on this area. The particulate contamination turned out to be dust particles, indicated as point 1 in Figure 55. A lot of particulate contaminations are accumulated on this area. The major compositions are Si, Al, Ca and S, which is consistent with the previous case. The small metal particles dispersed on the contaminations are tin oxides/hydroxides, indicated as point 2 in Figure 55. The tin oxides/hydroxides stay on the dust contaminations. No lead was detected on this area.

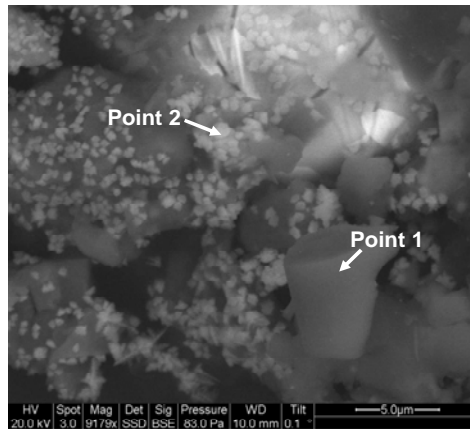


Figure 55: Magnified SEM image with metal oxides/hydroxides and dust particles

In this example, a metal migration path was grown from cathode to anode. At the anode, tin oxides/hydroxides were observed instead of Sn/Pb dendrite. Meanwhile, excessive dust contaminations were observed at this area. The dust particles may increase the local pH value at anode, which can assist the hydrolysis of Sn ions as shown in Eq. 4 and Eq. 5. Excessive formation of hydroxides impedes migration as hydroxides are neutral compounds and therefore they will not migrate under the electric field. Almost no lead was detected at the anode. Further investigation is needed to elucidate the exact reason for this behavior.

Case Study 3: Conductive Path Formation Caused by Dust

The component showed a slightly lower-than-expected SIR between two adjacent leads in the field. Particulate contaminations were found on the substrate spanning the two adjacent leads, shown in Figure 56. There is no metal migration observed. This component has copper leadframe with Sn/Pb finish.

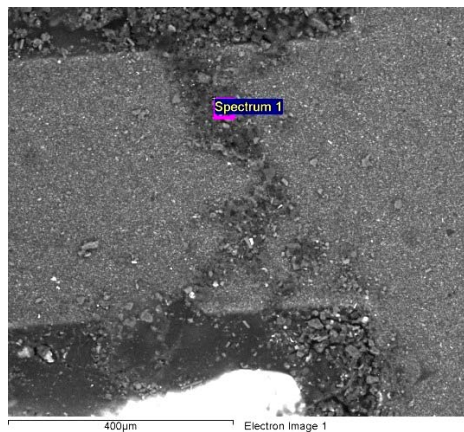


Figure 56: SEM image of a dust formed path

The particulate contaminations present on the board are dust particles containing some inorganic salts based on the preliminary compositional analysis. SEM/EDS analysis indicated the presence of O, Si, Ba, S, Ca and Br. Table 20 lists the weight and atomic percentage of each element. Gypsum (CaSO_4) normally is present when elements of Ca, S and O are shown [3]. CaSO_4 is slightly soluble in the water at room temperature. As temperature goes up, the solubility of CaSO_4 in the water is increased. In a humid condition, SO_4^{2-} can increase the conductivity of the water film to promote the corrosion or ECM to occur. In this case, it did not react with metals. The detection of element Si and O indicate the presence of quartz (SiO_2), which is the second most abundant mineral

in the Earth's continental crust, after feldspar. Element Br was believed to be extracted from flame retardant in the FR-4 PCB.

Table 20: Results of compositional analysis of dust on the substrate.

Element	Weight%	Atomic%
O K	42.67	67.94
Si K	20.85	18.91
S K	5.60	4.45
Ca K	5.09	3.23
Br K	5.11	1.63
Ba L	20.69	3.84
Totals	100.00	100.00

No ECM or corrosion was observed in this area partially because of the big spacing between component leads. The spacing between two leads of this component is around 750 μ m. The voltage gradient between the two leads was not high enough to cause the metal to migrate. Although there is no ECM was observed, this area has a higher reliability risk compared to the clean area due to the presence of dust particles spanning two leads. Those dust particles can cause the water condensation formation at a relatively high RH in the field by capillary wetting. CaSO₄ in the dust particles can dissolve in the water condensation at an elevated temperature in the field and increase the conductivity and total moisture uptake. Considering the impacts of dust, it can lead to the reduction of SIR in the field with high temperature swing and high humidity.

Summary

In the failure analysis, ECM was observed as a dominant failure mechanism in the field samples, despite the fact that the design of the products was qualified through temperature-humidity-bias (THB) testing and was believed to be resistant of corrosion and ECM. In this study of field returned electronic circuit boards, it is found that ECM is also dependent on dust. Some major effects of dust particles on the field samples observed in the examples are summarized as below:

- It has been recognized that Pb was more susceptible to migrate compared to Sn in a neutral aqueous solution. However, due to the presence of ionic contamination of SO_4^{2-} dissolved from dust particles, the migration preference was changed. Sn was found to preferentially migrate in a local environment.
- With the presence of dust particles, the morphology of dendrite structure shows a lot of fine branches instead of long stick-shape dendrite. The dendrites are composed of small nodular dendrites which are close to each other.
- A lot of metal oxides/hydroxides were observed in the dendrite structure with the presence of dust contamination.
- The dust particles can change the local pH value at anode. High contamination levels can lead to excessive formation of hydroxides, which impedes migration to occur. Further investigation is needed to elucidate the exact reason for this behavior.

Chapter 9: Conclusions

This thesis presents an experimental study on the impact of natural dusts on reliability of electronic products. Four different natural dusts were collected and used in the experimental study for loss of impedance and electrochemical migration failures. Loss of impedance in dust contaminated printed circuit boards was investigated under controlled temperature (20°C to 60°C) and relative humidity (50% to 95%) conditions. The impact of dust on electrochemical migration and corrosion was evaluated under temperature-humidity-bias tests (50°C, 90% RH, and 10 VDC). In addition to the conventional DC measurement where only resistive data can be obtained, electrochemical impedance spectroscopy were adopted to obtain a nonlinear equivalent circuit model of the electrochemical process, which helps to understand the underlying physics-of-failure.

The variation of impedance with relative humidity exhibited a transition range. Below the range, the impedance was constant, and above it, the impedance degraded by orders of magnitude. The value of relative humidity range decreased with the increase of dust deposition density. The experimental data confirmed that the hygroscopic property of dust determines the loss of impedance failures. Therefore managing relative humidity is an important consideration in preventing failures caused by dust contaminations.

Using EIS, an equivalent circuit model of the conductive paths of dust contaminated board is introduced to study the electric properties of dust contaminated boards. The equivalent circuit model decomposes the impedance into several components and helps to

understand the variation of impedance with temperature. During the increase of temperature, the largest resistive component changed from the bulk water film to the interface between copper traces and the water film, resulting in a fast decrease of impedance at low temperature and slow decrease in high temperatures.

The differences between ISO test dust and natural dusts were quantified using the degradation factor introduced in the research, the critical transition range, and time-to-failure. The experimental data showed that there are significant differences in the impedance degradation caused by different dust. The difference between ISO test dust and natural dust also demonstrated that using the ISO standard test dust in place of natural dust samples for reliability evaluation can lead to inaccurate results.

The findings in thesis showed that some critical characteristics of dust can be used to classify different dusts for the failure mechanisms of interest. Moisture sorption capability of dust can be used to classify different dusts regarding the loss of impedance failure. The dust with the highest moisture sorption ability had the highest degradation factor. Ion species/concentration or conductivity of dust aqueous solution can be used to classify dust regarding the electrochemical migration related failures. Dust with the highest ion concentration and conductivity had the lowest time-to-failure. The underlying principles behind those critical characteristics were described and discussed based on the physics-of-failure.

Chapter 10: Recommended Future Work

This study experimentally demonstrated that natural dust contamination on PCBs can cause impedance degradation and electrochemical migration failures in not-well-controlled temperature and relative humidity use conditions. Some critical characteristics of dust were identified, which can be used to classify dust based on its impact on dust-related failures in PCBs.

There are few approaches available to classify natural dust concerning its impact on reliability. Also there are no industrial standard on how to evaluate dust effect on reliability in terms of impedance degradation and ECM. This study provides a repeatable and generic test method that can be used to evaluate dust for both failure mechanisms. Based on the results in this thesis, a methodology to evaluate the impact of dust on electronics reliability can be developed for applications in electronics industry.

The recommended reliability assessment methodology is shown in Figure 57. The compositions of standard test dust are defined and formulated using design of experiments. Then, there are two necessary steps to determine the test conditions using this methodology: selection of test dust based on the characterization of the dust samples collected from the field and characterization of the use conditions. The dust samples need to be collected and characterized due to the significant variations among the different dust samples in terms of their impact on reliability, which in turn is caused by the variations in moisture sorption capacity, ion species/concentration, and particles size. The

research results from this thesis showed that the critical relative humidity of mixed salts, percentage of deliquescent substances, moisture sorption capacity are important characteristics of dust that can be considered as candidates for formulating standard dust and classifying natural dust. The use condition characterization includes the estimating dust deposition density, in addition to measuring of temperature, relative humidity, and electrical field during operation. Different reliability assessment tests will be recommended based on the characteristics of dust and use conditions. Three accelerated tests can be considered, including relative humidity ramp up test, temperature ramp up test and temperature-humidity-bias test. The test conditions for these tests should be selected based on the use conditions in the field.

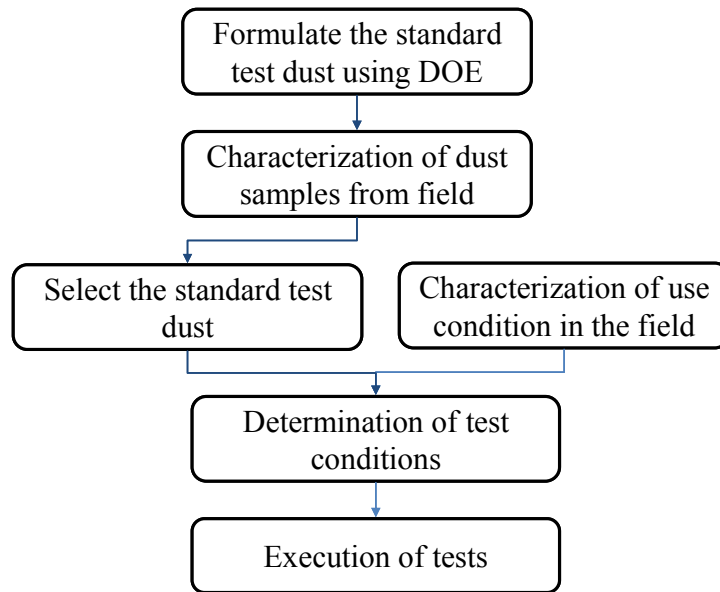


Figure 57: Proposed test methodology for dust evaluation

The compositions of standard test dust should be formulated. The dust sample used in the tests is critical for obtaining accurate reliability test results. The lack of standard test dust is one of the remaining challenges in conducting reliability experiments for the impact of dust. These standard test dusts need to have well-controlled substances and characteristics

which are close to the different natural dust. Design of experiments (DOE) can be performed to verify the important characteristics of dust identified in this thesis. These characteristics of dust can be varied with different levels as the factors in the DOE. The effects of these factors can be evaluated through keeping one factor constant and varying other ones. Potential factors to formulate the standard test dust are listed in the following. Further experiments with dust compositions under the suggested levels can verify the observations and extend the experimental results similar to those obtained in this thesis.

- The concentration of some key ionic contaminations including chloride (Cl⁻), sulfate (SO₄²⁻) and nitrate (NO₃⁻) with levels of 100ppm, 1000ppm and 10000ppm
- The size distribution of the mineral particles: ISO 12103-1, A1 (Ultra fine Test Dust, 1 ~ 20 um), ISO 12103-1, A2 (Fine Test Dust, 1~120 um), ISO 12103-1, A4 (Coarse Test Dust, 1~200 um), or glass sphere with known particle size.

The recommended approaches for most of the steps are listed in Table 21. The results by following this methodology can provide an accurate reliability evaluation of dust-contaminated electronics and reduce the early failure in fields if corrective actions are taken.

Table 21: Recommended evaluation approaches for each step

Steps	Recommended Evaluation Approaches
Formulate the standard test dust using DOE	<ul style="list-style-type: none"> • Critical ion species with different concentrations • Different particle size distribution (μ, Ω) • Different moisture sorption capacity
Characterization of dust samples from field	<ul style="list-style-type: none"> • Ion concentration and species • Moisture sorption capacity • Particle size distribution (μ, Ω)
Characterization of use conditions in the field	<ul style="list-style-type: none"> • Dust deposition density • Relative humidity range • Temperature range
Determination of test conditions	<ul style="list-style-type: none"> • Relative humidity ramp up test • Temperature ramp up test • Temperature-Humidity-Bias test • Test duration
Execution of tests	<ul style="list-style-type: none"> • Determine the pass/fail criteria based on the field application

For the dust characterization, EIS is proven to be a promising approach which can provide mechanistic information of the degradation of dust contaminated printed circuit assemblies by establishing an equivalent circuit to model the system. For future work, it is recommended that the impedance measurement be conducted using electrochemical instruments that have sufficient low frequency. Due to the lack of data at low frequencies, some elements in the equivalent circuit, such as diffusion-controlled impedance and charge transfer resistance, were not extracted in this thesis. More in-depth analysis can be performed if more measurement points at lower frequencies were available. Also a more accurate model with electrical elements associated with possible chemical reactions should be considered in the future work.

Bibliography

- [1] J. Dai, D. Das, and M. Pecht, "Prognostics-Based Risk Mitigation for Telecom Equipment under Free Air Cooling Conditions", *Applied Energy*, Volume 99, November 2012, pp 423–429.
- [2] Intel Information Technology, "Reducing data center cost with an air economizer", *IT@Intel Brief*; Computer Manufacturing; Energy Efficiency; Dec, 2008.
- [3] Jigao Zhang, "Effect of Dust Contamination on Electrical Contact Failure", 53rd IEEE Holm Conference on Electric Contacts, Pittsburgh, PA, USA, Sep. 2007
- [4] Christofer Leygraf, Thomas E. Graedel, "Atmospheric corrosion", John Wiley & Sons, Inc., ISBN 0-471-37219-6, 2000
- [5] Prabjit Singh, Joseph F. Prisco, and Roger R. Schmidt, "Particulate and gaseous contamination: effect on computer reliability and monitoring", *ASHRAE Transactions*, vol. 115, issue 1 pp 58-63, Jan, 2009
- [6] F. S. Sandroff, W. H. Burnett, "Reliability qualification test for circuit boards exposed to airborne hygroscopic dust", *Electronic Components and Technology Conference Proceedings*, pp384 – 389, 1992
- [7] M. Tencer, "Conductive Aqueous Layer Formation at the Gel-Substrate Interface in Equilibrium with 100% RH Environment", *IEEE Transactions on Components and Packaging Technologies*, Vol 23; No. 4, pp 693-699, 2000
- [8] R. P. Frankenthal, D. J. Siconolfi and J. D. Sinclair, "Accelerated Life Testing of Electronic Devices by Atmospheric Particles: Why and How", *J. Electrochemical Soc.*, Vol. 140, pp. 3129-3134, 1993
- [9] M. Tencer, and J. S. Moss, "Humidity management of outdoor electronic equipment: methods, pitfalls, and recommendations", *IEEE Trans. Comp. Packag. Technol.*, vol 25, pp 66-71, Mar. 2002
- [10] Xue-Yan Lin, Ji-Gao Zhang , "Dust Corrosion", *IEEE Holm Conference on Electrical Contacts*, 2004
- [11] D. G. DeNure and E. S. Sproles, Jr. , "Dust test results on multicontact circuit board connectors", *IEEE Transactions on Components, Hybrids, and Manufacturing Technology*, Volume 14, No. 4, 1991

- [12] P-E Tegehall, "Impact of Humidity and Contamination on Surface Insulation Resistance and Electrochemical Migration", IVF Industrial Research and Development Corporation, <http://www.europeanleadfree.net/>
- [13] M. G. Pecht, "An Overview of Key Printed Circuit Board Contaminants", to be submitted
- [14] C. H. Hamann, A. Hamnett, and W. Vielstich, *Electrochemistry*, New York: Wiley-VCH, 1998.
- [15] J. A. Dean, N. Lange, *Lange's Handbook of Chemistry*. McGraw-Hill, 1998.
- [16] J. F. Pankow, *Aquatic Chemistry Concepts*, Boca Raton, FL: CRC Press, 1991.
- [17] C. H. Chen, C. W. Lu, S. M. Huang, W. P. Dow, "Effects of Supporting Electrolytes on Copper Electroplating for Filling Through-Hole," *Electrochimica Acta*, Vol. 56, 2011, pp. 5954011.
- [18] P.-E. Tegehall, "Reliability of contamination from production processes on the reliability of printed board assemblies", Proc. Int. Conf. on Electronic Assembly: Materials and Process Challenges, pp. 69-80, 1998
- [19] Abbott, W.H., "The Development and Performance Characteristics of Flowing Mixed Gas Test Environments," IEEE Transactions on Components, Hybrids, and Manufacturing Technology, vol. 11, no. 1, pp. 22-35, Mar 1988.
- [20] R. Gore, R. Witska and J. Chao, "Corrosive gas environmental testing for electrical contacts", Proc. Of the Holm Conf. on Electric Contacts, pp 123-131, 1989
- [21] S. Zakipour and C. Leygraf, "Evaluation of laboratory tests to simulate indoor corrosion of electrical contact materials", J. Electrochemical Soc. Vol. 133 pp 21-30, 1986
- [22] Mark E Orazem and Bernard Tribollet, *Electrochemical Impedance Spectroscopy*, John Wiley & sons, Inc., 2008.
- [23] J. R. Macdonald, "Impedance spectroscopy," Ann. Biomed. Eng., vol.20, pp. 289-305, 1992.
- [24] Dukhin, A.S. and Goetz, P.J. *Electroacoustic Theory. Ultrasound for Characterizing Colloids*, Elsevier. 2002. Available at <http://www.dispersion.com/pages/theory/psd/modeltheory.html>
- [25] R. Winston Revie and Herbert H. Uhlig, *Corrosion and Corrosion Control: An Introduction to Corrosion Science and Engineering*, John Wiley & Sons, 2008.

- [26] Electrochemistry dictionary and encyclopedia, Case Western Reserve University, <http://electrochem.cwru.edu/ed/dict.htm>
- [27] Attila Husar, Dynamic water management of an open-cathode self-humidified PEMFC system, thesis proposal, Thermal Engineering Department, Universitat Politècnica de Catalunya, 2008.
- [28] Y.N.Liang, J.G.Zhang and J.J.Liu, “Identification of inorganic compounds in dust collected in Beijing and their effects on electric contacts”, 43rd IEEE Holm Conference on Electric Contacts, Philadelphia, PA. USA. Oct.20-22,1997, 315-327
- [29] J.W. Wan, J.C. Gao, X.Y. Lin and J.G. Zhang, “Water-Soluble Salts in Dust and Their Effects on Electric Contact Surfaces”, Proceedings of the International Conference on Electrical Contacts, Electromechanical Components and Their Applications, Jun., 1999, 37-42
- [30] GR-63-CORE: NEBSTM Requirements: Physical Protection, Telcordia Technologies Generic Requirements, Issue 3, March 2006
- [31] J. D. Sinclair, L. A. Psota-Kelty, C. J. Weschler and H. C. Shields, “Measurement and modeling of airborne concentrations and indoor surface accumulation rates of ionic substances at neenah, wisconsin”, Atmos. Environ., Vol. 24A, pp. 627-638, 1990
- [32] J. D. Sinclair, “The relevance of particle contamination to corrosion of electronics in processing and field environments”, Proc. 2nd Int. Symp. Corr. and Reliability of Electronic Materials and Devices, pp. 325-335, 1992
- [33] K.T. Whitby et al, Journal of Colloids and Interface Science, 29, 177, 1975
- [34] Michal Tencer, Deposition of aerosol (“hygroscopic dust”) on electronics – Mechanism and risk, microelectronics Reliability Volume 48, Issue 4, April 2008, pp 584-593
- [35] (a) Hoschen J, Kopelman R. Percolation and cluster distribution. I. Cluster multiple labelling techniques and critical concentration algorithm. Phys Rev B 1976;14:3438–45; (b) Hoschen J, Kopelman R, Monberg EM. Percolation and cluster distribution. II. Layers, variable-range interactions and exact cluster model. J Statist Phys 1978;19:219–42.
- [36] Ja-Young Jung, Shin-Bok Lee, Ho-Young Lee, Young-Chang Joo and Young-Bae Park, Electrochemical Migration Characteristics of Eutectic Sn-Pb Solder Alloy in NaCl and Na₂SO₄ Solutions, Journal of Electronic Materials, Volume 38, Number 5, 691-699, 2009

- [37] D. Q. Yu, W. Jillek and E. Schmitt, Electrochemical migration of Sn-Pb and lead free solder alloys under distilled water, *Journal of Materials Science: Materials in Electronics*, Volume 17, Number 3, 219-227, 2006
- [38] Gábor Harsányi, “Irregular effect of chloride impurities on migration failure reliability: contradictions or understandable?”, *Microelectronics Reliability*, Volume 39, Issue 9, September 1999, Pages 1407-1411
- [39] G. T. Kohman, H. W. Hermance, and G. H. Domes "Silver migration in electrical insulation," *Bell System Technical Journal* vol. 34, pp. 11-15, 1955.
- [40] A DerMarderosian, "The electrochemical migration of metals," *Proc. Int. Society of Hybrid Microelectronics*, p.134, 1978.
- [41] G. Ripka and G. Harshyi, "Electrochemical migration in thick-film ICs," *Electrocomp. Sci. Technol.*, vol. 11, p. 281, 1985.
- [42] M. V. Coleman and A E. Winster, "Silver migration in thick-film conductors and chip attachment resins," *Microelectronics Journal*, No. 4, p. 23, 1981
- [43] Katayanagi, H., Tanaka, H., Aoki, Y., Yamamoto, S., *ESPEC Technology Report*, 9 p15-20
- [44] P. Zhao and M. Pecht “Assessment of Ni/Pd/Au–Pd and Ni/Pd/Au–Ag Preplated Leadframe Packages Subject to Electrochemical Migration and Mixed Flowing Gas Tests”, *IEEE Transactions on Components and Packaging Technologies*, VOL. 29, No. 4, December 2006, p. 818-826
- [45] M. Schelesinger and M. Paunovic, *Modern Electroplating*, Wiley New York, NY 2000
- [46] S.A.M. Refaey, F. Taha, and T.H.A. Hasanin, *Electrochim. Acta* 51, 2942 (2006). doi:10.1016/j.electacta.2005.09.033
- [47] V. Maksimovic, M. Pavlovic, Lj. Pavlovic, M. Tomic, and V. Jovic, “Morphology and Growth of Electrodeposited Silver Powder Particles,” *Hydrometallurgy*, No. 86, pp. 22-26, 2007
- [48] U.S. Mohanty and K.-L. Lin, *Appl. Surf. Sci.* 252, 5907, (2006)., doi:10.1016/j.apsusc. 2005.08.020.
- [49] Nieman DA. Effect of contamination on copper migration in TAB tape structures. In: *Proc. of the International Reliability Physics Symp.* 1994. pp 87 - 92.
- [50] E.F.F. El-Sherbini, S.M. Abd-El-Wahab, M.A. Amin, and M.A. Deyab, *Corros. Sci.* 48, 1885 (2006). doi: 10.1016/j.corsci.2005.08.002

- [51] S.J. Krumbein and A.H. Reed, "New Studies of Silver Electromigration," in Proc. 9th Int. Conf. on Electric Contact Phenomena, 1978, p. 145
- [52] S.J. Krumbein, Electrolytic models for metallic electromigration failure mechanisms,, IEEE Transactions on Reliability. 44 (1995) 539–549
- [53] S.A.Self, G.B.Moslehi, M.Mitchner and R.Leach, "Electromechanics and Reentrainment of Precipitated Ash", Proceeding of the International Conference on Electrostatic Precipitation, Oct 14-18, 1981
- [54] GR-63-CORE: NEBSTM Requirements: Physical Protection, Telcordia Technologies Generic Requirements, Issue 3, March 2006
- [55] G. DiGiacomo, "Metal Migration (Ag, Cu, Pb) in Encapsulated Modules and Time to Fail Model as a Function of the Environment and Package Properties," IEEE/ Proceedings of the IRPS, 1982. pp. 27 – 33
- [56] D. Minzari, M.S. Jellesen, P. Møller, P. Wahlberg, and R. Ambat, "Electrochemical migration on electronic chip resistors in chloride environments," IEEE Transactions on Device and Materials Reliability, vol. 9, 2009, pp. 392–402.
- [57] D. Minzari, M.S. Jellesen, P. Møller, and R. Ambat, "On the electrochemical migration mechanism of tin in electronics", Corrosion Science, vol 53, issue 10, pp 3366–3379, 2011.
- [58] Bo-In Noha, Jong-Bum Leea and Seung-Boo Jung, "Effect of surface finish material on printed circuit board for electrochemical migration", Microelectronics Reliability, Volume 48, Issue 4, April 2008, Pages 652-656
- [59] Tullmin and P. R. Roberge, Uhlig's Corrosion Handbook, Second Edition, Edited by R. Winston Revie. John Wiley & Sons, Inc. Chapter 18: Atmospheric Corrosion, M pp. 305-321.
- [60] K. Barton, "Protection against Atmospheric Corrosion," Wiley, New York, 1976.
- [61] Brian E. Conway, "Electrochemical Capacitors, Their Nature, Function, and Applications", retrieved from <http://electrochem.cwru.edu/encycl/art-c03-elchem-cap.htm>.
- [62] S. Zhan, M. H. Azarian and M. Pecht, "Surface Insulation Resistance of Conformally Coated Printed Circuits Boards Processed with No-Clean Flux," IEEE Trans. EPM., Vol. 29, No. 3, July, 2006, pp. 217-223.
- [63] Electrochemical Migration Resistance Test. Northbrook, IL: IPC, Sept. 2000, IPC Publication IPC-TM-650, Method 2.6.14.1.

- [64] X. F. He, M. H. Azarian and M. G. Pecht, "Evaluation of Electrochemical Migration on Printed Circuit Boards with Lead-Free and Tin-Lead Solder", *Journal of Electronic Materials*, Vol. 40, No. 9, 2011, pp. 1921-1936.
- [65] http://www.tis-gdv.de/tis_e/misc/klima.htm.
- [66] E. Warraky, H. A. El Shayeb and E. M. Sherif, "Pitting corrosion of copper in chloride solutions", *Anti-Corrosion Methods and Materials*, Volume 51, Number 1, 2004, pp. 52-61.
- [67] B. D. Dunn and G. Chandler, "The Corrosive Effects of Soldering Fluxes and Handling on Some Electronic Materials," *Welding Journal*, Vol. 59, No. 10, 1980, pp. 289 s-307 s.
- [68] J. C. Galvan, J. M. Bastidas and S. Feliu, "A Study of the Corrosive Effect of Soldering Fluxes on Printed Circuit Boards," *Welding Research Supplement*, Vol. 75, No. 11, 1996, pp. 366 s-371s.
- [69] E. Bumiller, M. Pecht and C. Hillman, "Electrochemical Migration on HASL Plated FR-4 Printed Circuit Boards", *Journal of Surface Mount Technology*, Vol.17, No. 2, 2004, pp.37-41.
- [70] M. Weekes, "PWB Contamination & Reliability DOE", *Proceedings of SMTA International Conference*, Chicago, IL, September 2001.
- [71] IPC, "Requirements for Soldered Electrical and Electronic Assemblies", J-STD-001C, Section 8.3.7, Northbrook, IL, March 2000.
- [72] H. A. Chan, "Surface insulation resistance methodology for today's manufacturing technology," *Components, Packaging, and Manufacturing Technology, Part C, IEEE Transactions on*, Volume: 19 , Issue: 4, 1996 , pp. 300 – 306.
- [73] X. He, M. H. Azarian, and M. G. Pecht, "Effects of Solder Mask and Flux Solids on Electrochemical Migration of Tin-Lead and Lead-Free Boards", *Proceedings of IPC APEX Expo Conference*, Las Vegas, NV, April 2010.
- [74] Y. Jin, L. Tao, Y. Chi, and J. Yan , "Conversion of Bromine during Thermal Decomposition of Printed Circuit Boards at High Temperature", *Journal of Hazard Material*, Vol. 186, No. 1, 2011, pp. 707.
- [75] F. Barontini, and V. Cozzani, "Formation of Hydrogen Bromide and Organobrominated Compounds in the Thermal Degradation of Electronic Boards", *Journal of Analytical Applied Pyrolysis*, No. 77, 2006, pp. 41-55.

- [76] H. E. Gunning, A. R. Gordo, "The Conductance of Aqueous Solutions of Potassium Bromide at Temperatures from 15° to 45°C, and the Limiting Mobility of Bromide Ion," *Journal of Chemical Physics*, Vol. 11, 1942, pp. 18-20.
- [77] R. P. Frankenthal, R. Lobnig, D. J. Siconolfi, and J. D. Sinclair, "Role of Particle Contamination in the Corrosion of Electronic Materials and Devices," *Journal of Vacuum Science and Technology*, Vol. A 11, Iss. 4, 1993, pp. 2274-2279.
- [78] R. B. Comizzoli, C. A. Jankoski, G. A. Peins, L. A. Psota-Kelty, D. J. Siconolfi, and J. D. Sinclair, "Reliability of Electronics in Harsh Environments: Electrical Leakage and Corrosion Caused by Hygroscopic Pollutant Particles", in *Corrosion and Reliability of Electronic Materials and Devices*, R. B. Comizzoli, R. P. Frankenthal and J. D. Sinclair, Eds., PV 99-29, The Electrochemical Society, Inc., Pennington, NJ, 1999.
- [79] *Guidelines for Design, Selection and Application of Conformal Coatings*, IPC-HDBK-830, 2002, p 58.
- [80] Lisa J. Mauer and Lynne S. Taylor, "Water-Solids Interactions: Deliquescence", *Annual Review of Food Science and Technology*, Vol. 1: 41-63, 2010.
- [81] Charles J. Weschler, "Predictions of Benefits and Costs Derived from Improving Indoor Air Quality in Telephone Switching Offices", *Indoor Air*, Volume 1, Issue 1, pages 65–78, 1991.
- [82] ASHRAE, "Gaseous and Particulate Contamination Guidelines for Data Centers," Atlanta, GA: ASHRAE, 2009
- [83] V. Kucera and E. Mattson, "Atmospheric Corrosion," in *Corrosion Mechanisms*, F. Mansfeld (ed.), Marcel Dekker, New York, 1987.
- [84] A. Hornung, "Diffusion of Silver in Borosilicate Glass," *Proceedings of the 1968 IEEE Electronic Components Conference*, New York, , 1968. pp. 250-5.
- [85] IPC handbook, "Surface Insulation Resistance Handbook," IPC-9201, Northbrook, IL, July 1990.
- [86] M. Pourbaix, "The Linear Bilogarithmic Law for Atmospheric Corrosion," in *Atmospheric Corrosion*, ed. W. H. Ailor New York, John Wiley and Sons, 1982.
- [87] Power Technology Inc., Arizona Test dust, 9/13/ 2012, http://www.powdertechnologyinc.com/material_processed/test-dust/
- [88] William C Keene, Rolf Sander, Alexander A.P Pszenny, Rainer Vogt, Paul J Crutzen, James N Galloway¹, "Aerosol pH in the marine boundary layer: A review and model evaluation", *Journal of Aerosol Science*, Vol 29, pp 339-356, 1998.

- [89] H. H. Lawson, "Atmospheric corrosion test methods", Houston, TX: NACE International, 77 pp, 1995.
- [90] Ling Chunxian Zou and Christopher Hunt, "Characterization of the conduction mechanisms in adsorbed electrolyte layers on electronic boards using AC impedance", *Journal of the Electrochemical Society*, Vol 156, No. 1 pp C8-C15 (2009).
- [91] Hualiang Huang, Xingpeng Guo, Guoan Zhang and Zehua Dong, "The effects of temperature and electric field on atmospheric corrosion behavior of PCB-Cu under absorbed thin electrolyte layer", *Corrosion Science*, Vol 53, pp 1700-1707, 2011.
- [92] J. Chen, Z. Qin and D. W. Shoesmith, "Kinetics of corrosion film growth on copper in neutral chloride solutions containing small concentration of sulfide", *Journal of the Electrochemical Society*, Vol 157, No. 10, pp C338-C345, 2010.
- [93] B. Song, M. H. Azarian and M. G. Pecht, "Impact of Dust on PCB Reliability under Varying Temperature and Relative Humidity", *Journal of the Electrochemical Society*, 2013, Volume 160, Issue 3, Pages C97-C105.
- [94] B. Song, M. H. Azarian and M. G. Pecht, "Impact of Dust on Printed Circuit Assembly Reliability", IPC APEX Conference and Exhibition, San Diego, Feb. 2011.
- [95] T. Horikawa, D.D. Do and D. Nicholson, "Capillary condensation of adsorbates in porous materials", *Adv. Colloid Interface Sci.*, 169, pp 40-58, 2011.
- [96] Tang and Munkelwitz, "Composition and temperature dependence of the deliquescence properties of hygroscopic aerosols", *Atmospheric Environment. Part A. General Topics*, 1993
- [97] K. M. Takahashi, "Conduction paths and mechanisms in FR-4 epoxy/glass composite printed wiring boards", *J. Electrochem. Soc.*, vol 138, pp 1587-1593, 1991.